MAX-PLANCK-INSTITUT FÜR QUANTENOPTIK

Guiding and Trapping of Cold Dipolar Molecules

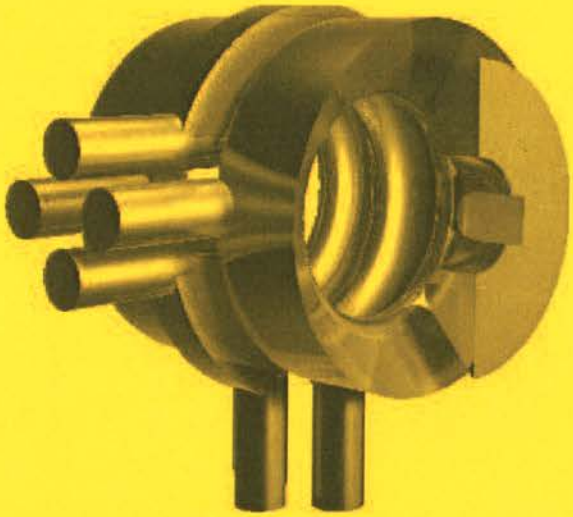

Tobias Junglen

MPQ-Report 304

April 2006

Max-Planck-Institut für Quantenoptik
Hans-Kopfermann-Str. 1
D-85748 Garching, Bundesrepublik Deutschland

MAX-PLANCK-INSTITUT FÜR QUANTENOPTIK

Guiding and Trapping of Cold Dipolar Molecules

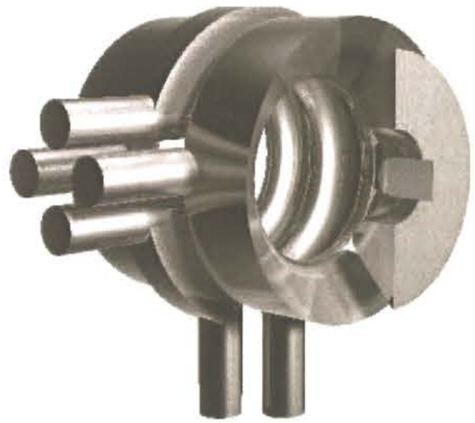

Tobias Junglen

MPQ 304 April 2006

Zusammenfassung

Im Rahmen dieser Arbeit wurde eine Methode zum Filtern und Führen von kalten polaren Molekülen entwickelt. Im Filterprozess wird die Wechselwirkung der Moleküle mit einem inhomogenen elektrostatischen Feld eines gebogenen Quadrupols genutzt, um die langsamen Moleküle von den schnellen Molekülen eines thermischen Strahls abzutrennen. Die Experimente wurden mit Ammoniak und Formaldehyd durchgeführt. Den Geschwindigkeiten der selektierten Moleküle konnten Temperaturen von wenigen Kelvin zugeordnet werden. Diese Quelle kalter Moleküle wurde weiterhin verwendet, um eine neuartige elektrostatische Falle für polare Moleküle zu demonstrieren, die kontinuierlich geladen wird.

Abstract

In this thesis, a method for filtering and guiding of cold polar molecules has been developed. In the filtering process, the interaction of the molecules with an inhomogeneous electrostatic field of a bent quadrupole is exploited to select the slow molecules from a thermal molecular beam. The experiments have been performed with ammonia and formaldehyde. The velocities of the selected molecules correspond to temperatures of a few kelvin. This source of cold molecules has further been used to demonstrate a novel electrostatic trap for polar molecules which is continuously loaded.

Contents

Chapter 1

General Introduction

During the past years a rapidly growing interest in the field of cold molecules has been observed. The possibility to investigate molecular behavior at low temperatures motivates physicists and chemists from diverse backgrounds to produce cold and dense samples. Certainly, this development is inspired by the great successes in the closely related field of cold atoms which led to the demonstration of Bose-Einstein condensation in ultracold atomic gases in 1995. The extension of these investigations to molecules is desirable as due to their complex internal structure, molecules offer properties which are not available with atoms, such as a permanent electric dipole moment. The long range and anisotropic character of the dipole-dipole interaction is expected to lead to new physics as the interaction of the molecules depends on the orientation of the dipole moments. It is expected that cold molecular samples enable a deeper insight in molecular collisions and chemical reactions. Indeed, the availability of almost motionless molecules holds the promise to open up a completely new regime in chemistry. Further applications of cold molecules can be found in the field of metrology as high-precision measurements benefit from the extended interaction times of cold molecules in external fields.

However, the production of cold molecules is not as straightforward as it is the case for atoms because there exists no simple extension of the laser-cooling technique to molecules. Up to now, there are at least about ten different methods to produce cold molecules, a number that is rapidly increasing with time. We designate molecules as cold or slow if their translational temperature is of the order of a kelvin or lower. Such molecules can be easily manipulated and trapped with electromagnetic fields. In principle, large quantities of such molecules are present in any thermal gas, they only need to be filtered out efficiently. This thesis describes a method where the Stark interaction of polar molecules with electric fields is exploited to filter translationally cold molecules effusing from a thermal reservoir. The method which is demonstrated with ammonia (ND_3) and formaldehyde (CH_2O) allows filtering and guiding of any polar molecule with a sufficiently high Stark shift. The slow molecules are further used to demonstrate a new large-volume electrostatic trap which can be loaded continuously.

This thesis is organized as follows: In the remainder of this chapter the motivation for studying cold molecules is made more explicit, and an overview over the different meth-

ods of producing cold atoms and molecules is given. In Chapter II, the manipulation of polar molecules using electric fields is explained and several two- and three-dimensional trapping schemes are detailed. Chapter III deals with the theoretical aspects of filtering, and the experimental demonstration of filtering and guiding is presented. In Chapter IV, the technical realization of the trapping scheme as well as the characterization of the trap are described. This thesis concludes with Chapter V where an outlook over the further prospects of the guiding and trapping technique is given.

1.1 Application of Cold Molecules

In the following, several fields of research are introduced where cold molecules play an important role. Many of the applications discussed here are currently being pursued, however, some applications are not yet amenable with the densities and temperatures available at present.

Time-Reversal Invariance in Molecules

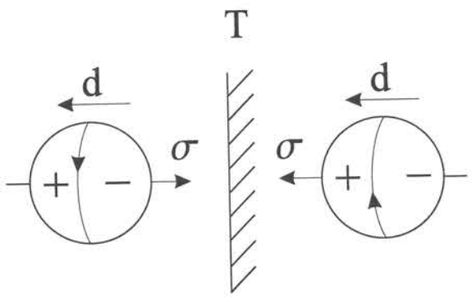

Figure 1.1: *An elementary particle having angular momentum σ and a permanent electric dipole moment* $\boldsymbol{d}$*. If time is reversed the angular momentum changes direction but the charge distribution determining the dipole moment remains unchanged. This means that the product* $\boldsymbol{d}\cdot\sigma$ *is different in the normal and time-reversed worlds.*

In the middle of the last century it was believed that the fundamental forces of nature are invariant under the discrete symmetries spatial inversion (parity, P), temporal inversion (time reversal, T), and the replacement of all particles by their antiparticles (charge conjugation, C). Already in 1956 it was suggested that the symmetry of P is violated in the weak interaction which has been confirmed by the observation of an asymmetry in the β decay of polarized ^{60}Co [1]. After the first observation of P violation, it was generally believed that the symmetry of T invariance is still conserved. However, in 1964 it was discovered that the neutral long-lived K meson was not invariant under the combined operations of C and P [2]. Due to the CPT theorem which requires that a system is invariant

under the combined operations of C, P, and T a system necessarily violates the symmetry of T if it violates CP [3]. Up to now, the only system violating T symmetry is the neutral kaon. In the Standard Model, T is not an exact symmetry but it is nearly exact in normal matter like electrons, protons and neutrons [4]. The discovery of a violation of T has initiated many experimental activities trying to find T violation in other systems. The most sensitive of these experiments are looking for a permanent electric dipole moment (EDM) of the electron which can be understood as the average displacement of charge from the center of mass. Only the displacement along the spin axis contributes to the dipole moment because the spin averages the other components to zero. Consequently, the spin and dipole moment are parallel or antiparallel. The Standard Model predicts an electron EDM of less than $10^{-38}\,e\,\mathrm{cm}$, where e is the charge of the electron, which is far too small to be measured. However, theories beyond the Standard Model predict values in the range of $10^{-25} - 10^{-26}\,e\,\mathrm{cm}$ which are closer to the current experimental limit. The search for the electron dipole moment is, therefore, a search for new physics beyond the Standard Model, and the results play an important role in deciding which of the models correctly describes the fundamental interactions. The connection between T variance and the EDM of a fundamental spin-1/2 particle like an electron or a neutron can be seen in Fig. 1.1. It becomes obvious that the EDM has to be zero in order not to violate T invariance.

If an electron is placed in an external electric field, $\boldsymbol{E}_{ext}$, its EDM has an interaction energy $-\boldsymbol{d}\cdot\boldsymbol{E}_{ext}$. The basic idea of any experiment measuring the electron's EDM is to compare the energies when $\boldsymbol{d}$ is parallel and antiparallel to the electric field. This can be performed in an interferometer where the phase difference between the states with the opposite orientations is measured. Obviously, the experiment cannot be performed with a free electron as it would immediately crash into the electrodes generating the fields. The solution to this problem is that one uses an electron in an atom or a molecule. Sandars discovered in 1967 that the EDM of a molecule is related to the EDM of an electron by a factor of order $Z^3\alpha^2$ where α is the fine-structure constant and Z the mass-number [5]. As a consequence, heavy molecules show a significantly larger EDM than the electron. Especially polar molecules with strong ionic bonds are suited for these experiments as they can be completely polarized in attainable laboratory electric fields. Note that the interaction of the electron's EDM with $\boldsymbol{E}_{ext}$ is not to be confused with the interaction of the molecule's dipole moment with $\boldsymbol{E}_{ext}$ which gives rise to the Stark shift. Both effects can be distinguished by reversing the orientation of $\boldsymbol{E}_{ext}$ because this changes the sign of the T-violating interaction but not the Stark effect.

Up to now, the most precise measurement of the electron EDM is that of Regan *et al.* [6] who searched for a differential Stark shift in atomic thallium. The first attempt using polar molecules was performed by Hudson *et al.* [7]. Even though this molecular method is not yet as accurate as the atomic experiments it is acknowledged that the use of molecules is potentially much more sensitive. The use of cold molecules in the subkelvin regime promises to increase the sensitivity by orders of magnitude [8]. For further reading, see also the references [9, 10].

Cold Chemistry

Recent developments in the production, cooling and trapping of molecules at low temperatures open the perspective to observe and investigate chemical reactions at the low temperature limit. One of the basic questions in the field of cold chemistry is whether chemical reactions are possible at ultralow temperatures. Especially chemists are interested in the efficiency of chemical reactions and the inelastic energy transfer in molecular collisions under these conditions. At low kinetic energies, the dynamics of colliding atoms and molecules is dominated by quantum effects. In this regime, it is predicted that the inelastic processes will occur more frequently than elastic collisions as the cross-sections depend on the inverse of the initial relative velocity [11]. In theoretical studies of chemical reactions it has been observed that due to the long durations of the collisions tunneling through repulsive potentials can occur even in the limit of zero temperature [12]. Close to the tunneling region, sharp van der Waals resonance states can occur which open a completely new regime of chemical reactions [13, 14, 15]. It is further expected that unusual resonant states can be formed when the colliding molecules begin to rotate, leaving them with insufficient translational energy to overcome their van der Waals attraction. Those resonances cannot be observed in atom-atom collisions as they result from the rearrangement of rotational energy.

Dipole-Dipole Interaction

The past time has seen an increasing interest in the dipole-dipole (DD) interaction in ultracold gases. The DD interaction potential between two dipolar particles has two important properties: it is anisotropic, and it is of long range character. If the dipole moments are sufficiently large, the resulting DD forces can influence the properties of Bose-Einstein condensation (BEC) in bosonic gases. The investigation of the stability of a BEC of trapped dipolar particles, where the interparticle interaction is dominated by the DD force, has revealed striking differences from common atomic condensates. It has been calculated that in the BEC regime the sign and the strength of the DD interaction strongly depends on the trapping geometry [16, 17]. In the calculations, a BEC of dipolar particles in a cylindrical harmonic trap has been assumed where all dipoles are oriented along the trap axis. In cigar shaped traps along the dipole direction, the interactions will be mainly attractive leading to an unstable condensate similar to the case of a Bose gas with a negative scattering length. Conversely, in pancake traps the interactions will be mainly repulsive and the gas will be stable. The possibility to modify the shape of the trapping potential opens the perspective to tune the interaction between the particles.
The observation of DD interactions in alkali BECs is challenging as the DD interaction is negligible compared to the s-wave pseudopotential. Nevertheless, it has been proposed that even in alkali BECs the (magnetic) DD interaction can be made visible using rotating magnetic fields [18]. Among the elements which have been Bose condensed so far, the element chromium plays a particular role due to its high magnetic moment of 6 Bohr magnetons [19]. As the magnetic DD interaction scales with the square of the magnetic dipole moment, it is a factor of 36 higher than for alkali elements. Therefore, it is likely

that the DD interaction becomes observable in a chromium BEC [19]. The interaction in the gas plays a decisive role in Fermi gases. Due to the Pauli principle, the interaction between identical fermions vanishes at ultracold temperatures. In order to reach quantum degeneracy, the simultaneous trapping of at least two different fermionic species is required for efficient collisional cooling. Ultracold polar gases, however, interact via DD interaction which is energy independent in the ultracold limit [17]. This opens prospects to observe the effects of interparticle interactions in a single-component Fermi gas.
The most promising candidates for the observation of the DD interaction in ultracold gases are polar molecules as the electric DD interaction is typically three orders of magnitude larger than its magnetic counterpart [18]. In order to stabilize strongly interacting dipolar systems, the ability to tune the interaction between the particles by the shape of the trapping potential might become a relevant technique.

1.2 Cooling Techniques for Atoms

In general, the term cooling refers to processes compressing the velocity distribution of an ensemble. However, there exists a narrower definition considering only the suppression of phase-space density as true cooling. The phase-space distribution of an ensemble can be defined in terms of the probability to find a particle in a certain space and momentum interval. The phase-space density $n\Lambda^3$ depends on n the number density and $\Lambda = (2\pi\hbar^2/mk_BT)^{1/2}$ the thermal de Broglie wavelength where T is the temperature. For an ideal Boltzmann gas, $n\Lambda^3 \ll 1$. The parameter $n\Lambda^3$ plays an important role in quantifying the quantum degeneracy of a gas where for a Bose-Einstein condensate $n\Lambda^3 > 2.6$ as demonstrated in many experiments with ultracold atoms. Cooling in terms of increasing $n\Lambda^3$ in a molecular sample is very challenging. Nevertheless, the field of cold molecules has benefited from the rapid development of cooling techniques for atoms as, for instance, cold diatomic molecules can be composed from cold precursor atoms. In the following, the present day standard cooling techniques for atoms are briefly described.

1.2.1 Laser Cooling and Trapping

Laser cooling exploits the fact that atoms can be cooled by successive absorption-emission cycles of light which is resonant to a closed atomic transition. Every absorption and emission is assisted with a photon recoil which changes the momentum of the atom. This effect is exploited in the magneto-optical trap (MOT) which has become the standard technique for producing ultracold atoms. In a MOT, the Doppler effect and the ability to manipulate the atomic levels with magnetic fields provide a position and velocity dependence of the light force, so that the atoms experience a friction force damping their motion in the light field. This friction and the dissipative spontaneous emission lead to a compression of the phase-space density. At present, laser cooling and trapping is a standard technique which allows to prepare cold atoms at temperatures below 1 mK with densities of 10^{10} cm^{-3}.

The cooling can be enhanced by polarization gradient cooling which leads to temperatures in the low microkelvin regime. However, laser cooling is restricted to atoms with a "simple" energy level structure in order to provide a closed cycle transition. Molecules with their complex internal energy level structure have not been laser-cooled so far as a closed transition is difficult to establish.

1.2.2 Buffer-Gas Cooling

Before the advent of the laser-cooling technique, cryogenic buffer-gas cooling was used to cool down atomic hydrogen where the unique low binding energy of H to a liquid He surface has been exploited. This property made it possible to cool and stabilize spin-polarized atomic hydrogen to millikelvin temperatures by surface thermalization in a dilution refrigerator [20] and to trap it in magnetic fields [21, 22]. Unfortunately, all other species have much higher binding energies with cold surfaces and, at the low temperatures required for loading a trap, all atoms would stick to the recipient walls. The solution to this problem is to use He as a buffer gas which is employed to thermalize the atoms by elastic collisions to temperatures below the trap depth before the particle touches the walls. After thermalization, the buffer-gas is (cryo-)pumped away, leaving a thermally isolated sample in the trap. Initially this cooling technique has been demonstrated with the paramagnetic atoms europium [23] and chromium [24] which were vaporized by laser ablation in a cold ^{3}He gas inside the cryostat. After 30 ms of thermalization with the buffer-gas, atomic europium is cooled down to 250 mK. The large paramagnetism of europium makes it easy to trap in magnetic fields, and up to 1×10^{12} Eu atoms can be loaded at a density of 5×10^{12} cm^{-3}. The atoms can be held for longer than 100 s.
As elastic collisions are independent of the internal structure, buffer-gas cooling provides a general method to cool atoms not amenable to laser-cooling and even molecules [25]. With this technique, the cooling and trapping of the paramagnetic molecule calcium monohydride (CaH) has been demonstrated [26]. In this experiment, a number of 1×10^8 CaH molecules which were generated by laser ablation could be trapped at a temperature of 400 mK after a thermalization time of 200 ms. The molecules inside the trap were at a density of 8×10^7 cm^{-3} and they could be observed for 2 s. The removal of the buffer-gas should lead to evaporative cooling, however, in this experiment the pump down time exceeds the lifetime of the trapped molecular sample so that significant evaporative cooling could not be observed. Vaporization of particles by laser ablation has significant drawbacks like, for example, additional heat input, poor purity of the sample, and a limited number of particles in the gas phase. Some of these drawbacks are overcome by loading the trap from a particle beam which is guided into the cryostat where the thermalization occurs [27].

1.2.3 Evaporative Cooling

Evaporative cooling allows to cool an ensemble even if there are no dissipative external forces. In a trapped ensemble in thermal equilibrium, the energy distribution of the

particles is given by the Boltzmann distribution. If particles whose energy exceeds a certain energy threshold were removed from the ensemble, the remaining ensemble would relax by elastic collisions in order to establish the thermodynamic equilibrium again. Due to energy conservation, the maximum of the distribution of the remaining ensemble is shifted to lower energies. This results in a cooling of the ensemble as temperature is proportional to energy. The timescale for evaporation is closely related to the duration of the thermalization which depends on the elastic collision rate, and thus on the density, and on the trap depth compared to the energy of the trapped gas. The evaporation has to compete with heating processes caused by inelastic collisions and collisions with the background gas. Evaporative cooling of a magnetically trapped atomic sample has first been considered by Hess [28] and it was demonstrated in 1988 with spin-polarized atomic hydrogen [29]. In this experiment, the evaporation was induced by lowering the magnetic trapping field and a temperature of 3.0 mK could be obtained with a central density of 7.6 $\times$ 10^{12} cm^{-3}. Lowering the trapping field leads to an inefficient cooling process because the reduced density affects the thermalization. The solution to this problem was the implementation of radio frequency induced evaporation where the trap depth is set by the radio frequency "knife" removing high-energy particles that reach a certain magnetic field value. Lowering the trap depth leads to an increase in density which forwards the evaporation process and by that the phase-space density increases by several orders of magnitude. Applying evaporative cooling to a laser-cooled atomic sample is the final step in experiments which have led to Bose-Einstein condensation [30, 31, 32].

1.3 Generation of Molecules from Cold Atoms

The ability to produce cold and dense atomic samples by laser cooling and trapping techniques has led to the idea to generate cold molecules by photoassociation [33]. This technique which is applicable to homo- and heteronuclear atomic samples is widely being used to generate molecules from laser-cooled precursor atoms. Another method uses Feshbach resonances in ultracold degenerate atomic gases which allow to precisely control the interactions between the atoms including molecule formation. In the following, both methods are described in detail.

1.3.1 Photoassociation

In the photoassociation (PA) process, a pair of free cold atoms resonantly absorbs one photon which leads to the formation of an excited molecule. This technique has been successfully applied to all the alkali atoms (for a review see [34]) as well as for hydrogen [35], metastable helium [36], calcium [37] and ytterbium [38]. The formation of heteronuclear molecules has quickly been considered [39] as it opens the perspective to generate polar molecules. However, for heteronuclear molecules the properties of the molecular potentials make it difficult to achieve PA. Heteronuclear PA has been demonstrated with two isotopes of lithium [40] but the resulting molecular dipole moment was negligible due to the identical nuclear charges. Furthermore, the small isotope shift led to a rather homonuclear character

of the PA process. The first production of ultracold, polar molecules with a heteronuclear PA process has been demonstrated with RbCs [41]. Only short time later, the formation of other heteronuclear alkali-dimers like NaCs [42] and KRb [43, 44] could be demonstrated. After the photoassociation process, the excited molecules are translationally cold with a temperature similar to that of the atomic sample. Subsequent spontaneous emission into a bound state is exploited to obtain cold electronic ground state molecules, whereas the molecules are usually not vibrationally cold. A major problem in the PA process is that PA is a long-range effect, whereas the stable vibrational motion of a ground state molecule occurs at short distances. This is the reason why the relaxation by spontaneous emission mostly leads to dissociation of the molecular state into two atoms having more kinetic energy than initially. In the heteronuclear case, the levels addressed are of much shorter range due to the van der Waals interaction ($V(R) \propto R^{-6}$) as in the homonuclear case where the resonant dipole-dipole interaction ($V(R) \propto R^{-3}$) is dominant [41]. This is the reason why heteronuclear PA is in general less efficient compared to the homonuclear case. The formation of molecules can be deduced by an observed loss in the atomic sample depending on the frequency of the PA laser. Another detection method is photoionization of the generated ground state molecules which allows direct detection of the molecules. In the cesium experiment, the molecule formation rates are in the range of 0.05 - 0.2 s^{-1} per atom leading to a molecule formation of millions per second in a MOT [45]. Similar rates were achieved with the formation of cold potassium molecules [46].
PA of atoms in a Bose-Einstein condensate has also been demonstrated using stimulated Raman free-bound transitions [47, 48] which allow to generate ground-state molecules in a well-defined ro-vibrational quantum state. An enhancement of the molecule formation process can be reached by performing PA with a coherent Raman process in optical lattices [49] exploiting the tightly confinement of atoms at the lattice sites. This technique allows to control the internal rovibronic state as well as the external center of mass quantum state of the molecules with the light fields involved [50].

1.3.2 Generation of Molecules using Feshbach Resonances

Feshbach resonances constitute a powerful tool to tune the interaction in ultracold bosonic and fermionic gases. A Feshbach resonance is a scattering resonance which occurs when the collision energy for two free atoms coincides with that of a quasi bound molecular state. Experimentally, Feshbach resonances can be induced by magnetic fields when both states involved experience a different Zeeman shift. This enables control over the sign and the strength of the cold atom interaction which is characterized by the s-wave scattering length a. The first observation of coherent coupling between atoms and molecules has been achieved by the use of time-varying magnetic fields near a Feshbach resonance in a ^{85}Rb condensate [51]. In this experiment, the number of atoms that remain in the condensate oscillates at a frequency which is in agreement with the molecular binding energy. Rapid adiabatic magnetic field sweeps across a Feshbach resonance offer the possibility to generate ultracold molecules from an atomic BEC. Usually, these molecules are in a specific highly excited vibrational state. By this technique, a pure molecular sample of 3000 molecules at a temperature of a few nanokelvin has been generated from a ^{133}Cs condensate containing 6×10^4 atoms. As the molecular magnetic moments are different from the atomic ones, the molecules could be spatially separated from the condensate by a magnetic levitation field. After sweeping the magnetic field back over the Feshbach resonance, the molecules are reconverted into atoms, and the sample is detected by absorption imaging. In a similar experiment, molecules were formed in a ^{87}Rb condensate of 10^5 atoms with a conversion efficiency of ≈7% [52]. The molecules were spatially separated from the atomic cloud by a Stern-Gerlach field. In an experiment where more than 10^5 sodium molecules in the nanokelvin regime were produced from an atomic BEC by a magnetic field sweep across a Feshbach resonance, the remaining atoms were rapidly removed by radiation pressure. By this technique, the trap loss and heating processes after molecule formation were reduced so that the pure molecular sample yielded a phase-space density greater than 20 [53]. It can be seen that molecule formation in bosonic gases occurs at low conversion efficiencies of about ≈5% and the lifetime of the produced samples, which is strongly dependent on the sample density, is in the range of a few milliseconds. A critical parameter in these experiments is the magnetic field ramp speed as for fast ramps the conversion is no longer adiabatic yielding only few molecules, whereas for slow ramps the short lifetime of the molecules becomes an issue. It is also possible to couple fermionic atoms to bosonic molecules using magnetic field sweeps. In contrast to bosonic gases, recent fermion experiments have observed molecules with lifetimes close to 1 s. Due to this, more adiabatic magnetic field ramps are possible which lead to a conversion efficiency for fermions of ≥ 50%. The long lifetime is caused by the fact that the inelastic collisions of molecules composed of fermionic atoms is suppressed by the Pauli blocking [54]. In a first experiment the formation of 2.5×10^5 molecules from an degenerate Fermi gas of ^{40}K in two different spin states has been demonstrated [55]. The molecules formed with a conversion efficiency of ≈ 50% could directly be identified by their photodissociation spectrum. The first long-lived molecular Bose gases produced from fermionic atoms were demonstrated with ^{6}Li. Molecule numbers of the order of 10^5 molecules were reached at lifetimes of the order of 1 s [56, 57, 58]. This development culminated in the emergence of a molecular BEC from a degenerate Fermi gas [59]. The molecular condensate containing 4.7×10^5 molecules at peak densities of 7×10^{12} cm^{-3} was not formed by any active cooling, but it arose from a quantum phase transition initiated by sweeping across a Feshbach resonance.

1.4 Generation of Cold Molecules

This section provides a brief overview over the rapidly growing field of cold molecule generation. The generation of cold and dense samples of naturally occurring molecules is very challenging as there is no simple extension of the laser-cooling technique to molecules. Nevertheless, several techniques have been developed yielding molecules with temperatures between 1 and 1000 mK which can be trapped, for example, in electromagnetic fields.

1.4.1 Deceleration of Supersonic Molecular Beams

Various molecular beam experiments use a supersonic seeded nozzle beam. Those beams consist of a carrier gas and a small admixture (<10%) of the target molecules which expand from a container under high pressure (1-5 bar) through a nozzle into vacuum. During the expansion, the molecular internal degrees of freedom are efficiently cooled by multiple collisions and the total energy of the molecules is converted into kinetic flow energy. After the expansion, the molecular beam has usually supersonic speed, but it has a very narrow translational velocity distribution in the beam's moving frame. With this technique, translational temperatures below 1 K and rotational temperatures below 5 K can be obtained [60]. The carrier gas is usually a noble gas which prevents the target molecules from clustering. Due to the carrier gas, the phase-space density of the target molecules in the container can be maintained in the beam. As only few rotational levels are populated (excited vibrational levels can be neglected), the phase-space density of molecules in low-lying quantum states increases enormously. In the following, several experimental methods are described which translate the high phase-space densities from the moving frame of the molecular beam into the laboratory frame.

The Stark Decelerator

The Stark decelerator exploits the fact that samples of polar molecules emerging from a pulsed supersonic beam can be decelerated (or accelerated) by time-varying inhomogeneous electric fields. The molecular beam is coupled into the Stark decelerator which consists of a series of pairs of parallel electrodes where each pair generates an inhomogeneous electric field along the beam axis. When molecules prepared in states that experience a positive Stark shift (low-field seeker) approach an electrode pair, they are decelerated by the inhomogeneous electric field as a part of the kinetic energy is converted into Stark energy (potential energy). If the field is still applied after the molecules have passed the field maximum between the electrodes, the molecules will be accelerated again until they reach their initial velocity. In a Stark decelerator, however, the electrode pairs are synchronously switched with the molecular beam sample so that the field is switched off precisely when the molecules have reached the maximum fields between the electrodes. When the field is switched off instantaneously, the molecules can not completely regain their kinetic energy and so the molecules can be efficiently decelerated and brought to a standstill. The Stark decelerator has first been demonstrated in an experiment where a pulsed beam of neutral metastable CO molecules has been slowed down from 225 m/s to 98 m/s in an array of 63 synchronously pulsed electric field stages [61]. The pulsed electric fields provide a travelling potential well in which neutral molecules can be transported, decelerated and cooled while maintaining their initial phase-space density [62]. The deceleration of molecules with a negative Stark shift (high-field seeker) as, for instance, every molecule in the ground state, is more complicated because these molecules are always attracted to the charged electrodes. Nevertheless, it has been demonstrated that high-field seekers can be decelerated (and accelerated) in a Stark decelerator by using an alternate gradient focusing technique [63, 64]. In general, the Stark decelerator technique is applicable to a wide range of molecules (for an overview see [65]) and besides CO, it has been demonstrated with ND_3 [66], OH [67] and YbF [64].

Alternative Deceleration Techniques

The availability of supersonically cooled molecules initiated the development of various methods to translate the high phase-space densities from the moving frame of the molecular beam in the laboratory frame. One method uses a counter-rotating beam source mounted on the tip of a rotor where the velocity distribution of the beam can be shifted downward or upward by the rotor speed [68]. For example, the flow velocity of a rotating seeded supersonic beam of O_2 was reduced to below 70 m/s which corresponds to a kinetic energy below 10 K. The technique is applicable to a large variety of molecules, and similar results have been obtained for CH_3F and SF_6. However, the rotor itself imposes a limit on the lowest attainable speed as the molecules which are too slow to escape from the rotor path are swatted. It is very difficult to build pulsed rotating sources, and only continuous sources were tested causing a high background pressure. Collisions with the background gas weaken the beam intensity and they are detrimental for the slow molecule harvest.
In another approach, supersonically cooled molecules are superimposed by a moving focus of a nonresonant laser beam. The focus serves as an optical dipole trap confining the slowest molecules in the moving sample. After the dipole trap and the sample overlap, the laser beam is deflected out of the molecular beam by a rotating mirror and the dipole force counteracts the centrifugal and deceleration forces. [69]. Recently, it has been demonstrated that NO molecules from an supersonic source could nearly be brought to a standstill by single "billard-like" collisions with argon in a crossed beam apparatus [70]. The velocity vector of the NO molecules is cancelled by a single collision with an argon atom when the center of mass (COM) frame velocity of the scattered NO is equal in magnitude but opposite in direction to the COM velocity of the NO + Ar COM system in the laboratory frame. In a crossed beam experiment, typical collision frequencies are of the order of $10^{13}\,s^{-1}$ and the probability for collisions yielding velocities below 15 m/s is $\approx 10^{-5}$. With this technique, densities of $10^8 - 10^9$ NO molecules per cm^3 in a single rovibronic quantum state have been achieved.

1.4.2 Filtering Slow Molecules from a Thermal Reservoir

So far, several methods were introduced which actively produce cold molecules by the various cooling techniques described in this chapter. For some applications, like, e.g., cold chemistry and high-precision spectroscopy, it is not necessary to produce cold molecules as (translationally) cold molecules are present in any thermal gas, even at room temperature. They only need to be filtered out. For this reason, already in the 1950s it was attempted to select the slowest molecules from a molecular beam using gravity. Zacharias *et al.* proposed the possibility of shooting a molecular beam vertically observing molecules of such very low velocity ($\approx$ 6 m/s) that their direction of flight is reversed by the earth's gravitational field, so that they may be detected after returning to the starting region.

With such a "fountain" experiment it was expected to achieve an enormous increase in precision in magnetic resonance experiments [71]. However, these attempts failed, mostly because the slow molecules were kicked out of the beam by the fast ones in the source region. Additional problems have been caused by the large loss in beam intensity in the proposed scheme and by the background pressure affecting the molecules' mean-free path. The following section describes a novel technique for filtering polar molecules from a thermal reservoir which is the subject matter of this thesis.

1.5 This Thesis

This thesis describes a method where the Stark interaction of polar molecules with electric fields is exploited to filter translationally cold molecules effusing from a thermal reservoir. The effusion of the molecules out of the reservoir occurs under molecular flow conditions which means that the pressure in the exit channel has to be reduced so far that the mean-free path is large compared to the channel dimensions. Under this condition, the effusion does not disturb the thermal equilibrium in the reservoir, and the molecular velocity can be described by the Maxwell-Boltzmann velocity distribution. If the mean-free path becomes comparable to the channel dimensions, the fast molecules can collide with the slow molecules inside the channel which leads to a dramatic reduction of slow molecules. When the molecules leave the reservoir, they are injected at the field minimum of a bent electrostatic quadrupole where they experience the Stark potential. For the injected low-field seeking molecules whose transverse kinetic energy is smaller than the Stark energy shift transverse trapping results, while the rest escapes. The longitudinal velocity is limited by guiding them around a bend in the quadrupole further downstream from the reservoir. The centripetal force due to the electric field gradient guides only the slowest molecules around the bend, whereas the fast ones escape. With this technique, which is applicable to any polar molecule with a sufficiently high Stark shift, molecular fluxes of the order of $10^{10}\,\mathrm{s}^{-1}$ with a motional temperature of a few K have been demonstrated using ammonia (ND_3) and formaldehyde (CH_2O). The slow molecules are used to demonstrate a new large-volume electrostatic trap which can be loaded continuously. The trapped particle number amounts to 6×10^7 at a density of the order of $10^8\,\mathrm{cm}^{-3}$. The temperature of the trapped sample is determined to 300 mK.

Chapter 2

Electric Manipulation of Polar Molecules

In general, molecules are electrically neutral but they can have an asymmetric charge distribution, with one end of the molecule more positively and the other end more negatively charged. This charge separation leads to an electric dipole moment and the molecule is called a polar molecule. The interaction of a dipole moment with an external electric field is known as the Stark effect. In this chapter, it is described how the Stark effect can be used to manipulate neutral molecules and the Stark shift is calculated for the molecules ammonia (ND_3) and formaldehyde (CH_2O).

2.1 Polar Molecules in Inhomogeneous Electric Fields

Fig. 2.1 shows a classical dipole in the inhomogeneous electric field generated by two cylindrical electrodes. The dipole is represented by a positive and a negative charge q separated by a distance d. The dipole moment is defined as $\vec{\mu} = q\,\vec{d}$, pointing from the negative to the positive charge. For instance, the dipole moment of the pyramidal molecule ammonia (NH_3) is 1.47 Debye (1 Debye= 3.336×10^{-30} Cm), corresponding to a unit charge separation of 0.36 Å. This charge separation is comparatively high on the molecular scale if one considers that the height of the pyramid is about 0.38 Å [72]. In the electric field, the two charges of the dipole are attracted and repelled by the electrodes but when the field is inhomogeneous the forces will not cancel exactly. The resultant force on the molecule depends on the orientation of the dipole moment with respect to the external field,

$$\vec{F}(\vec{r}) = q\left(\vec{E}(\vec{r}+\frac{1}{2}\vec{d}) - \vec{E}(\vec{r}-\frac{1}{2}\vec{d})\right) = \mu\,\cos\theta\,\nabla|\vec{E}(\vec{r})| \tag{2.1}$$

where θ is the angle between the dipole and the electric field lines. If the dipole moment is oriented parallel (antiparallel) to the electric field lines, the dipole experiences a net force towards higher (lower) electric fields. In order to compare the force on a charge

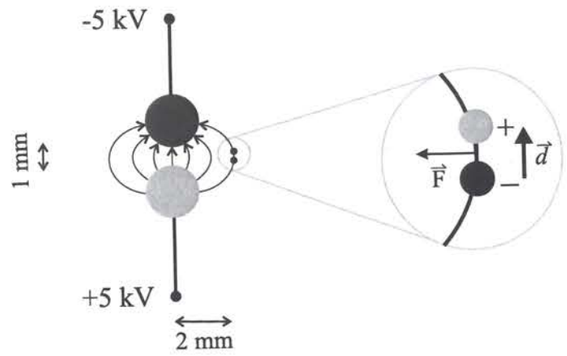

Figure 2.1: *Classical dipole in an inhomogeneous electric field generated by two cylindrical electrodes. When the dipole moment is oriented parallel (antiparallel) to the electric field lines, the dipole experiences a net force towards higher (lower) electric fields.*

with the force on a molecular dipole, both values are estimated for the situation shown in Fig. 2.1. The force on the unit charge at each end of the dipole amounts to 0.35 pN, whereas the force on the ammonia molecule in this situation amounts to $8.3 \cdot 10^{-9}$ pN. It is obvious that the resulting force on a polar molecule is much weaker than the force acting on each charge but, nevertheless, this force causes an acceleration of $29700\,g$. In case of the molecule, the force depends on the variation of the electric field along the distance $|\vec{d}|$ and the orientation of the molecular dipole. As the electric field tends to align the dipole along the field lines, a torque is acting on the dipole which results in a precession of the dipole around the field lines. This motion is much faster than the translational motion of the molecule and it will be neglected in the following. For the calculation of the force on the center of mass of the molecule only the time-averaged orientation of the dipole moment is used. So far, the description has been purely classical. The quantum mechanical description of a polar molecule in an electric field accounts for the fact that the projection of the molecular dipole moment with respect to the electric field can only take a discrete set of values. In the following, the Stark effect in the polyatomic symmetric top molecule deuterated ammonia (ND_3) and in the asymmetric top molecule formaldehyde (CH_2O) is described.

2.2 Stark Effect in Ammonia

Ammonia has a pyramidal structure with the N atom at the top and the three D (or H) atoms at the base. Due to this structure, the moments of inertia along the two principal axes perpendicular to the symmetry axis are equal and the rotational constant for these axes is B=5.14 cm^{-1}, whereas the rotational constant for the symmetry axis is C=3.15 cm^{-1} [72]. The rotational energy levels (in units of cm^{-1}) can be calculated from:

$$W_{\mathrm{rot}} = BJ(J+1) + (C-B)K^2 \tag{2.2}$$

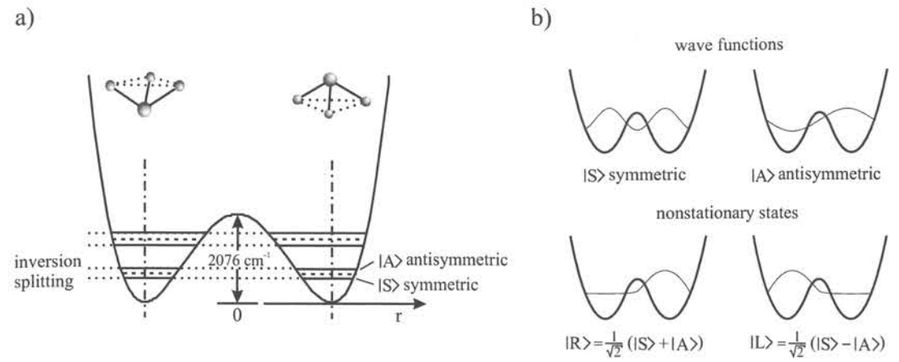

Figure 2.2: *(a) Potential energy of the ν_2 (umbrella) mode with the two lowest lying states $|S\rangle$ (symmetric) and $|A\rangle$ (antisymmetric). In the lowest state, the splitting between the inversion levels is 0.053 cm^{-1} and 0.79 cm^{-1} for $^{14}ND_3$ and $^{14}NH_3$, respectively. For NH_3, the double-well potential hill amounts to 2076 cm^{-1}. (b) The double-well potential with the lowest lying states is shown. In the unperturbed system, the wave function of the system can be described by a superposition of $|S\rangle$ and $|A\rangle$ which leads to the nonstationary states $|R\rangle$ and $|L\rangle$.*

where J is the rotational quantum number and K is the projection of J on the molecule's symmetry axis. One of the normal vibrational modes of ND_3 is the mode where the N atom vibrates back and forth through the plane of the three D atoms which is also called the umbrella mode. The system can be described by a double-well potential and the nitrogen atom can tunnel through the base of the molecular pyramid, inverting the molecular structure. Fig 2.2 shows the potential energy of ND_3 with the two lowest lying vibrational modes. The system is invariant under parity and the two lowest lying states are a symmetric state $|S\rangle$ and an antisymmetric state $|A\rangle$. It can be calculated that the energy of the antisymmetric state E_A is slightly higher than in the symmetric state E_S. The unperturbed states can be written as linear combinations of the states $|A\rangle$ and $|S\rangle$:

$$|R\rangle = \frac{1}{\sqrt{2}}(|S\rangle + |A\rangle) \qquad |L>= \frac{1}{\sqrt{2}}(|S\rangle - |A\rangle) \tag{2.3}$$

so that the wave function is largely concentrated on the right-hand side and the left-hand side, respectively. $|R\rangle$ and $|L\rangle$ are called nonstationary states and the time evolution of these states shows that the wave function oscillates between $|R\rangle$ and $|L\rangle$ at a frequency

$$\omega = \frac{E_A - E_S}{\hbar} \tag{2.4}$$

corresponding to the tunneling or inversion frequency. For a moderately high potential barrier, as it is the case for ammonia, the inversion frequency lies in the microwave region. In case of NH_3, the inversion splitting of the vibrational ground state is $W_{inv} = 0.79\,cm^{-1}$, whereas in ND_3 the splitting is only $W_{inv} = 0.053\,cm^{-1}$ as the tunneling is suppressed. Higher vibrational states are not populated at room temperature. If the potential barrier were infinitely high, there would exist two degenerate wave functions for the N atom on

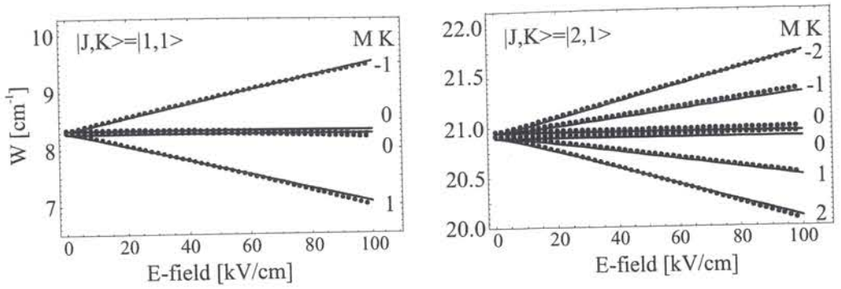

Figure 2.3: *Stark shift of the $|J,K\rangle = |1,1\rangle$ and the $|J,K\rangle = |2,1\rangle$ level of ND_3 is shown. The points denote the values obtained from a numerical calculation [73] and the lines indicate the results from eq. 2.6. Molecular states which increase (decrease) their potential energy in the electric field are low-field (high-field) seekers.*

each side of the pyramidal base and no tunneling would occur. In the following, the Stark effect in $^{14}ND_3$ is calculated. In contrast to linear molecules, symmetric top molecules can have a component of their dipole moment parallel to the angular momentum which means that it is fixed in direction rather than rotating. This is why symmetric top molecules predominantly show a first order Stark effect. In case of ammonia, the small inversion splitting plays a major role, as it has a strong effect on the Stark shift of the molecule. For two such close levels, the energy due to the electric field cannot be considered as a small perturbation. The perturbed wave functions are combinations of the unperturbed wave functions

$$\Psi_1 = a(E)|S\rangle + b(E)|A\rangle \qquad \Psi_2 = -b(E)|S\rangle + a(E)|A\rangle \tag{2.5}$$

where a and b depend on the perturbing interaction. It can be shown that for these nonstationary states, which can be written as a superposition of opposite parity states, it is permissible to have a nonvanishing permanent electric dipole moment giving rise to a linear Stark shift [74]. In electric fields below 100 kV/cm, the Stark shift can be approximated by [75]:

$$\Delta W_{Stark} = \pm\sqrt{\left(\frac{W_{\text{inv}}}{2}\right)^2 + \left(\mu\,|\vec{E}|\,\frac{MK}{J(J+1)}\right)^2} \tag{2.6}$$

where μ denotes the dipole moment, M is the projection of J on the electric field $\vec{E}$, and the plus and the minus sign are used for low- and high-field seeking states, respectively. For ND_3, the dipole moment amounts to 1.50 D, whereas for NH_3 it amounts to 1.47 D [65]. Fig. 2.3 shows the theoretical values of the Stark shifts of the $|J,K\rangle = |1,1\rangle$ and the $|J,K\rangle = |2,1\rangle$ levels of ND_3 together with the values obtained from eq. 2.6. It can be seen that theoretical values are well described by the approximate values for electric field strengths below 100 kV/cm. Due to the small splitting, W_{inv}, about 76% of the molecular states of ND_3 in a thermal ensemble show a Stark shift which deviates less than 0.005 cm^{-1} from the linear behavior at electric fields 10 kV/cm<E< 100 kV/cm. This is predominantly the case for states where J, $|K|$, and $|M|$ are roughly equal resulting in a

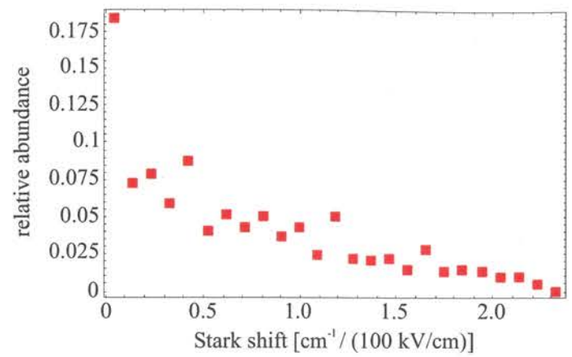

Figure 2.4: *Stark shift occurrence at a field strength of 100 kV/cm in a thermal gas of ND_3 at $T = 300\,K$. Similar shifts are gathered in small groups and every point covers a range of 0.093 cm^{-1}.*

comparatively high Stark shift. For this estimate, it has been taken into account that the inversion splitting depends on the particular quantum numbers J and K according to an approximate equation for the inversion splitting from reference [76]. Compared to ND_3, the inversion splitting of NH_3 is much higher resulting in weaker and more quadratic Stark shifts.

At room temperature, states with a rotational quantum number up to $J = 25$ occupy more than 99.99% of the population which results in a total number of more than 23400 rovibrational states. The Stark shifts of these molecular states were calculated whereas the relative occurrence of the states is given by the Boltzmann factor. Similar Stark shifts are grouped together and Fig. 2.4 shows the relative occurrence of these Stark shifts at electric field strength of 100 kV/cm in a thermal gas at $T = 300$ K. Grouping together the Stark shifts of the various states facilitates a better overview over the possible Stark shifts, and the shown discrete distribution is further used to assign Stark shifts to molecules in a Monte-Carlo simulation.

2.3 Stark Effect in Formaldehyde

Formaldehyde (CH_2O) belongs to the group of asymmetric top molecules which means that none of the principal moments of inertia are equal. The molecule has a planar structure and the symmetry axis is given by the line connecting the C with the O atom. The rotational constant for this axis is A=8.75 cm^{-1}, whereas the rotational constants for the axes perpendicular to the symmetry axis are B=1.12 cm^{-1} and C=1.01 cm^{-1} [77]. In case of CH_2O, the asymmetry is not very pronounced as can be seen from the similarity of the rotational constants B and C. The light H atoms bound to the C atom have only a weak influence on the rotation which is why CH_2O is a slightly asymmetric top. For asymmetric tops in general, the degree of asymmetry can be described by the asymmetry parameter $\kappa = \frac{2B-A-C}{A-C}$ with the range $-1 \leq \kappa \leq 1$, where the two end points of κ are the limiting symmetric top cases, the prolate top (cigar-shape) limit $\kappa = -1$, and the oblate

top (discus-shape) limit $\kappa = 1$. The projection K of the angular momentum J on the molecule axis is denoted by K_{-1} in the prolate limit and by K_1 in the oblate limit. For CH_2O, the parameter κ is about -0.97 indicating that the molecule is a nearly prolate top. In case of an asymmetric top, K is not a good quantum number and the pseudoquantum number $\tau = K_{-1} - K_1$ is introduced. The asymmetric top wave functions are denoted $|J_{K_{-1}K_1}M\rangle$ or $|J_\tau M\rangle$, and this designation provides sufficient information to determine the symmetry of the wave function. In the language of group theory, CH_2O belongs to the symmetry group D_2. The lab frame F is defined by $F \equiv X, Y, Z$, whereas the molecular frame g is defined by the principal axes $g \equiv a, b, c$. In the following, the calculation of the rotational energy levels and the Stark shift of an asymmetric top are briefly sketched, and detailed information about the calculation can be obtained from [78, 79, 80]. The rotational Hamiltonian H_{rot} of the asymmetric rotor is:

$$H_{rot} = AJ_a^2 + BJ_b^2 + CJ_c^2 \tag{2.7}$$

$$= \frac{1}{2}(A+C)J^2 + \frac{1}{2}(A-C)H(\kappa) \tag{2.8}$$

$$\tag{2.9}$$

with the reduced Hamiltonian $H(\kappa) = J_a^2 + \kappa J_b^2 - J_c^2$. In the two symmetric top limits, the rotational state eigenvalues are $W_{JK_{-1}M} = CJ(J+1) + (A-C)K^2$ for $\kappa = -1$ and $W_{JK_1M} = AJ(J+1) + (C-A)K^2$ for $\kappa = 1$. The eigenfuctions of the symmetric top are

$$\Psi_{JKM} = \Theta(\theta)e^{iM\phi}e^{iK\chi} \tag{2.10}$$

where θ, ϕ and χ are the Eulerian angles connecting the lab frame with the molecular frame and Θ is a rather complicated function which can be obtained from [75]. Note that no analytic solution for the asymmetric top energy eigenvalues can be obtained. The asymmetric top wave functions $A_{J_\tau M}$ can be described as superpositions of symmetric top basis functions

$$A_{J\tau M} = \sum_K a_K^{J\tau M}\Psi_{JKM}. \tag{2.11}$$

All $A_{J\tau M}$ belong to the symmetry group D_2 which means that the symmetry of the wave functions can be described by the representations of D_2.
In the following, the Stark shift of CH_2O is calculated. The magnitude of the permanent electric dipole moment of CH_2O, which has only a component along the principal axis a, is $\mu_a = 2.34\,\text{Debye}$. An electric field E is defined to be directed along the lab frame quantization axis Z. The direction cosine matrices, Φ_{Zg}, connect the components of E to the molecular framework. The Stark Hamiltonian is

$$H_S = E\sum_g \mu_g \Phi_{Zg} \tag{2.12}$$

The matrix elements for Φ_{Zg} are

$$\langle J\tau M|\Phi_{Zg}|J'\tau'M'\rangle = \langle J|\Phi_{Zg}|J'\rangle\langle JM|\Phi_{Zg}|J'M\rangle\delta_{M,M'} \tag{2.13}$$

$$\times \sum_{KK'} a_K^{J\tau M} a_{K'}^{J'\tau'M'}\langle JK|\Phi_{Zg}|J'K'\rangle \tag{2.14}$$

Element	J'=J-1	J'=J	J'=J+1
$\langle J\|\Phi_{Fg}\|J'\rangle$	$\frac{1}{4J(4J^2-1)^{1/2}}$	$\frac{1}{4J(J+1)}$	$\frac{1}{4(J+1)[(2J+1)(2J+3)]^{1/2}}$
$\langle JK\|\Phi_{Fz}\|J'K\rangle$	$-2(J^2-K^2)^{1/2}$	$2K$	$2[(J+1)^2-K^2]^{1/2}$
$\langle JM\|\Phi_{Zg}\|J'M\rangle$	$-2(J^2-M^2)^{1/2}$	$2M$	$2[(J+1)^2-M^2]^{1/2}$

Table 2.1: *Direction cosine matrix elements adapted from reference [80].*

and the terms are supplied in table 2.1. Note that E can mix only $\triangle J = 0, \pm 1$, $\triangle K = 0$, and $\triangle M = 0$. For the evaluation of the matrix elements, the symmetry of the wave functions plays a key role. In order for $\langle J\tau M|\Phi_{Zg}|J'\tau'M'\rangle \neq 0$, $\langle J\tau M|\mu_g|J'\tau'M'\rangle$ must belong to the totally symmetric species of the D_2 point group. Diagonalizing the Stark matrix yields the shifts in the energy levels as the field strength is varied. Fig. 2.5 a) shows the Stark energy curves of several states $|J\tau M\rangle$ of CH_2O. In the calculation J values up to $J = 5$ are included. The calculated energy shifts are in good agreement with the Stark energies from reference [80]. Although some of these states clearly have bent Stark curves, the majority of states at higher J values can be very well approximated by linear Stark shifts as can be seen in Fig. 2.5 b).

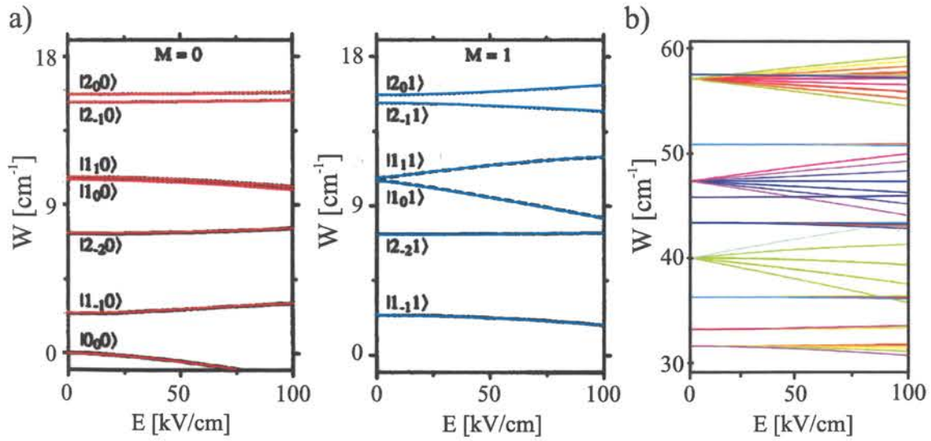

Figure 2.5: *(a) Stark energy curves of several states $|J\tau M\rangle$ of CH_2O are shown. The black lines denote the Stark energies from reference [80] whereas the colored lines denote the results from the recipe detailed in the text. Here, the calculation includes J values up to $J = 5$. (b) Stark shifts of various states are shown and the linear character of the shifts is visible. Different colors are chosen for a better visibility.*

2.4 Deflection and Focusing of Polar Molecules

The Stark effect can be exploited for filtering and focusing polar molecules in inhomogeneous electric fields. These techniques are frequently applied in state-selected scattering experiments as well as in precision spectroscopy experiments. Depending on the orientation of the molecular dipole with respect to the electric field, molecules in different states experience different forces. Therefore, an inhomogeneous electric field can be used as a filter which deflects molecules in unwanted states. However, most molecular beam experiments where state selection is simply based on deflection, suffer from the fact that the beam intensity after deflection is very poor. In order to enhance the beam intensity, it has been demonstrated by Friedburg and Paul *et al.* that a diverging atomic beam can be focused due to the interaction of the atoms magnetic moment with an inhomogeneous magnetic field [81, 82]. In contrast to atoms, the use of inhomogeneous magnetic fields for molecular state selection is not very effective because molecular magnetic moments are typically only of the order of a nuclear magneton which is small compared to a Bohr magneton. Analogous to the technique developed for atoms, intensity enhancement and state selection in a molecular beam has been achieved by electric focusing which was developed independently by Gordon, Zeiger, and Townes (1954) [83] and by Bennewitz, Paul, and Schlier (1955) [84]. Townes *et al.* used an electrostatic quadrupole to focus NH_3 molecules in the upper inversion states (low-field seeker) into a microwave cavity in order to achieve Microwave Amplification by Stimulated Emission of Radiation (MASER) [85]. In a focusing experiment, molecules with a narrow velocity spread are injected in a quadrupole or a higher order multipole, consisting of equally spaced parallel cylindrical electrodes which are lying on the outside of a circle. Neighboring electrodes carry high voltages of different polarity which results in a field minimum along the molecular beam axis. The field rises with the distance r from the beam axis according to a $r^{\frac{n}{2}-1}$ dependence where n is the number of poles involved [86].

Focusing of high-field seekers is much more difficult as Maxwell's equations do not allow for an electric field maximum in free space. Therefore, high-field seekers are immediately lost on the electrodes where the fields are the highest. In order to avoid this, a method which allows focusing of high- and low-field seekers has been proposed by Auerbach *et al.* [87] which is based on the use of alternating two-poles. A two-pole consists of two oppositely charged parallel electrodes with the molecular beam passing between. For a high-field seeker, optimum focusing is obtained if the beam falls into the plane containing the axis of the two electrodes; for a low-field seeker, it is obtained if the beam is oriented perpendicular to this plane. Alternating two-pole focusing schemes as shown in Fig. 2.6 consist of several (groups of) two-poles positioned along the beam axis with the orientation of successive (groups of) two-poles rotated by 90°. In each two-pole, high- and low-field seekers experience a defocusing force and this defocusing along alternating directions results in a net focusing of the molecular beam. Similar focusing schemes are used in the Stark decelerator technique. Alternating gradient focusing of polar molecules was experimentally demonstrated by Kakati and Lainé [88, 89] and by Günther *et al.* [90]. In a different approach, it has been shown that polar molecules in high-field-seeking states can be confined along the inner electrode of a charged cylindrical capacitor. As the electric field drops off according to $1/r$ with the distance r from the central wire, molecules with a

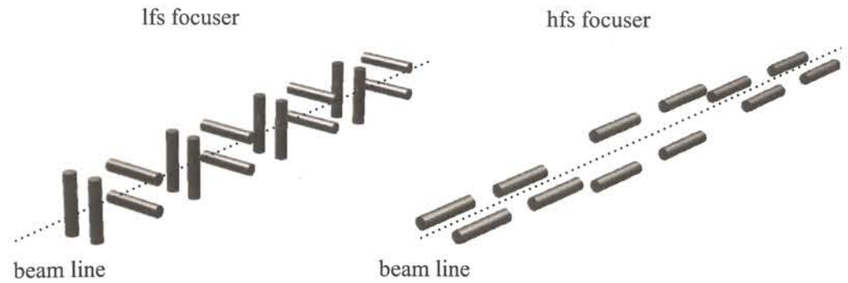

Figure 2.6: *Molecular beam focusing schemes for low-field seekers (left) and high-field seekers (right). Opposite electrodes carry high voltages of different polarity. In each two-pole, high- and low-field seekers experience a defocusing force and this defocusing along alternating directions results in a net focusing of the molecular beam. Similar focusing schemes find their application in the Stark decelerator technique.*

linear negative Stark shift experience an attractive force proportional to $1/r^2$ towards the central wire. The molecular orbits around the wire become Kepler ellipses for suited initial conditions. This approach has recently been used by Loesch [91, 92] for state selection of molecules in high-field-seeking states.

2.5 Trapping of Polar Molecules

Multipole focusers can be regarded as two-dimensional traps for low-field-seeking molecules. This trapping scheme can be extended to three dimensions by bending the multipole focuser into a torus which results in a storage ring for polar molecules [93]. By the development of the Stark decelerator technique, it has been possible to load a sample of 10^6 state selected ammonia molecules with a velocity about 100 m/s into a 25 cm diameter hexapole ring [94]. Similar to the upper case, it is also possible to build an alternate gradient circular system. Such a system combines deflection fields which are responsible for the circular motion with curved or straight alternate gradient lenses, compensating for the divergences caused by the deflection field [87]. In addition, this technique also allows focusing in forward direction or "bunching" [62] as well as deceleration and acceleration when the two-pole lenses are suitably switched [63, 95]. A three-dimensional electrostatic trapping scheme for molecules and neutral excited atoms has been proposed by Wing [96]. Molecules and excited atoms can have a positive Stark shift and they can be trapped near the electric field minimum of an electrostatic quadrupole trap. Bethlem *et al.* demonstrated that trapping of a molecular sample in low-field-seeking states is possible in such a trap [65, 66]. Stable trapping of high-field-seeking particles like ground state atoms or molecules is not possible in static fields as the Maxwell equations do not allow for an electric field maximum in free space. In order to avoid this problem, various trapping schemes for high-field seekers have been proposed which use a central charged wire with nonuniform cylindrical symmetric outer electrodes [97, 98] similar as in the cylindrical capacitor case

[92]. In these schemes, the repulsive centrifugal potential created by the particle's angular momentum prevents it from hitting the central wire. Stable three-dimensional trapping of high- and low-field-seekers can be obtained in time-varying electric fields [99, 100] which is similar to the trapping of ions in a Paul trap. The technique uses oscillating saddle-point electric field configurations and trap depths of about 5 mK were achieved for ammonia molecules [101].

Chapter 3

Filtering and Guiding Slow Polar Molecules

3.1 Introduction

In this chapter, the theoretical and experimental aspects of the filtering and guiding method are discussed in detail. The method is based on the fact that large quantities of slow molecules are present in any thermal gas even at room temperature and it is sufficient to filter them out efficiently. In this context, molecules are considered as slow if they can be trapped with electric, magnetic or electromagnetic fields. A practical upper limit of neutral particle trap depths is in the order of a kelvin, which is most easily achieved using electric fields. If this value is translated into a light polar molecule like ammonia, it corresponds to velocities of $\approx$ 30 m/s. From the Maxwell-Boltzmann distribution at $T = 300$ K, it can be derived that the fraction of particles with a velocity below the cutoff velocity v_0=30 m/s is $\int_0^{30} 4\pi^{-1/2}\alpha^{-3}v^2 \exp[-v^2/\alpha^2]dv \approx 1 \times 10^{-4}$ in each volume element. The most probable velocity in the gas, $\alpha=\sqrt{2k_BT/m}$, where k_B is the Boltzmann constant and m the molecular mass, can be calculated to be α=500 m/s. Although being a small fraction, for a gas at standard pressure and temperature this results in a density of $\approx 10^{15}\,\mathrm{cm}^{-3}$. This small fraction but large number is the core motivation behind the attempt to efficiently filter slow molecules from a gas reservoir in thermal equilibrium. The idea for a possible experimental setup for filtering is sketched in Fig. 3.1 a). It is based on a similar filtering method exploited in an experiment where a curved magnetic octupole field is used to filter out slow lithium atoms from a thermal oven beam [102] for efficient loading of a magneto-optical trap. In this experiment, the interaction of the atomic magnetic moment with the inhomogeneous magnetic field is exploited. The method described here uses a bend electrostatic quadrupole to filter slow polar molecules from an effusive source. In an effusive source, the mean free path of the molecules is large compared to the source dimensions so that intermolecular collisions are rare. This regime is called molecular flow or Knudsen regime. Furthermore, the spatial and velocity distributions of the molecules in the source are not affected by the effusion of the molecules.

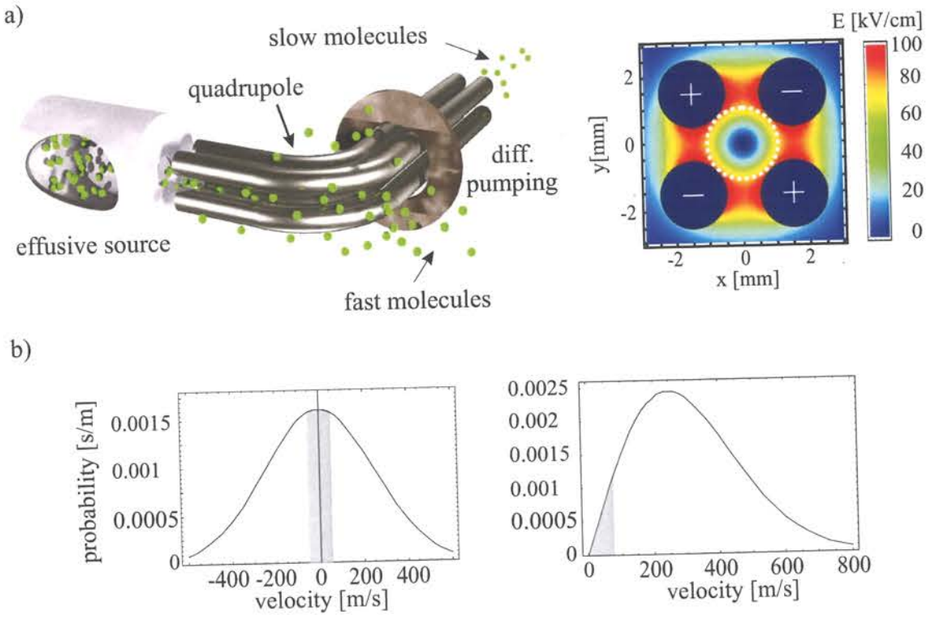

Figure 3.1: *(a) Sketch of how to filter slow polar molecules from a thermal gas. Molecules from an effusive source are injected into a bent electrostatic quadrupole with a free inner radius r indicated by the dashed circle in the field plot. Only transversely slow molecules which cannot overcome the Stark potential barrier are kept within the guide, whereas longitudinal velocity selection is provided by the bend. (b) Guided fractions are displayed as shaded regions in the transverse (left) and longitudinal (right) velocity distribution of the gas.*

For the filtering process, the Stark interaction of polar molecules with the inhomogeneous electric quadrupolar field is exploited. Molecules whose time-averaged dipole moments are oriented antiparallel (parallel) to the external electric field minimize their internal energy in weak (strong) field regions and they are called low-field seekers [lfs] (high-field seekers [hfs]). The gas is injected at the electric-field minimum of the quadrupole. For the injected low-field seeking molecules whose transverse kinetic energy is smaller than the Stark energy shift, transverse trapping results, while the rest escape. The longitudinal velocity is limited by guiding them around a bend in the quadrupole further downstream from the reservoir. In Fig. 3.1 b), the guided fraction is sketched by means of the transverse and longitudinal velocity distribution of the gas. The centripetal force due to the electric field gradient guides only the slowest molecules around the bend whereas longitudinally fast molecules escape the guide and are pumped away. Assuming a quadrupole geometry like that in Fig. 3.1 a) with a radius of curvature of 1.0 cm and an ammonia molecule exhibiting a Stark shift of, e.g., $1.0\,\mathrm{cm}^{-1}/(100\,\mathrm{kV/cm})$. Then, the maximum guidable longitudinal velocity is approximately 60 m/s. As the background pressure is comparatively high in the injection region, the slow molecules are guided through differential pumping stages into

a better vacuum to reduce losses caused by background collisions. This technique allows "on spot" delivery of slow molecules in a separate ultra-high vacuum chamber for further investigation without disturbing influences of the inlet beam.
In the following, the novel source for translationally cold polar molecules is characterized. First, the expected guidable flux of ND_3 for the relevant experimental parameters is calculated. Additionally, a Monte-Carlo simulation of the experiment is introduced which provides a deeper insight in the features of the experimental setup. Then, experimental data are shown where the flux of cold ND_3 molecules is measured as a function of the parameters: electrode voltage, gas reservoir pressure and temperature. Additionally, the results from the first guiding experiments obtained with CH_2O in a small test chamber are shown. The velocity distribution of the guided molecules is determined by a time-of-flight measurement and the exit beam angle distribution is also presented. Finally, the influence of a buffer gas admixture on the flux and the velocity distribution is analyzed.

3.2 Stark Filter

The molecules originate from an effusive source with a small exit channel through which the gas escapes from the high pressure side to the low pressure side. Directly behind the channel, the molecules are led into the quadrupole guide. It is essential that the source is maintained in the molecular flow regime, which means that the pressure at the exit channel or "nozzle" has to be reduced so far that the mean-free path exceeds the exit channel dimensions. If these conditions are ignored, the molecules will collide with each other when leaving the exit channel and the small fraction of slow molecules will be promoted to higher velocities by collisions with fast ones, effectively removing the lowest velocities in the velocity distribution of the effusing gas.
For a better understanding a reference frame is defined, in which "longitudinal" or "z" means along the guide axis and "transverse" or "x" and "y" means perpendicular to it. As the guide forms a conservative potential for the transversely slow molecules, the velocity distribution for a hypothetical gas of state-selected molecules is the Boltzmann distribution for a thermal gas,

$$P(v_\rho) = \frac{1}{\alpha\sqrt{\pi}}\, e^{-v_\rho^2/\alpha^2} \quad (|v_\rho| < |v_{max}|), \tag{3.1}$$

with the transverse velocity $v_\rho = \sqrt{v_x^2 + v_y^2}$ and the maximum transverse velocity v_{max}. This velocity depends on the Stark shift and on the distance from the injection point to the axis. Directly after injection in the guide, the longitudinal velocity distribution is the same as that of molecules in the reservoir passing through a plane from one side with velocity component v_z perpendicular to the plane:

$$P(v_z) = \frac{2v_z}{\alpha^2}\, e^{-v_z^2/\alpha^2}. \tag{3.2}$$

Longitudinal velocity filtering is achieved by bending the guide with a certain radius of curvature. If the molecule is too fast, the centrifugal force exceeds the Stark force and

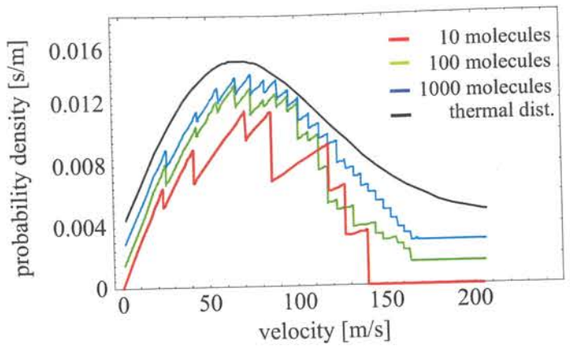

Figure 3.2: *Longitudinal velocity distributions after filtering are shown for 10, 100 and 1000 molecules with randomly chosen molecular Stark shifts out of 25 possible shifts. It is obvious that the velocity distribution shows sharp discrete structures indicating the velocity cutoffs for the particular molecular states. For 1000 molecules, it can be seen that the discrete structures are smoothed and the velocity distribution can be described by a one-dimensional thermal distribution. The remaining structure in the distribution stems from the underlying discrete state distribution used in this example. Note that the different distributions are shifted for a better visibility.*

the molecule leaves the guide. For every Stark shift there exists a maximum guided longitudinal velocity v_{lmax}. Therefore, the velocity distribution at the guide exit should show a relatively sharp cutoff if only a single molecular state is involved. As the gas consists of a mixture of states, the cutoff is smeared out and the velocity distribution can be described by a thermal distribution. The situation is illustrated in Fig. 3.2 where longitudinal velocity distributions after filtering are shown for 10, 100 and 1000 molecules with randomly chosen states according to the discrete distribution from section 2.2. The characteristic velocity of the molecules' velocity distribution before filtering is chosen to be $\alpha = 500\,\mathrm{m/s}$ in this example. The filtering details are discussed later in this chapter. It can be observed that already for 1000 molecules the velocity distribution can well be described by a one dimensional thermal distribution. The shape of the curve shown in Fig. 3.2 is briefly discussed. In case of slow velocities, molecules covering a wide range of Stark shifts can contribute to the guiding signal. However, slow molecules are rare due to the high characteristic velocity α so that the probability density is small for slow molecules. The probability density rises for higher velocities until a maximum is reached. When the velocity increases, molecules with a small Stark shift cannot be guided which leads to a reduction of the guidable molecular states. Therefore, the probability density decreases again for higher velocities as the fraction of molecules with a high Stark shift is small. The discrete structure in the distributions shown in Fig. 3.2 stems from the discrete Stark shift distribution. Under experimental conditions, these structures should vanish due to the large number of different states. Further smoothing will occur due to the molecules' transverse velocity distribution and the mixing of the transverse with the longitudinal distribution. The different potential energies of the molecules when entering the guide away from the center will also contribute to a smoothing.

The velocity distribution of the guided particles can be tuned by the guide's radius of

curvature. Choosing a large radius of curvature results in modest filtering in longitudinal direction, whereas a small radius is expected to select molecules which are slow enough for trapping in an electrostatic trap. Eq. 3.2 exhibits a unique property of the guide: the probability density rises linearly for small longitudinal velocities, compared to standard molecular beams, which show a cubic dependence. This results from the fact that the guide selects on energy and not on angle, keeping those molecules which are lost in a standard molecular beam collimated with apertures. This is the key reason for the efficiency of this guide as a continuous source for slow molecules.

3.3 Guiding Efficiency

In this section, the guiding efficiency for the relevant experimental setup is calculated [103]. The guiding efficiency is different for every gas as it critically depends on the molecular Stark shifts. Here, the calculations for ND_3 are presented and it is shown how the guiding efficiency varies with the source temperature. The results are confirmed by a numerical simulation and they are finally compared with the experimental data.

As the guided flux is one of the key parameters of the slow-molecule source, the guided fraction of ND_3 molecules emerging from an effusive source is estimated. For simplicity, it is assumed that the transverse and longitudinal degrees of freedom do not mix, i.e., a particle injected with zero transverse velocity will come out of the guide with zero transverse velocity. This is valid as long as the radius of curvature of the bend is much larger than the transverse width of the guide. However, this assumption is not exactly fulfilled in the guide used in this experiment. Most molecules enter the guide off-axis so that they already have a higher potential energy which reduces their exit velocity to $|v| < |v_{max}|$. This can be taken into account yielding a small correction which is neglected here for simplicity. In the following, we calculate a lower limit of the guided fraction assuming that the selection in z-direction is influenced by the transverse velocity and that the two transverse directions fully mix.

The longitudinal cut-off velocity, v_{lmax}, can be found by equating the centripetal force given by the Stark force with the centrifugal force, yielding $v_{lmax}^2 = v_{max}^2\, R/2r$ for a guide with the radius of curvature R and the open inner radius r. The molecules escape in the transverse direction if their total transverse velocity v_ρ exceeds v_{max}. As the filtering depends on both longitudinal and transverse velocity, for each v_z there exists a critical transverse velocity $v_{\rho max} < v_{max}$ given by $v_{\rho max}^2 = v_{max}^2 - 2v_z^2 r/R$ above which the molecule will be lost. The guided fraction of transversely slow molecules as a function of the longitudinal velocity is found from Eq. 3.1 by integrating in cylindrical coordinates:

$$\begin{aligned} f_\rho(v_z)dv_z &= \int_0^{v_{\rho max}(v_z)} 2\pi v_\rho \frac{1}{\alpha^2\pi}\, e^{-v_\rho^2/\alpha^2} dv_\rho dv_z \\ &= (1 - e^{-[v_{\rho max}(v_z)]^2/\alpha^2}) dv_z. \end{aligned} \tag{3.3}$$

The total guided flux as a fraction of the input flux in this limit can be written as a function of v_{max} alone and is obtained by integrating this result over the v_z-distribution

from Eq. 3.2:

$$f = \int_0^{v_{lmax}} \frac{2v_z}{\alpha^2} e^{-v_z^2/\alpha^2} f_\rho(v_z)\, dv_z \tag{3.4}$$

$$= \frac{2r(e^{-Rv_{max}^2/(2r\alpha^2)} - 1) + R(1 - e^{-v_{max}^2/\alpha^2})}{R - 2r}. \tag{3.5}$$

The knowledge about the Stark shifts of the various molecular states is required to determine the transverse cut-off velocities $v_{\rho max}$ for the individual states. For a room temperature reservoir, the guided fraction of the lfs molecules can be calculated to be 4.0×10^{-5} for a quadrupole guide with $R = 12.5\,\text{mm}$ and $r = 1.2\,\text{mm}$ and a maximum electric field of $80\,\text{kV/cm}$. The guiding efficiency can be increased by reducing the reservoir temperature as the velocity distribution is shifted to smaller velocities. For a temperature of T=150 K, the guiding efficiency amounts to 1.5×10^{-4}. Note that the relative abundance of the Stark shifts does not change significantly compared to the room temperature distribution. From these numbers, it is obvious that it should be possible to increase the flux by a factor of approximately 3.75 by cooling down the reservoir.

3.4 Simulation of the Filtering Process

3.4.1 The Electric Quadrupole Field

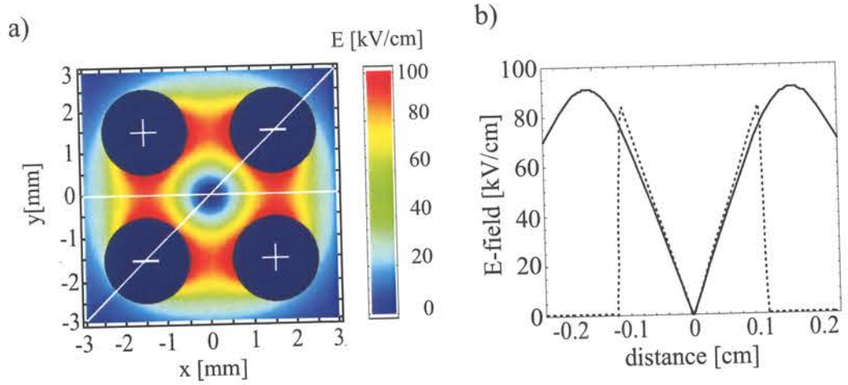

Figure 3.3: *(a) Electric field of a quadrupole with electrode radii of 1 mm and 1 mm gaps between neighboring electrodes. The electrodes carry voltages of ±5 kV which gives rise to a maximum electric field of ≈ 80 kV/cm inside the guide. (b) Electric field strength as a function of the distance from the quadrupole center along a horizontal and a diagonal field cut (see (a)). The line refers to the electric field along the horizontal cut, whereas the dashed line refers to the diagonal cut.*

In the following, a Monte-Carlo simulation of the filtering process is described were slow molecules from an effusive source are filtered in an electrostatic quadrupole guide. The

electric potential of a quadrupole is calculated with SIMION 3D software which enables to generate electrode configurations with the corresponding voltages. In order to find a suitable configuration, several quadrupole configurations with electrode diameters of the order of 1 mm have been created in an equidistant three-dimensional grid with a grid unit of 0.1 mm. The electric potential U of an electrode configuration is obtained by solving the Laplace equation

$$\Delta U(x, y, z) = 0 \tag{3.6}$$

for the particular boundary conditions. The Laplace equation is satisfied to a good approximation when the electric potential of any grid point is estimated as the average over the six nearest neighbor points. SIMION 3D calculates the electric potential with a relaxation method where the averaging process is iterated until the method converges. With the electric potential, the electric field E at each grid point can be calculated by

$$E = -\nabla U(x, y, z). \tag{3.7}$$

From the discrete electric field distribution in the three-dimensional grid, the continuous distribution is obtained by third order polynomial interpolation. Fig. 3.3 a) shows the electric field of a quadrupole consisting of 2 mm diameter electrodes with 1 mm gaps between neighboring electrodes. The electrodes carry voltages of ±5 kV which gives rise to a maximum electric field of ≈ 80 kV/cm inside the guide. This particular configuration is chosen for the filtering experiment as it provides equally high electric field maxima along the horizontal and the diagonal cut through the quadrupole field so that molecules moving in transverse direction are equally trapped. The electric field along the cut lines is shown in Fig. 3.3 b), and it can be seen that the field rises nearly linearly with the distance from the center over a wide range. Electrodes with a 2 mm diameter have been chosen as they provide sufficiently high mechanical stability which facilitates the mounting and they are flexible enough for bending even small radii of curvature.

In the simulation, the propagation of molecules in a double bent electrostatic quadrupole guide is simulated from the instant of injection by the nozzle until they leave the guide. The double bend structure has been chosen in order to achieve better vacuum conditions in the detection region (see section 3.5). Those molecules which are kept within the guide are collected behind the quadrupole exit and they provide essential information about the filtering and guiding process. The electric field calculation of the double bend quadrupole in a single rectangular grid with a sufficient resolution exceeds the available computer memory. Therefore, the double bend structure is split in two bent and two linear sections and the fields in each section are calculated separately. The molecules from the nozzle are first injected into a bent section with a radius of curvature of $R_1 = 12.5\,\text{mm}$ with additional 5 mm and 10 mm long linear segments before and behind the bend, respectively. The molecular trajectories are calculated with MATHEMATICA® software. Here, the classical equations of motion are solved with a relative accuracy of more than 10^{-4} using the stiff Adams algorithm. The molecules which cannot escape the quadrupole are collected inside the quadrupole at the end of this guide section and their positions and velocities as well as their molecular state, i.e. their Stark shift, are recorded. Those molecules are then propagated through the first 50 mm long linear section where they are collected before they leave the guide. This procedure is repeated for the remaining second bend section with a radius of curvature of $R_2 = 25\,\text{mm}$ and the last 50 mm long linear

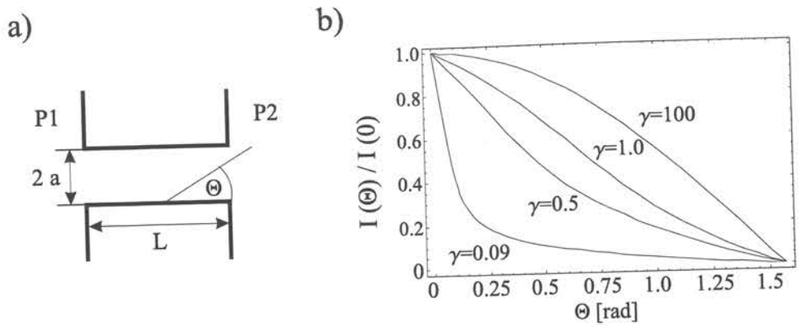

Figure 3.4: *(a) The effusive source consisting of a cylindrical tube with length L and radius a separates the high pressure side P1 from the low pressure side P2. (b) Angle distributions of the effusing molecules for different nozzle parameters* $\gamma = \frac{2a}{L}$. *For short nozzles* ($\gamma \to \infty$), *the angle distribution approaches the cosine law which is valid for an effusion through an orifice, whereas for long nozzles, the distribution is peaked in forward direction.*

section. At the end of the second linear section, the molecules can exit the guide so that their motion towards the detector can be simulated.

3.4.2 Characterization of the Effusive Source

The velocity and the angle distribution of the effusing molecules are important parameters for the simulation and they are calculated here for the nozzle assembly which is used in this experiment. At first, the angle distribution of the molecular flow emerging from a cylindrical tube with length L and radius a, sketched in Fig. 3.4 a), is calculated according to reference [104]. It is assumed that the angle distribution of the molecules entering the nozzle follows a cosine law. Under effusive flow conditions, the molecules inside the nozzle only collide with the walls from which they desorb according to a cosine law again. The angle distribution of the beam intensity I behind the nozzle is calculated from purely geometrical considerations and it can be described by the following piecewise defined function for the angle Θ:

If $p = \frac{L}{2a} \tan\Theta \leq 1$:

$$I(\Theta)d\omega = Q(p)\frac{k\dot{N}}{2\pi^2}\cos\Theta d\omega + \frac{\dot{N}}{2\pi}\cos\Theta d\omega \tag{3.8}$$

If $p = \frac{L}{2a} \tan\Theta > 1$:

$$I(\Theta)d\omega = \frac{k\gamma\dot{N}}{3\pi^2}\frac{\cos^2\Theta}{\sin\Theta}d\omega + \frac{\dot{N}}{2\pi}\cos\Theta d\omega \tag{3.9}$$

with $d\omega$ the solid angle and $\dot{N}$ the total molecular flux. The function $Q(p)$ and the

parameter k are defined by:

$$\begin{aligned} Q(p) &= \arccos p - p\sqrt{1-p^2} + \frac{2}{3}\frac{1-[1-p^2]^{3/2}}{p} \\ k &= \frac{1}{\frac{1}{3}\gamma + 2\gamma u} \end{aligned} \tag{3.10}$$

whereas γ and u are defined by:

$$\gamma = \frac{2a}{L} \qquad u = \frac{1}{4\gamma} + \frac{1}{6\gamma^3}(1 - \sqrt{1+\gamma^2}^3). \tag{3.11}$$

The molecular flux $\dot{N}$ from an effusive source can be calculated by [105]:

$$\dot{N} = \frac{2N_A\pi a^3}{3}\sqrt{\frac{8RT}{\pi M}}\frac{\triangle P}{LRT} \qquad \triangle P = P1 - P2 \tag{3.12}$$

where R denotes the gas constant, M the molecular weight in kg/mol, and N_A Avogadro's constant. Here, the units of the lengths and the pressure are meter and pascal, respectively. Fig. 3.4 b) shows the angle distributions of the effusing molecules for different nozzle parameters γ. For long nozzles ($\gamma \to 0$) the angle distribution is strongly peaked in the forward direction, whereas for short nozzles ($\gamma \to \infty$) the distribution approaches the cosine law which is valid for an effusion from a thin orifice. Note that the filtering process does not depend critically on the particular angle distribution as the guide filters on energy. For an angle distribution with a pronounced forward peak, the filtering mainly occurs in the bend section of the guide, whereas for a cosine-distribution, the filtering in transverse direction which occurs directly after injection becomes more dominant. From the experimental point of view, it is advantageous to choose a nozzle yielding a more peaked angle distribution so that the molecular flux which is not guided can be directed towards the input of a pump. In the experiment, a nozzle with a length of 16 mm and a diameter of 1.5 mm is chosen which correspond to a nozzle parameter $\gamma \approx 0.09$. For this experimental parameters, eq. 3.12 yields a molecular flux of the order of $10^{15}\mathrm{s}^{-1}$ at reservoir pressures of the order of 0.01 mbar. With the calculated guiding efficiency of 1.5×10^{-4} for a nozzle at 150 K, a maximum guided slow molecule flux of the order of 10^{11} molecules s^{-1} can be expected.

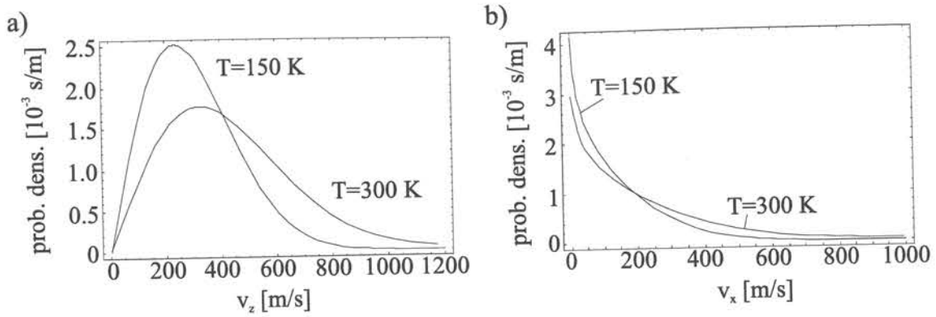

Figure 3.5: *(a) Longitudinal velocity (v_z) and (b) transverse velocity (v_x) distribution of ND_3 molecules at reservoir temperatures of $T = 150\,K$ and $T = 300\,K$, respectively. The distributions are calculated for a nozzle parameter $\gamma = 0.09$ which is used in the experiment.*

The angle distribution $I(\Theta)$ of the effusing beam allows to calculate the velocity distribution $f(\Theta, \mathbf{v})$ of the molecules which is given by:

$$f(\Theta, \mathbf{v}) = cI(\Theta) \exp\left(-\left(\frac{\mathbf{v}}{\alpha}\right)^2\right) \qquad \alpha = \sqrt{\frac{2kT}{m}}. \tag{3.13}$$

The longitudinal and the transverse velocity distribution in cartesian coordinates can be calculated to:

$$f(v_z) = c\int_{-\infty}^{\infty} dv_x \int_{-\infty}^{\infty} dv_y\, I \arccos\left(\frac{v_z}{\sqrt{v_x^2+v_y^2+v_z^2}}\right) \exp\left(-\frac{v_x^2+v_y^2+v_z^2}{\alpha^2}\right) \tag{3.14}$$

$$f(v_x) = c\int_{-\infty}^{\infty} dv_z \int_{-\infty}^{\infty} dv_y\, I \arccos\left(\frac{v_z}{\sqrt{v_x^2+v_y^2+v_z^2}}\right) \exp\left(-\frac{v_x^2+v_y^2+v_z^2}{\alpha^2}\right)$$

where c is a normalization constant. Fig. 3.5 shows the longitudinal and transverse velocity distributions for the experimental nozzle parameter $\gamma = 0.09$ for ND_3 at reservoir temperatures of $T = 150\,\mathrm{K}$ and $T = 300\,\mathrm{K}$, respectively. It is obvious that the velocity distributions shift towards lower velocities for lower temperatures which leads to an enhancement of the guiding efficiency.

In the simulation, the molecular trajectories start from a 1.5 mm diameter circular area modelling the nozzle open cross section which is placed 0.5 mm away from the quadrupole entrance. This gap between the nozzle and the quadrupole is required in the experiment to avoid heat transfer to the cold nozzle. The starting positions are equally distributed over the circular area and the initial longitudinal and transverse velocities are randomly generated according to the upper velocity distributions. The molecular state, i.e. the Stark shift, is randomly assigned to each molecule according to the distribution shown in Fig. 2.4. As the maximum Stark shift and the quadrupole parameters do not allow guiding molecules with longitudinal (transverse) velocities above 120 m/s (60 m/s), only velocities

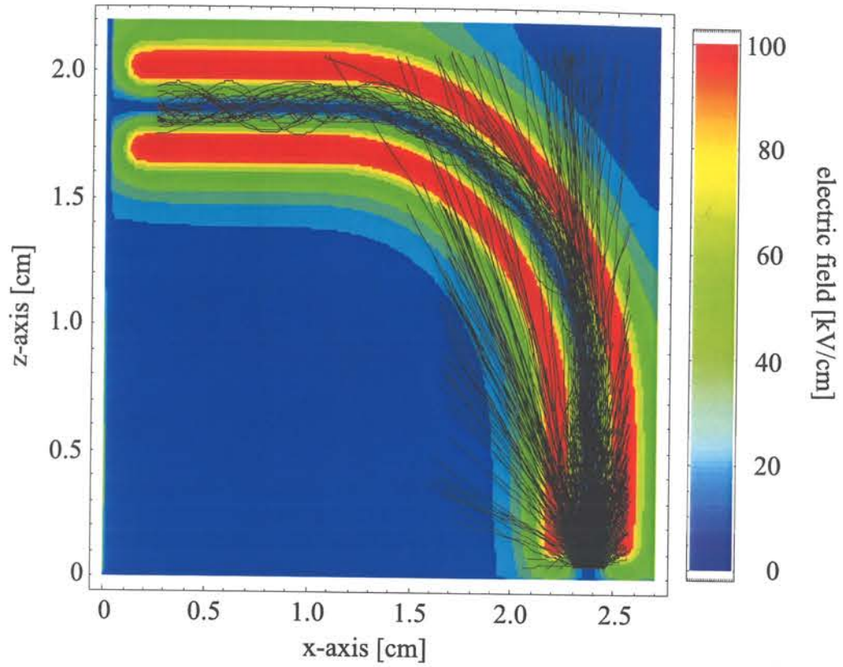

Figure 3.6: *The filtering process in a bent quadrupole is simulated. A cut through the middle plane of the quadrupole field is shown together with the projections of 1000 molecular trajectories on this plane. The molecules with longitudinal (transverse) velocities below 120 m/s (60 m/s) emerge from an effusive source at $T = 300\,K$. For a better visibility, the trajectories of molecules which are not guided are interrupted when they leave the quadrupole.*

below these threshold values are used in the simulation. Fig. 3.6 shows 1000 trajectories of ND_3 molecules from a reservoir at $T = 300\,\mathrm{K}$ propagating through the first bent section with a radius of curvature of $R_1 = 12.5\,\mathrm{mm}$. Until an amount of 5000 molecules is collected after the first bend section, a calculation time of $\approx 2\,\mathrm{h}$ is required. The propagation of these ensembles containing 5000 molecules through the remaining quadrupole sections also takes about 2 h. In order to keep the computing time in a tolerable limit, the simulation was performed on several computers in parallel.
In a simulation where more than 10 millions molecules are injected into the quadrupole, it is obtained that from a room-temperature reservoir a fraction of 6.3×10^{-5} molecules can be guided, whereas for a source temperature of $T = 150\,\mathrm{K}$ the fraction rises to 2.2×10^{-4}. Obviously, the absolute fractions from the simulation exceed those obtained from the approximate analytical calculation by a factor of ≈ 1.5. This difference can be caused by the fact that the analytic estimate yields a lower limit of the guiding efficiency. Nevertheless, the increase in guiding efficiency by a factor of ≈ 3.5 in the simulation when the temperature is lowered is in good agreement with the analytical estimate from section 3.3.

3.5 Experimental Setup

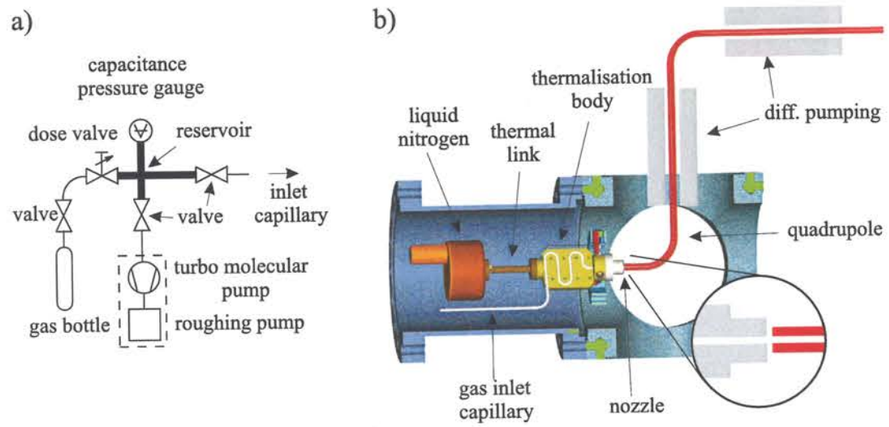

Figure 3.7: *(a) Schematic view of the gas preparation stage and the room-temperature gas reservoir. The gas of ND_3 molecules is obtained from a bottle and a controllable dose valve maintains a constant gas flow into the reservoir. The reservoir is under fine vacuum and it can be evacuated by a turbo molecular pump. (b) Cut through the gas inlet chamber of the experimental setup. The liquid nitrogen cooling stage with the connected gas inlet system and the quadrupole is shown. Gas enters the chamber in a thin flexible teflon tube which passes through a copper block before it ends in the exit nozzle. The copper block with the nozzle assembly is connected to the liquid nitrogen reservoir via a thermal link and heating elements allow nozzle temperature variations from 100 K to 400 K. The nozzle assembly, highlighted in the inset, is aligned to the quadrupole axis. Between the quadrupole electrodes and the ceramic source assembly there is a gap of 0.5 mm.*

The experimental setup of the cryogenic source for cold molecules is shown in Fig. 3.7 together with the room-temperature gas reservoir which is connected to the nozzle assembly via a long flexible teflon capillary. Fig. 3.7 a) shows a schematic view of the room temperature reservoir which satisfies fine vacuum conditions ($10^{-1} - 10^{-4}$ mbar). In case of ND_3, the gas is obtained from a bottle with a vapor pressure of ≈ 8 bar above the liquid phase. This pressure is reduced down to 0.5 bar by a reduction valve, and with a further controllable dose valve a constant pressure of the order of 0.1 mbar is maintained in the reservoir. The reservoir can be evacuated by a turbo molecular pump. When formaldehyde is used, the powdery formaldehyde trimer is heated above 90°C in a bottle in order to obtain gaseous formaldehyde monomers. The gas flow into the reservoir is controlled by a dose valve keeping the reservoir pressure constant.
Fig. 3.7 b) shows the setup in the high vacuum chamber consisting of the cooled nozzle assembly and the electrostatic quadrupole. The ceramic nozzle is mounted on a heatable copper block which is connected via a thermal link to a liquid nitrogen reservoir. For an effective cooling of the gas, the teflon capillary (ø= 1.5 mm inner diameter) is guided along

a winding path of ≈ 8 cm length inside the copper block before it flows through the nozzle with an inner diameter of 1.5 mm. The conductance F of the capillary can be obtained from standard textbook expressions [106] and it amounts to $\approx 10^{-3}$ liter/s. This value corresponds to a capillary flow impedance of 10^3 s/liter. With the conductance, the flow rate through the system can be determined which allows to calculate the local pressure at every point along the inlet capillary. For a pressure drop of 0.1 mbar along the capillary, the throughput Q is of the order of 10^{-4} mbar liter/s. The thermal link connecting the nozzle with the liquid nitrogen reservoir consists of a 5 mm diameter and 7 cm long flexible copper wire. The wire dimensions are chosen in a way that without heating an equilibrium temperature of ≈ 100 K can be reached. To minimize the thermal contact, the nozzle assembly is held by three glass balls which are mounted on plastic screws embedded in a metal ring. With the additional heating provided by a thermocoaxial cable inside the copper bloc the nozzle temperature can be varied between 100 K and 400 K. In order to provide a long term cooling of the nozzle assembly, the liquid nitrogen reservoir is filled from an external 10 l reservoir. When the nozzle is heated to a temperature of 150 K, the consumption of liquid nitrogen amounts to ≈ 1 l per day.
Between the quadrupole electrodes and the nozzle a gap of 0.5 mm exists to avoid heat transfer. The quadrupole is formed by 50 cm long and 2 mm diameter stainless steel electrodes, with a 1 mm gap between neighboring electrodes. The exact alignment of the quadrupole is provided by ceramic mounts shown in Fig. 3.8 a). In the ceramic mounts, the quadrupole electrodes are held with metallic clamps which can also be used to apply high voltages to the electrodes. Fig. 3.8 b) shows a picture of the mounted nozzle assembly and the bent quadrupole guide. The radius of curvature of the first bend is 12.5 mm and further downstream there is a second bend with a radius of curvature of 25.0 mm. Only in early measurements which will be shown in section 3.6.1 the radii were both 25.0 mm. Every bend section is followed by a ceramic differential pumping tube of ≈ 8 cm length with a cloverleaf shaped open cross section. This shape is chosen as it adapts well to the quadrupole and it allows a tight enclosure of the latter. Most of the injected molecules are not guided and escape into the first vacuum chamber, where an operational pressure of a few times 10^{-7} mbar is maintained by a 500 l/s turbo molecular pump. Behind the first differential pumping stage, a 300 l/s turbo molecular pump maintains a pressure of a few times 10^{-9} mbar. In the detection chamber, where a pressure below 10^{-10} mbar is achieved by using a 100 l/s ion pump, the guided molecules are detected with an efficiency of about 10^{-4} counts/molecule by a quadrupole mass spectrometer (QMS)[Hiden Analytical, HAL 301/3F]. In order to protect the QMS from the high voltages on the guide, a grounded 3 mm thick metallic shield with a 5 mm diameter opening is placed 2 mm behind the guide. The QMS is operated in pulse-counting mode and the pulses are recorded with a multi-channel scaler. For detecting ND_3, the QMS is set on mass 20, the dominant mass peak of ND_3. A picture of the whole setup is shown in Fig. 4.3.
The first guiding signals were obtained with CH_2O in a small test setup, and the initial results are shown at the beginning of the following section. The test setup consists of a reservoir with a ceramic nozzle (length: 1.6 mm, diameter: 0.5 mm) which injects the molecules into a 18 cm long quadrupole guide made of 1 mm steel rods with a 1 mm gap between neighboring electrodes. The guide has one bend with a radius of curvature of 13.5 mm and the molecules are guided into a separate vacuum chamber where they are detected by a QMS [Pfeiffer Vacuum, Prisma QMA 200]. For detecting CH_2O

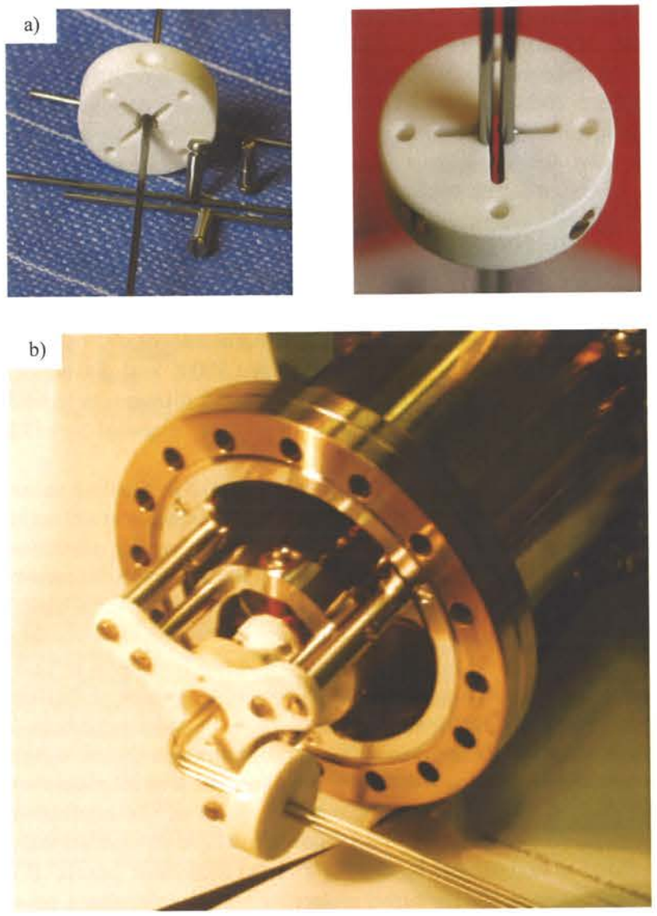

Figure 3.8: *(a) Exact alignment of the quadrupole is provided by ceramic mounts in which the quadrupole electrodes are held with metallic clamps. The clamps are also used for contacting the electrodes to high voltage. (b) Cryogenic source setup with the first bend section of the guide. The mounting scheme allows a precise positioning of the ceramic nozzle with respect to the quadrupole.*

molecules, the QMS is set to mass 29, the strongest peak in the CH_2O mass spectrum. The channeltron-amplified QMS ion current can be tapped directly for transient measurements. The reservoir pressure is of the order of 10^{-2} mbar in order to provide molecular flow conditions. In the filtering chamber, the pressure amounts to $\approx 10^{-7}$ mbar and in the detection chamber, separated from the latter by a differential pumping stage, the pressure amounts to 2×10^{-9} mbar. Further detailed information about the setup and the first experiments can be obtained from [107].

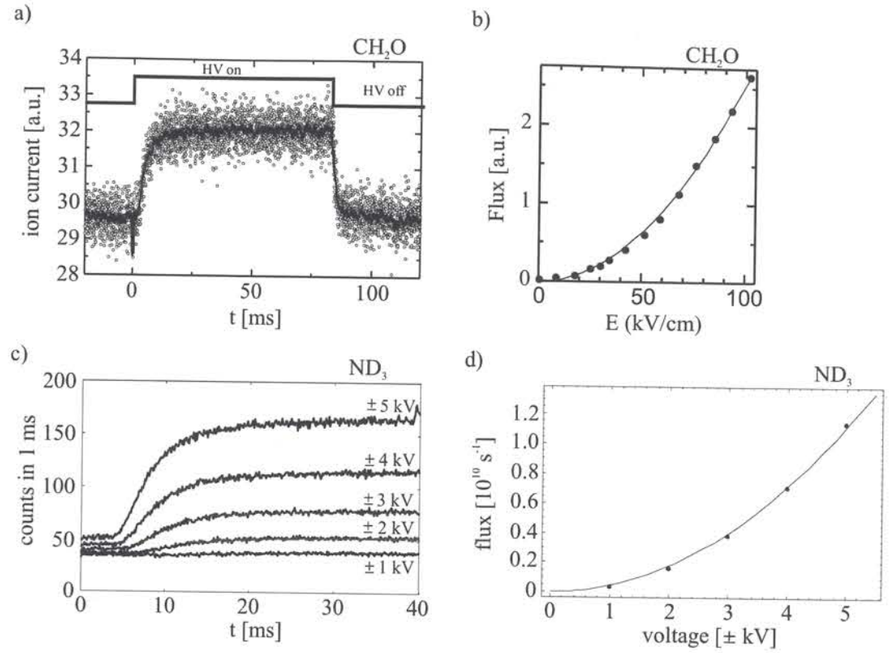

Figure 3.9: *(a) The modulation of the molecular flux when the electric field on the quadrupole in the test setup is switched. Note the delay and the relatively slow rise of the signal, corresponding to a gradual build-up of molecular flux, compared to the sudden fall due to the loss of molecules when the field is switched off. The line is a 20-point running average. (b) The flux as a function of applied electrode voltage. The symbols denote the measured height of the step function in a). (c) Detector signal as a function of the on-time of the quadrupole in the actual setup. The signal amplitude increases with the applied electrode voltages and for higher voltages the signal rises earlier. (d) The quadratic dependence of the guided flux as a function of the applied electrode voltages. The line is a quadratic fit to the data.*

3.6 Filtering and Guiding CH_2O and ND_3

3.6.1 Signal Amplitude Analysis

In a first experiment, a constant flow of formaldehyde into the test chamber is maintained. Then, the quadrupolar field is switched on and off and, after averaging over 5000 switching cycles, a modulated QMS signal shown in Fig. 3.9 a) is obtained. The quadrupole voltages were set to ± 5 kV. It has been checked that the electric disturbance from switching the high voltage does not significantly influence the signal, apart from a short spike of sub microsecond duration. As a further test that the signal represents the direct flux of the guide, a mechanical shutter has been installed that can prevent the direct flux from reaching the QMS. With the shutter blocking the direct flux into the QMS, the modulation

of the QMS signal is a factor of ≈ 5 smaller. With this test one can conclude that the observed changes in the QMS signal are due to real changes in the density of the guided gas. In a further measurement, the guiding signal was recorded as a function of the applied electric field. The signal amplitude shows a quadratic dependence on the applied electric field, as can be seen from Fig. 3.9 b). This is expected because under the assumption that the molecules show a linear Stark effect and that the longitudinal (v_l) as well as the transverse (v_ρ) velocities are much smaller than the mean thermal velocity inside the reservoir, the flux Φ in the guide is:

$$\Phi \propto \int_{v_\rho=0}^{v_{\rho max}} 2\pi v_\rho \, \mathrm{d}v_\rho \int_{v_l=0}^{v_{lmax}} v_l \mathrm{d}v_l \propto {v_{\rho max}}^2 {v_{lmax}}^2 \propto E^2, \tag{3.15}$$

where E is the depth-determining electric field strength. Eq. (3.15) is valid for every molecule with a linear Stark shift, and therefore also for an ensemble of molecules with different, but linear, Stark shifts. By calibrating the QMS ion current with the partial background pressure of CH_2O it can be estimated that the guided flux amounts to $\approx 10^9\,\mathrm{s}^{-1}$ for electrode voltages of $\pm 5\,\mathrm{kV}$. From the guiding signal shown in Fig. 3.9 a), it can be seen that the signal-to-noise ratio is rather poor which is mainly caused by the high background pressure in the test setup. The background pressure in the detection chamber can be reduced significantly by adding a further differential pumping stage. This has led to the construction of the actual setup with the double bend structure and the two differential pumping stages. In the following, the results from the actual setup are shown which have been obtained with ND_3. Compared to CH_2O, which is obtained by heating the trimer, ND_3 is easier to handle as it can be obtained directly from a bottle. Furthermore, CH_2O can polymerize again at the reservoir walls and after a while the whole reservoir and the valves are covered with the polymer. This effect can reduce the open diameter or even clog the capillary and it affects the functionality of the dose valves. Therefore, the use of ND_3 is more convenient and because of its large and linear Stark shift it is a good candidate for further experiments.

In a first experiment with ND_3 in the actual setup, the guiding signal is recorded as a function of the applied quadrupole voltages. For this measurement, voltages between $\pm 1\,\mathrm{kV}$ and $\pm 5\,\mathrm{kV}$ were periodically applied on the quadrupole which results in a maximum field strength of $\approx 80\,\mathrm{kV/cm}$ between the electrodes at $\pm 5\,\mathrm{kV}$. As soon as the field is switched on, the slow molecules coming from the nozzle are kept within the guide. For the highest voltage it takes about 4 ms till the fastest molecules arrive at the detector. Fig. 3.9 c) shows the time-of-flight signals for the different voltages obtained after 400 switching cycles. Note that the delay in the signal rise increases as the voltage on the quadrupole is reduced, because the maximum guidable velocity decreases for smaller voltages. It can be seen that the background level of the signal traces grows with the quadrupole voltages. This is due to the different average background pressure in the detection chamber for a measurement at a particular field strength. The average background pressure depends on the guided flux which is caused by the switching and it increases when the quadrupole voltages are increased. Note that the signal-to-noise ratio has improved significantly compared to the test setup which is mainly caused by the improved background pressure. As expected for a molecule with a linear Stark shift, the signal amplitude shows a quadratic dependence on the applied electric field which is shown in Fig. 3.9 d).

3.6.2 Flux Calibration

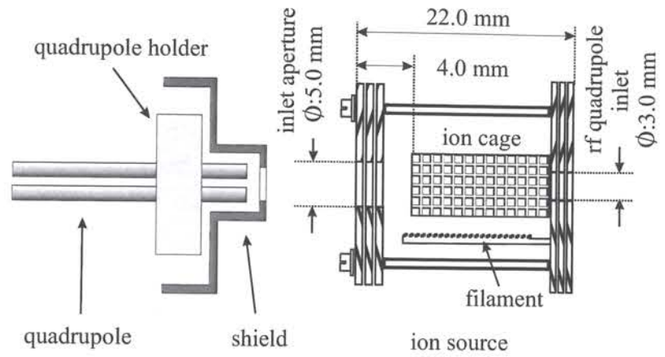

Figure 3.10: *Schematic view of the quadrupole exit and the ion source of the QMS. Behind the quadrupole, a metallic shield protects the QMS from the high voltages. The molecules from the guide enter the QMS ionization unit by the inlet aperture. Inside the ion cage assembly, the molecules are ionized by electron impact ionization and the molecular ions are focused towards the radio frequency quadrupole. The distance between the shield and the QMS can be variably adjusted and, under normal conditions, there is a 3 mm gap between the QMS inlet aperture and the shield.*

In order to calibrate the flux of the guided molecules, the sensitivity of the QMS for ND_3 is estimated under the present experimental conditions. To this end, a constant flow of ND_3 into the system is maintained and, when a certain partial pressure of ND_3 has established in the detection chamber, a mass spectrum is taken. The peaks with the strongest contribution in the mass spectrum are corrected with the particular gas correction factor [108] according to their different electron ionization probability. From the corrected mass spectrum, the relative abundance of ND_3 in the residual gas can be determined. By measuring the pressure with an ionization gauge, the total particle density can be estimated and, as the relative abundance is known, the absolute number of ND_3 molecules in the ionization volume can be determined. Our estimate results in a QMS sensitivity within a factor of two from the $\approx 10^{-4}$ counts/molecules estimate which is provided by the manufacturer, for room-temperature molecules. An accurate flux estimation also requires a solid angle correction as the guided molecules are spatially filtered by an inlet aperture (ø= 5 mm) on the QMS ionization unit. Fig. 3.10 shows a schematic view of the quadrupole exit and the ionization unit of the QMS. Under normal conditions, there is a 3 mm gap between the shield and the QMS which corresponds to a distance of $\approx 18\,\mathrm{mm}$ from the quadrupole exit and the center of the ionization unit. From the angle distribution measurement of the exit beam, shown in section 3.6.7, it is derived that a fraction of 15 percent of the guided flux reaches the detector. These corrections are employed for the flux estimation.

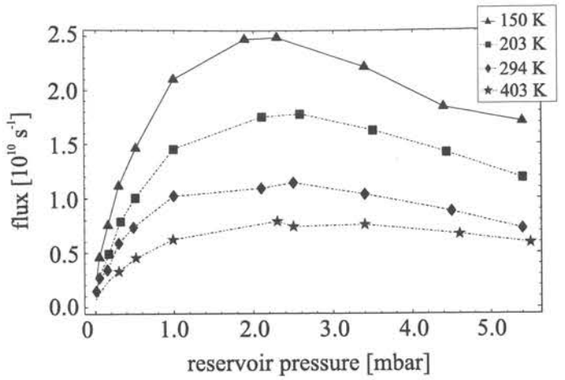

Figure 3.11: *Flux dependence on the reservoir pressure at different nozzle temperatures. For lower temperatures, the guiding efficiency is increased as long as the gas has a vapor pressure higher than the local nozzle pressure.*

3.6.3 Flux at Different Nozzle Pressures and Temperatures

The measurements were performed in a reservoir pressure range from 0.05 mbar to 5.5 mbar and the nozzle temperature has been varied between 100 K and 400 K. Some of the resulting flux curves are shown in Fig. 3.11. At first, the room-temperature curve at 294 K is discussed. For low pressures, the flux increases linearly in pressure and it starts deviating from the linear dependence above a reservoir pressure of ≈ 0.3 mbar. This leads to a pressure inside the nozzle which lies between the Knudsen regime, where the mean free path is larger than the nozzle diameter and the viscous regime, where intermolecular collisions along the capillary frequently occur. When the reservoir pressure is further increased, the guided flux reaches a maximum at 2.5 mbar. In consideration of the gas inlet stage conductance, it has been calculated that at this reservoir pressure the average pressure in the last 10 mm of the nozzle is close to 0.1 mbar. At this value, the mean-free path of the molecules is of the order of the nozzle diameter and collisions play an important role. When the pressure is further increased, collisions quickly remove the slow molecules and the guided flux decreases again.

As the guiding technique allows filtering of the slowest molecules from a thermal gas, its natural extension is that the filtering efficiency can be increased if the average velocity of the thermal gas is reduced, i.e., if the effusive source itself is cooled. The approximate analytical theory from section 3.3 shows that one can expect an increase in guiding efficiency by a factor of ≈ 3.75 when a temperature of $T = 150$ K is substituted in the model instead of $T = 300$ K. The guided flux is the product of the input from the nozzle and the guided fraction, f. For an ideal gas, it is expected that the particle flux through the nozzle at a pressure p and temperature T is proportional to $p/\sqrt{T}$. In order to see how this affects the gas input, the pressure drop in the cooled nozzle is calculated.
With the conductance, the flow rate through the system can be determined which allows to calculate the local pressure at every point along the inlet capillary. The pressure is expected to drop linearly along the warm and the cold sections of the capillary. At 150 K,

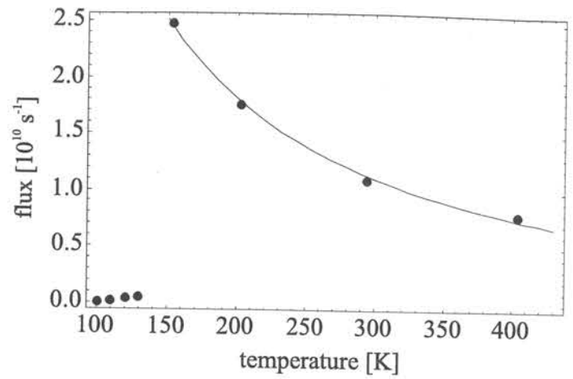

Figure 3.12: *Maximum flux at different nozzle temperatures. At 150 K, the flux reaches a maximum and it decreases for lower temperatures as the vapor pressure of ND_3 for $T < 130$ K is less than the local nozzle pressure. The black curve indicates a T^{-1} dependence for temperatures above 150 K.*

the pressure in the cold section is about 10% lower compared to the pressure at 300 K. The variations in pressure and temperature contributions compensate each other to some extend so that the flux through the nozzle is expected to increase by a factor of $0.9/\sqrt{1/2}$ according to the $p/\sqrt{T}$-dependence when the temperature is reduced from 300 K to 150 K. If this factor is multiplied with the increase in guiding efficiency, the guided flux is expected to increase by a factor of ≈ 4.8 in the case of an ideal gas.
It can be seen in Fig. 3.11 that decreasing the temperature leads to an increase in the guided flux, and the maximum flux changes in good approximation by a factor of two when the temperature is reduced from 300 K to 150 K. As the approximate analytical theory is only valid in the regime where the guided flux rises linearly with the reservoir pressure, the rising slopes of the two relevant flux curves are compared. The slope of the flux curve for 150 K rises only twice as fast as the room-temperature curve. This deviation from the model might be explained by the fact that 150 K is below the triple point of ND_3 at 195 K, and the molecules begin to stick to the capillary walls which increases the impedance of the gas inlet capillary. As the present setup does not provide access to the pressure inside the nozzle, this is difficult to verify. However, the hypothesis is supported by the different pressure rises in the first filtering chamber when injecting gas at different temperatures: At $T = 150$ K, the pressure rise is half that at $T = 300$ K for a comparable reservoir pressure, hinting to a smaller gas input at lower temperatures. The exact value and position of the maximum in the flux curve is not yet understood, but will depend on the flow dynamics of fast and slow molecules in the nozzle in the intermediate pressure regime between Knudsen and viscous flow. Also due to the lack of accurate nozzle pressures, this seems very difficult to model. Nevertheless, it is striking that the maximum flux in the curves occurs in the same reservoir pressure range.
For temperatures below ≈ 130 K no measurable guiding signal is expected, because at these temperatures the saturated vapor pressure of ammonia [109] is less than the local nozzle pressure at usual reservoir pressures and it decreases exponentially with temperature. This leads to a rapid condensing of the gas at the nozzle walls and for lower temperatures

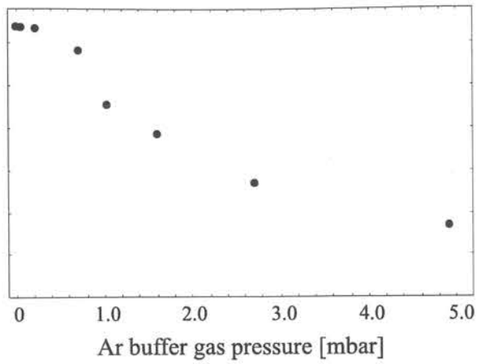

Figure 3.13: *The flux as a function of the partial pressure of the argon buffer gas that is admixed to the ND_3 gas in the reservoir. The nozzle temperature is 140 K. Clearly, the buffer gas is detrimental to the guided slow molecule flux.*

the guiding signal should fall off rapidly. Fig. 3.12 shows the maximum flux as a function of the nozzle temperature for temperatures down to 100 K. As expected, the flux vanishes for temperatures below 130 K. The range between 150 and 400 K is well fitted by a T^{-1} dependence, which is not yet understood.

3.6.4 Buffer-Gas Attempts

In an attempt to extend the reservoir cooling technique to temperatures below 150 K, a mixture of ND_3 and argon was injected through the nozzle which was cooled to a temperature of 140 K. Noble gases like argon still have a considerable vapor pressure below 150 K and the idea was that they can be used as a buffer-gas which enables thermalization of the ND_3 molecules to the nozzle temperature by collisions. Furthermore, the buffer-gas should prevent the ND_3 molecules from hitting the cold walls where the would be absorbed. The non-polar noble gases are hfs and will not be guided. For this idea to work, the partial pressure of the buffer gas has to exceed that of ND_3 by far, in order for the mean-free path of the molecules to be smaller than the nozzle diameter so that the ND_3 is prevented from sticking to the walls. Of course, this then automatically leads to a speed-up of the average output velocity by collisions, similar to the transition from an effusive source to a supersonic nozzle. A priori it was not clear which effect wins: the gain in signal because the cold molecules do not freeze out on the walls, or the loss in signal because slow molecules are removed from the nozzle and the guide by collisions with the fast buffer gas.
Fig. 3.13 shows the flux as a function of the reservoir pressure when ND_3 is injected together with argon as buffer gas. The partial pressure of ND_3 is held constant at 0.5 mbar and the pressure rise up to 5.0 mbar is caused by the argon. Clearly, the flux decreases when a buffer gas is added and therefore buffer gas addition at the temperatures just below the standard operation regime of the apparatus is not very promising.

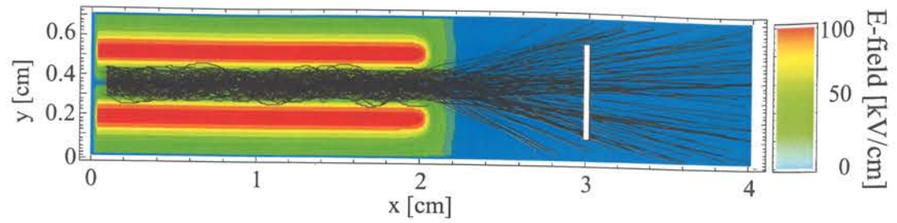

Figure 3.14: *Simulation of 100 molecular trajectories (ND_3) at the guide exit shows that several trajectories are bent away from the quadrupole fringe field which indicates that the molecules are accelerated when leaving the guide. This acceleration towards the detector results in an increased detection efficiency for the longitudinally fast molecules as the longitudinally slow molecules spread over a larger solid angle. The white bar indicates the position of the detector aperture diameter under normal conditions.*

3.6.5 Velocity Distribution

The velocity distribution of the guided molecules provides essential information about their (external) temperature and it reveals basic properties of the molecular beam. With the length of the flight path L and the rising slope of a time-of-flight (TOF) signal $S(t)$ the longitudinal velocity distribution $f(v)$ can be derived. The delay t of a signal point and the corresponding velocity v are related by $t = L/v$ and differentiation yields:

$$\delta t = -\frac{L}{v^2}\,\delta v \tag{3.16}$$

where δt is an infinitesimal time interval. The infinitesimal fraction of molecules in the interval δv is equal to the molecules contributing to the rise in the signal in the corresponding time interval δt, and thus:

$$f(v)(-\delta v) = \frac{S(t+\delta t) - S(t)}{\delta t}\delta t \tag{3.17}$$

The minus sign expresses the fact that the rise in the signal at later time intervals corresponds to the contribution of molecules in lower velocity intervals. Using eq. 3.16, the velocity distribution $f(v)$ can be written as:

$$f(v)\delta v = \frac{L}{v^2}\dot{S}(t)\delta v \tag{3.18}$$

for $\delta t \to 0$. The velocity distribution is obtained by differentiation of the signal $S(t)$ where t can be replaced by L/v. For an accurate calculation of the velocity distribution, one has to take into account several features of the interplay between guide and detector:
1.) When the molecules leave the guide, they are accelerated towards the detector by the fringe field. This can be observed in Fig. 3.14 where some trajectories are bent towards the detector when leaving the guide. The probability that the molecules enter the ionization volume of the QMS varies for different velocities, because the longitudinally slow molecules are more likely to miss the QMS entrance aperture as they spread over a larger solid

angle. The opposite is true for fast molecules. These effects become obvious in Fig. 3.15 a) where a simulated velocity distribution in the guide and behind the detector aperture are shown for ND_3. It can be seen that the fraction of slow molecules is strongly reduced behind the detector aperture and, in addition, fast molecules are more abundant. Inside

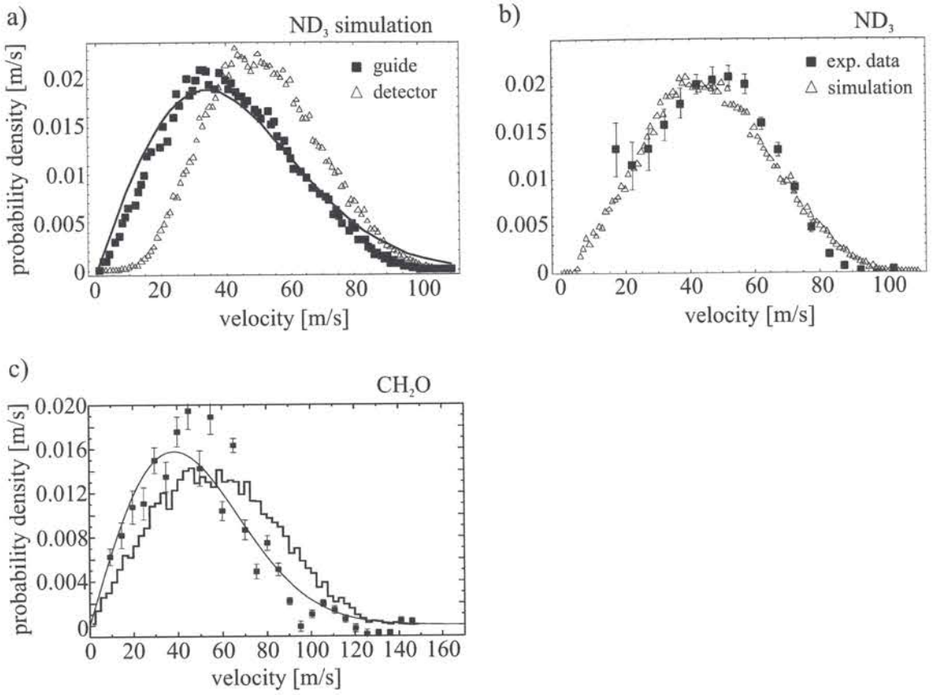

Figure 3.15: *(a) Simulated velocity distribution of ND_3 molecules in the guide and at the detector. The distribution in the guide is fitted by the functional form $(2v_l/\alpha^2)\exp[-v_l^2/\alpha^2]$ with the characteristic velocity $\alpha = 48.5 \pm 1$ m/s. At the detector, the fraction of slow molecules is reduced as they spread over a larger solid angle. Additionally, the molecules are accelerated when leaving the guide leading to a shift in the distribution towards higher velocities. (b) The measured velocity distribution (ND_3) obtained by a time-of-flight (TOF) measurement with electrode voltages of ± 5 kV at a nozzle temperature of 150 K is shown together with the simulation results. Below 20 m/s, the data points are affected with large systematic errors. The maximum of the probability density is at 50 m/s which corresponds to a one-dimensional (translational) temperature of ≈ 4 K. The error bars in the graph denote statistical errors. (c) Measured longitudinal velocity distribution of CH_2O obtained from the test setup with electrode voltages of ± 5 kV (data points with statistical error bars). The curve is a (normalized) fit to the data of the functional form $(2v_l/\alpha^2)\exp[-v_l^2/\alpha^2]$, with $\alpha = 54$ m/s, the stepped curve is the simulation result. The negative values at high velocities are due to statistical noise in the data at short times. The analysis includes corrections for the solid angle and the ionization probability*

the guide, the velocity distribution of the molecules can be fitted by a one-dimensional thermal velocity distribution with a characteristic velocity $\alpha = 48.5 \pm 1$ m/s. Note that the characteristic velocity is the most probable velocity in a volume element.

2.) The QMS ionization probability is velocity dependent because compared to the fast molecules, the slow molecules spend more time in the ionization volume and so their ionization probability is higher. This effect leads to an overestimation of the slow molecules in the detector.

Fig. 3.15 b) shows a velocity distribution of guided ND_3 molecules with electrode voltages of ± 5 kV and a nozzle temperature of 150 K. The distribution is derived from the TOF signal according to eq. 3.18. The correction for the velocity dependent ionization probability is included. Note that in the TOF measurement the average velocity of the molecules on their way to the detector is determined. The arrival time is mainly dominated by the velocity of the molecules inside the guide. The velocity distribution obtained from a TOF measurement can be simulated in the following way: Those molecules which have been propagated through the double bend quadrupole segments are injected in the 2 cm long quadrupole segment shown in Fig. 3.14. About 1 cm behind the quadrupole there is a circular area which represents the detector aperture. From the trajectories impinging on the circular area the initial longitudinal velocity (at the injection) and the flight time is recorded. With the initial velocity the flight time for a 48 cm long quadrupole can be calculated, whereas the flight time for the remaining 2 cm and the way to the detector can be obtained from the simulation. Note that the total length of the real quadrupole amounts to 50 cm. With these flight times one can calculate the velocity distribution. As can be seen from Fig. 3.15 b), the measured data is in good agreement with the distribution behind the detector aperture obtained from the simulation. Compared to the velocity distribution in the guide, the distribution from the TOF measurement is slightly shifted to higher velocities caused by the detector aperture. The velocity distribution shows a maximum near 50 m/s which corresponds to a temperature of ≈ 4 K. Below 20 m/s the data are affected with large systematic errors as the time-of-flight signal shows a small but permanent rise for later arrival times. This rise is not only caused by slow molecules because an additional local pressure increase near the detector originating from the guided molecules might play a role.

Fig. 3.15 c) shows the measured longitudinal velocity distribution of CH_2O obtained from the test setup with electrode voltages of ± 5 kV. The data can be fitted by a one-dimensional thermal distribution with a characteristic velocity $\alpha = 54$ m/s which corresponds to a temperature of 5.4 K. The data are corrected according to the ionization probability and a correction factor for the slow molecule losses caused by the detector aperture has been used.

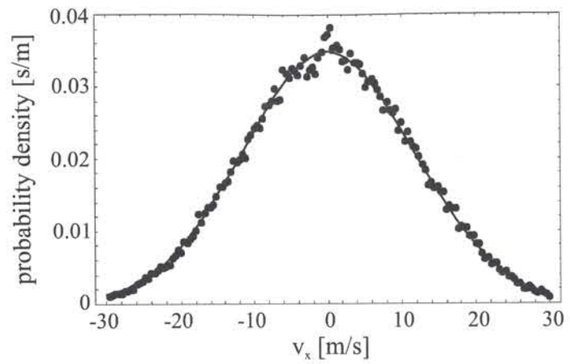

Figure 3.16: *Transverse velocity distribution of ND_3 molecules in the guide obtained from the simulation. The line is a fit of the functional form $1/(\sqrt{\pi}\alpha)\exp[-v_t^2/\alpha^2]$, with the characteristic velocity $\alpha = 16.4 \pm 0.2\, m/s$.*

Fig. 3.16 shows the transverse velocity distribution of ND_3 molecules in the guide obtained from the simulation. As expected, the transverse distribution, which can be described by a characteristic velocity $\alpha = 16.4\,\mathrm{m/s}$, is much narrower than the longitudinal distribution as transverse filtering is more restrictive than longitudinal filtering.

3.6.6 Stark Shift and Density Distribution

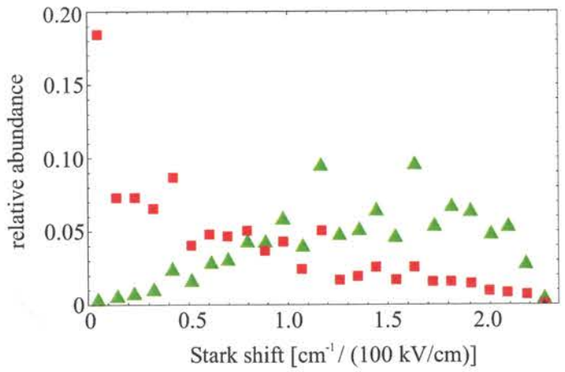

Figure 3.17: *The simulated Stark shift distribution in the guide (triangles) is shown together with the distribution in the reservoir (boxes). Similar shifts are gathered in small groups and every point covers a range of $0.093\ cm^{-1}$. Inside the guide, the Stark shift distribution is shifted to higher values as the guided beam is enriched with molecules with a higher Stark shift.*

The internal state distribution of the guided molecules is peculiar as it is enriched by states with a large Stark shift. Fig. 3.17 shows the Stark shift distribution of the guided

beam obtained from the simulation together with the distribution in the reservoir from section 2.2. Inside the guide, the Stark shift distribution has changed completely and a clear shift towards higher Stark shift values can be observed. The average of the Stark shift distribution in the guide is about $1.4\,\mathrm{cm}^{-1}$ at $100\,\mathrm{kV/cm}$.

J	0-5	6-10	11-15	16-20	>20
reservoir	15.8%	53.9%	26.2%	3.7%	0.4%
guide	7.4%	48.8%	37.6%	8.6%	0.6%

Table 3.1: *Relative abundances of the states with an angular momentum J in the reservoir and in the guided beam.*

In the following, the population of the different rotational energy levels is estimated in the reservoir and in the guided beam. The population of a rotational state in the reservoir is determined by the Boltzmann factor $e^{-W_{rot}(J,K)/kT}$ where W_{rot} denotes the rotational energy, k the Boltzmann constant and T the temperature. Additionally, the $(2J+1)$ fold degeneracy in the absence of an external field is taken into account. The number of states in the reservoir is about 23400 states when the spin statistic and states with an occurrence below 10^{-5} are neglected. In order to obtain the population of the states in the guided beam, those states with a similar Stark shift are grouped together according to the Stark shift groups in Fig. 3.17. The occurrence of the different states in the different groups is also registered and states with an occurrence below 10^{-5} are neglected. Then, the occurrence of the different states is multiplied with the relative abundance of the particular Stark class in the guided beam and the new distribution is renormalized. Finally, the occurrence of the J levels in the guided beam can be determined and the results for the reservoir and the beam are shown in Table 3.1. It can be seen that about 86% of the guided molecular states have angular momenta in the intermediate range $6 \leq J \leq 15$. Compared to the reservoir distribution, the distribution in the guide is centered in this range to a larger extent. When states with an occurrence below 10^{-5} are neglected, which are predominantly those with higher J values, the number of states in the guided beam can be estimated to approximately 4500 states. It is obvious that the number of states in the guide is much smaller than in the reservoir.

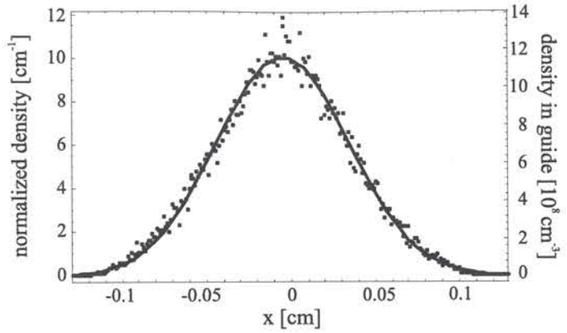

Figure 3.18: *Density of guided molecules as a function of the x coordinate inside the guide. The points denote the normalized density distribution (left axis) obtained from the simulation and the line is a Gaussian fit with a standard deviation $\sigma = 400\,\mu$m. The right axis shows the calculated molecular density in the guide for voltages of $\pm 5\,kV$ at a nozzle temperature of $150\,K$*

Another interesting feature of the guided beam is its density distribution. In order to obtain a density profile, the positions of the guided molecules are projected on the x-axis of the guide. Fig. 3.18 shows the normalized density distribution in the guide obtained from the simulation. The density distribution can be described by a Gaussian with a standard deviation $\sigma = 400\,\mu$m. The simulated density distribution and the total guided flux ϕ allow to calculate the real density distribution of the molecules in the guide. With the knowledge of the average molecular velocity in longitudinal direction ($\bar{v}_z$) and the cross-sectional area A of the guide, the average number density n can be calculated according to $\phi = n\bar{v}_z A$. Note that the average longitudinal velocity $\bar{v}_z$ can be calculated to $\bar{v}_z = \frac{1}{2}\bar{v}$ with the average thermal speed $\bar{v} = 2\alpha/\sqrt{\pi}$. The radius of the cross-sectional area A is chosen to be the standard deviation σ of the density profile. The average density of the guided molecules is distributed inside the guide according to the simulated distribution. This gives rise to a maximum density of $\approx 1.2 \times 10^9\,\mathrm{cm}^{-3}$ inside the guide.

3.6.7 Exit Beam

In order to characterize the angular distribution of the exit beam, the flux density has been measured in a plane perpendicular to the guide along two orthogonal axes x and y through the center of the guide. For this measurement, the QMS has been translated with a vacuum manipulation stage along the two axes. The flux dependence is shown in Fig. 3.19 a). It can be seen that the beam profile is slightly asymmetric which can be caused by the fact that the electrodes do not have exactly the same length. The FWHM of the distributions is approximately 1 cm at a distance of 18 mm behind the exit. At that distance, it can be calculated from the angular distribution that the fraction of the guided flux which passes the inlet aperture is about 15%. In the next measurement, the QMS is positioned in the center of the beam and the distance between the guide and the QMS is varied. For every position the flux is recorded (see Fig. 3.19 b)) and, as expected, the

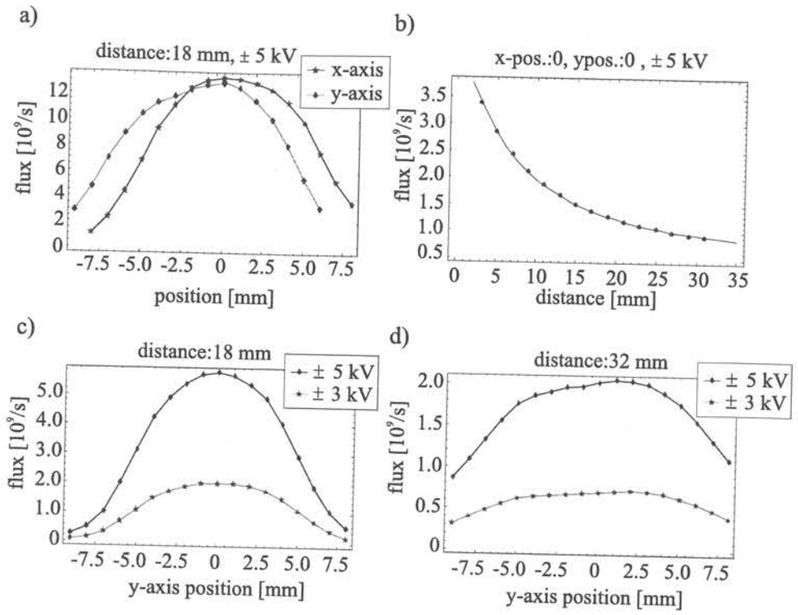

Figure 3.19: *(a) Angle distribution of the guided flux along two perpendicular axes at a distance of 18 mm between the center of the QMS ionization unit and the end of the guide. The slight asymmetry can be explained by small electrode length variations. The electrode voltages are $\pm 5\,kV$. (b) Flux as a function of the distance between the guide and the center of the QMS ionization unit at electrode voltages of $\pm 5\,kV$. The line is an inverse quadratic fit to the data. (c) Angle distribution of the guided flux along one axis with two different electrode voltages $\pm 3\,kV$ and $\pm 5\,kV$. The angle distribution remains unchanged as the lower curve is proportional to the upper curve. The same is valid for the measurement in (d) where the distance has been increased to 32 mm. Note that the pressure conditions for the different measurements were not the same.*

flux decreases according to a $1/z^2$-dependence with the distance. In Fig. 3.19 c) the beam profile along the y-axis has been measured with different electrode voltages of ± 3 kV and ± 5 kV at a distance of 18 mm between the guide and the center of the QMS ionization unit. For both measurements, the angle distribution is the same but for an overall scale factor. The same measurement has been repeated for a larger distance of 32 mm and the data is displayed in Fig. 3.19 d).

3.6.8 Alternative Guiding Prospects

So far, the quadrupole guide has been operated with electrostatic fields and efficient guiding of low-field-seeking molecules has been demonstrated. The use of electrostatic fields precludes the manipulation of high-field-seeking molecules which might play a role in the

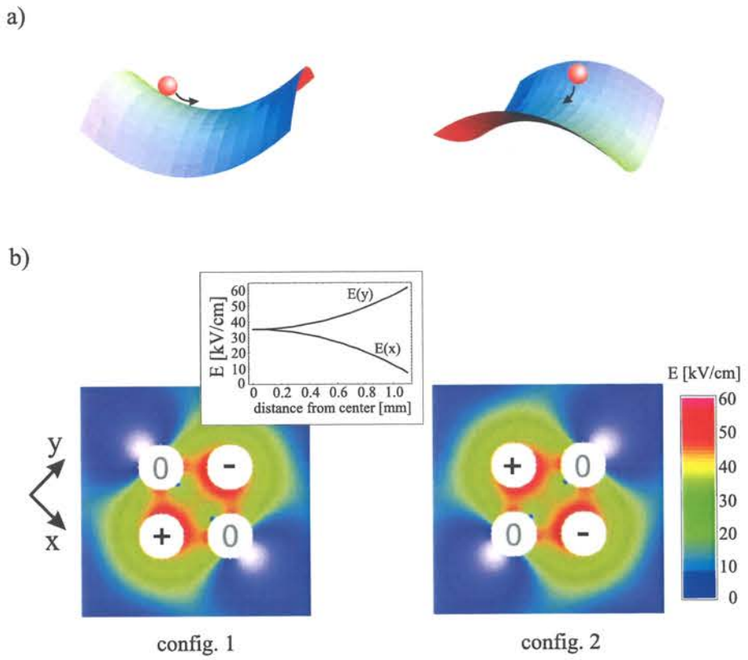

Figure 3.20: *(a) Schematic view of a particle in a saddle-like potential. Similar to the situation in an ion trap, neutral particles can be trapped in a rotating saddle-potential exploiting the Stark interaction. (b) A saddle-like potential can be realized by applying a dipolar voltage configuration to the quadrupole electrodes. A time-varying field is generated by alternating between the configurations 1) and 2) with a repetition rate in the kHz range. The inset in configuration 1) shows the electric field along the axes.*

low temperature limit as every molecule in the ground state is high-field-seeking. Compared to low-field-seekers, the manipulation of high-field-seekers is much more difficult as electrostatic maxima are not allowed in free space, and hence high-field-seekers are quickly lost on the electrodes. Furthermore, in future experiments with trapped samples of cold molecules, collisions or the interaction with light fields are likely to change the high-field-seekers into low-field-seekers and vice-versa. Due to this, a method which allows guiding or manipulating of both high- and low-field seekers is vital. In the following, a method is introduced which in principle allows simultaneous guiding of both high- and low-field-seeking molecules with the present quadrupole setup. The method is based on the use of time-varying electric fields and it has first been considered by Auerbach *et al.* [87]. Similar to the situation in the radio frequency field of a Paul trap where ions can be trapped in a rotating saddle potential (see Fig. 3.20 a)), time-varying electric fields can be used for confining neutral dipolar molecules. Fig. 3.20 b) shows 2 quadrupole voltage configurations which generate a saddle-like Stark potential for polar molecules. The time-varying field

is generated by alternating between the configurations 1) and 2) with a repetition rate in the kHz range. Independent of the slope and the sign of the Stark shift, the saddle-like dipole potential confines the particle in one direction and repels it in the perpendicular direction, depending on time. Therefore, the time average of the force is small at every position, and identical to zero for a linear Stark shift. However, the particle performs a micromotion which is locked to the external driving field so that the time-averaged force does not cancel, and the particle experiences a net attractive force towards the center. Two-dimensional trapping of polar molecules has been demonstrated in this group [110], but it is not treated in this thesis. In brief, a trapping potential of the order of 20 mK can be produced for molecules such as ND_3 with time-varying electric fields using a similar experimental setup.

3.7 Conclusions

In this chapter, a detailed overview of the theoretical and experimental aspects of filtering slow ND_3 molecules emerging from an effusive source with a bent electrostatic quadrupole guide is provided. The dependence of the filtering efficiency on the source parameters temperature and pressure is investigated and the flux of the guided molecules is measured as a function of the applied electric fields. It has been demonstrated that a flux of ND_3 of the order of $2 \times 10^{10}\,s^{-1}$ can be achieved with the presented technique which is in principle applicable to any molecule with a reasonably high Stark shift. Here, the experiments are performed with ND_3 which shows a predominantly linear Stark shift and similar results are achieved with formaldehyde (H_2CO). Furthermore, the longitudinal velocity distribution has been measured with a time-of-flight measurement and the velocity distribution of the guided molecules shows a maximum around 40 m/s. These results show that the filtering technique is able to provide a high flux of slow molecules which in principle can be trapped in the field minimum of an electrostatic trap. Even though the molecules are still hot internally, which results in a high number of internal states populated, the slow beam as it stands already offers new perspectives for experiments in interferometry and cold chemistry. Here, the focus is set on the filtering of molecules in low-field seeking states with electrostatic fields. High-field seekers, as, for instance, the ground state of any molecule, cannot be manipulated by the use of electrostatic fields. In order to extend this technique to both high- and low-field seekers, the present setup can be used to guide both species in alternating electric fields.

Chapter 4

Filtering and Trapping of Polar Molecules

4.1 Introduction

The guiding technique described in the previous chapter is applicable to a variety of polar molecules. It has been demonstrated that high fluxes of molecules like ND_3 and CH_2O with motional temperatures of a few kelvin could be filtered out from an effusive beam. This source of cold molecules is now being used to demonstrate a new trapping scheme for polar molecules.
In this chapter, a continuously operated electrostatic trap for polar molecules in low-field-seeking states is introduced. The trap is experimentally demonstrated with ND_3, but it can be used for all molecules with a sufficiently large Stark shift. In the following, the working principle and the experimental setup of the trap is detailed. Then, the experimental techniques to determine the relevant trap parameters like the lifetime, the temperature and the density of the trapped sample are described. The experimental data are discussed and they are compared with the simulation results. The chapter closes with an outlook where the perspectives of the trapping technique are discussed.

4.2 A Continuously Loadable Electrostatic Trap

In this section, a continuously loadable electrostatic trap for polar molecules, which can be adapted to a quadrupole guide, is introduced. Here, trapping is defined as the ability to store the particles much longer than it would take them to leave the trap volume in the absence of the trapping potential. In the following, the experimental setup as well as the operating mode of the trap is described. The trapping scheme is based on electrostatic principles already proposed by Wing in 1980 [96]. It confines low-field-seeking molecules in a region with low electric field strength, surrounded by a region with a high electric field.

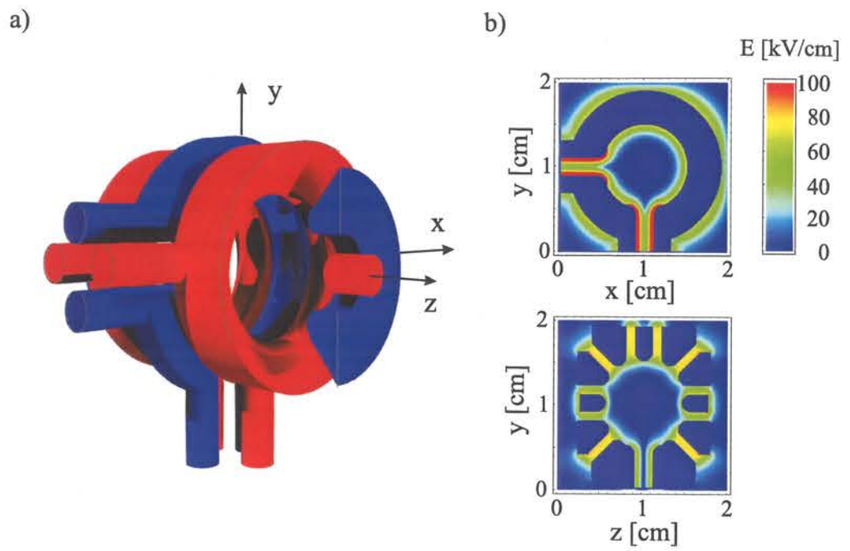

Figure 4.1: *(a) Schematic of the trap with input and detection output quadrupoles. The trap consists of 5 ring electrodes closed by electrodes with spherical end caps. Parts of the right electrodes are cut for a better view into the trap. Neighboring electrodes carry voltages of different polarity giving rise to an inhomogeneous electric field. (b) Electric field distribution in the xy plane for electrode voltages of ±5 kV (left), together with the distribution in the yz plane (right).*

The electrostatic trap, shown in Fig. 4.1 a), consists of five ring-shaped electrodes and two spherical electrodes at both ends. Neighboring electrodes carry high voltages of different polarity giving rise to an inhomogeneous electric field, illustrated in Fig. 4.1 b), which is large near the electrodes and small in the center of the trap. The central electrode is intersected two times and local thickening of the neighboring electrodes towards the gaps makes it possible to adapt two small quadrupole segments, one for filling and one for extraction of the trapped gas. The inner radii of the five ring electrodes are (2.0; 4.3; 4.8; 4.3; 2.0) mm and the two end electrodes have a diameter of 2 mm. The electrodes are separated by a 1 mm gap and the enclosed volume amounts to $\approx 0.6\,cm^3$. Fig. 4.2 shows pictures of the trap when it is built up in the vacuum system. With the present setup, a voltage difference of 10 kV between neighboring trap electrodes can be reached. This results in a minimum electric field of $\approx 40\,kV/cm$ which the molecules need to overcome in order to escape the trap in regions away from the small entrance and exit holes. At these electric fields, only guided molecules with velocities below $\approx 30\,m/s$ for ND_3 can be kept within the trap where the maximum capture velocity depends on the Stark shift of the individual molecule.
Once inside the trap, the molecules are reflected from the high electric fields close to the electrodes and, bouncing to and fro, their motion is randomized. Those molecules which can overcome the Stark potential barrier of the trap are either lost by hitting the electrodes or they escape the trap and are pumped away. The reflected molecules will bounce around

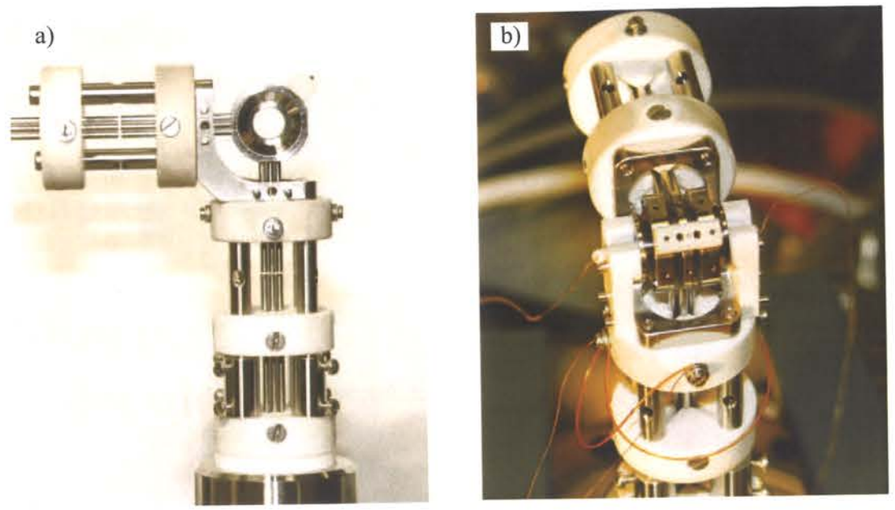

Figure 4.2: *Pictures from the trap during the assembly. (a) Side view of the trap with one conical side electrode and the end cap removed on each side. The trap is separated from the quadrupole guides by 0.5 mm gaps which allow independent switching of the quadrupole segments. Several ceramic mounts are used to provide mechanical stability and exact alignment of the quadrupole and trap electrodes. (b) View from above with all trap electrodes implemented. For exact alignment of the distance between the trap electrodes, they are mounted on a small ceramic bridge.*

until they find the entrance or exit hole. As the trap surface is large compared to the exit channel area given by the two quadrupolar openings, the probability of finding these holes is small and can even be made arbitrary small by making the trap volume and/or the electric field larger. Even though the trap allows continuous filling, the trap density is limited by the density of the incoming molecules and the trap density will equilibrate when the filling rate equals the leak-out rate.

4.3 Trapping Experiment

4.3.1 Experimental Setup

In this experiment, the trap is filled with deuterated ammonia (ND_3) from a quadrupole velocity selector. The combined setup of the trap and the quadrupole guide is shown in Fig. 4.3. In brief, a guided flux of the order of $10^{10}\,s^{-1}$ can be achieved for quadrupole voltages of $\pm 5\,kV$, resulting in a maximum electric field of $\approx 80\,kV/cm$. The guided flux consists of a mixture of states with different Stark shifts, and the longitudinal velocity distribution can be described by a one-dimensional thermal distribution with a most probable velocity of $\approx 40\,m/s$. Due to the two-dimensional confinement at finite field strengths, the

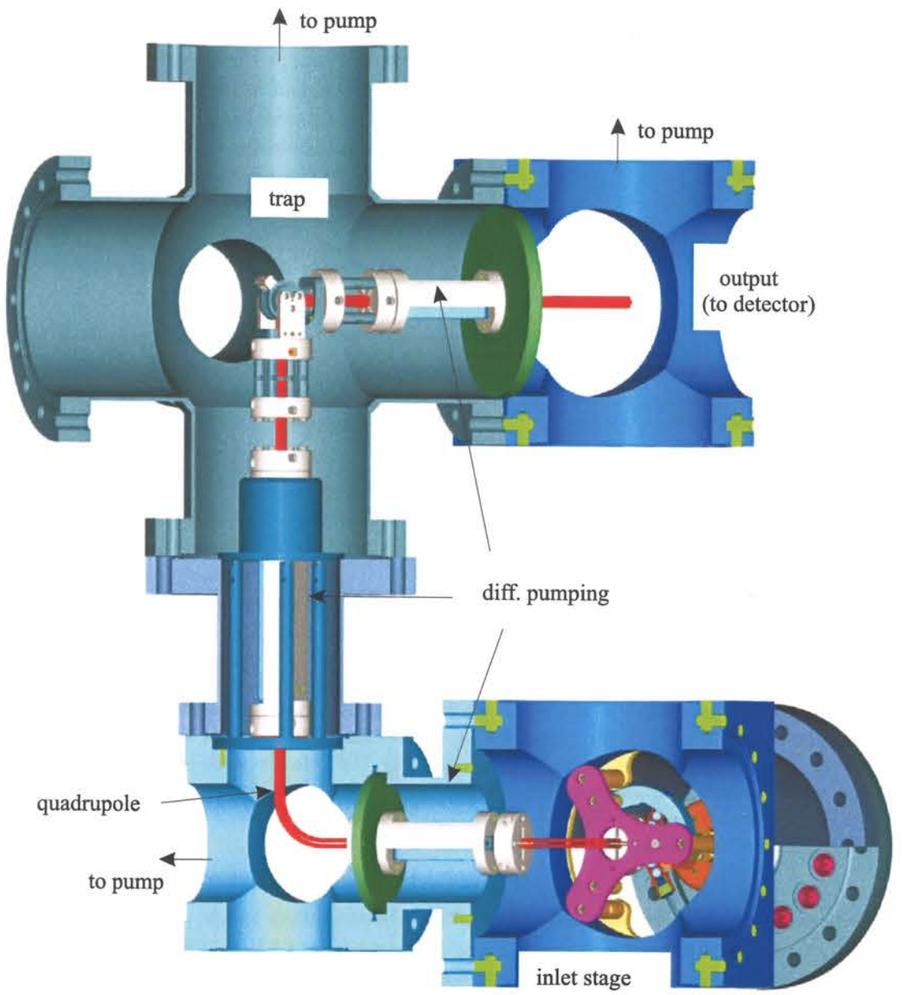

Figure 4.3: *View of the trap setup with input and detection output quadrupoles. The quadrupole guide filters slow molecules from the cooled effusive source and guides them into the trap. Here, the slowest molecules reside till they find their way out through one of the two quadrupolar guides. The trapped gas is analyzed with a mass spectrometer positioned behind the output quadrupole in a separate vacuum chamber.*

transversal velocity distribution is expected to be much narrower. Note that the internal state distribution of the guided molecules is enriched by states with a large Stark shift. As the electric field inside the quadrupole is higher than inside the trap, the molecules are accelerated when entering the trap. It follows that very low velocities are absent in the trap. The properties of the trapped sample are revealed by the molecules leaving

the trap by the 17 cm long output quadrupole. Here, the molecules are guided through a differential pumping aperture into a separate vacuum chamber where they are detected by a quadrupole mass spectrometer (QMS). Both the input and output guides are separated by a 0.5 mm gap from a short piece of a quadrupole guide formed from the trap electrodes. This separation allows independent switching of the quadrupole segments. The background pressure in the trap chamber is of the order of 10^{-10} mbar and even lower in the detection chamber.

4.3.2 Trap lifetime

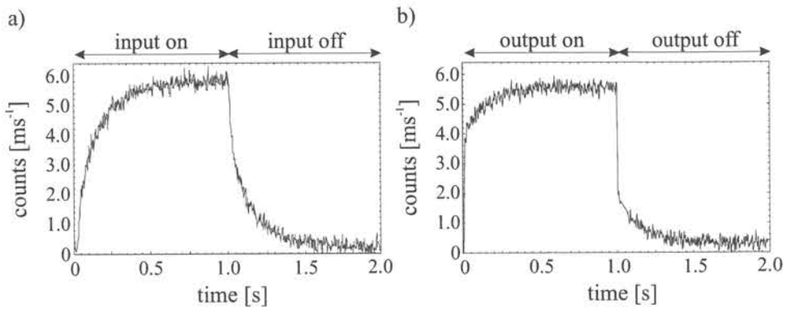

Figure 4.4: *(a) The detector signal at the output quadrupole as a function of time when the voltage at the input quadrupole is switched. As soon as the input is switched off, the signal shows a fast decay followed by a slow decay. The electrodes carry voltages of ±4.5 kV. (b) The detector response is measured by switching the output quadrupole when the trap is permanently filled. When the output is off, the signal rapidly decays, however, a small slow decay contribution can also be observed.*

In a first trapping experiment, voltages of ±4.5 kV were applied to the trap and the output electrodes while the input quadrupole was switched from 0 kV to 4.5 kV and back every 2 s. The effusive source temperature was set to a constant value of 160 K. Fig 4.4 a) shows a trapping signal which is obtained after averaging over 4000 cycles. When the input quadrupole is switched on at t=0 s, slow molecules are guided and the trap is filled resulting in an increasing signal at the output quadrupole guide. After the input quadrupole is switched off at t=1 s, a signal decay is observed which allows to estimate the lifetime of the molecules in the trap. However, it is obvious that the rising and the falling slope are significantly disturbed by a pronounced signal even 500 ms after switching on or off the input quadrupole.
At that time it is expected that the filling and emptying of the trap, respectively, is completed so that steady-state conditions are reached. Hence, a change of the output flux cannot be caused by the direct flux of molecules. At the rising slope, the excess signal might be caused by a local pressure increase near the detector after switching on the guiding process which has already been discussed in chapter 3. These molecules must be pumped away after switching off the input guide, an effect which leads to a time-dependent

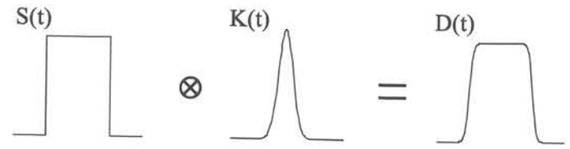

Figure 4.5: *Illustration of a convolution (⊗) process. The time-dependent rectangular signal $S(t)$ is processed in a detector with a Gaussian detector response function $K(t)$ denoting the kernel of the signal transformation. The signal at the detector output $D(t)$ is affected by the response function leading to a smoothing of the initially sharp edges.*

signal at the falling slope. These spurious signals can be measured by switching on and off the output quadrupole while the trap is continuously filled. As soon as the output guide is switched off, a rapid decay of the QMS signal to the background level is expected, only limited by the time the molecules that already left the guide need to fly to the detector, typically less than 1.0 ms. Indeed, a fast decay can be observed in the measurement shown in Fig 4.4 b), but it is accompanied by a slow decay with a (1/e)-time of ≈150 ms.
As the measured signals are convoluted with this slow decay component, a deconvolution kernel has to be determined which allows to eliminate this component when processing the data. The signal reconstruction is clarified in the following example illustrated in Fig. 4.5. Consider a time-dependent raw signal, $S(t)$, consisting of a rectangular pulse. This pulse is processed in a detector with a certain pulse response function, $K(t)$, denoting the kernel of the signal transformation. The detector output, $D(t)$, depends on the history of $S(t)$ weighted with the detector response function:

$$D(t) = \int_0^\infty S(t-\tau)K(\tau)d\tau, \tag{4.1}$$

which is a convolution $D = S \otimes K$. In order to extract the detector response function from the detector output, it can be exploited that the Fourier transform F transforms the convolution in a product

$$F[(S \otimes K)(t)] = F[S(t)] \times F[K(t)] \tag{4.2}$$

from which the detector response function or kernel can easily be obtained given that the signal $S(t)$ is known. Starting from the measurement already shown in Fig 4.4 b), it is assumed that the guided flux into the detector is a sharp step function $\Theta(t)$ when the output is switched off. The measured signal $S_\Theta(t)$ can now be used to determine the deconvolution kernel by $F(K) = F(S_\Theta(t))/F(\Theta(t))$. For determining the lifetime of the molecules in the trap, the measured decay signal, $S_D(t)$, is deconvoluted by the transformation $S(t) = F^{-1}[F(S_D(t))/F(K)]$, where F^{-1} denotes the inverse Fourier transform. With this technique, the slow rise and fall of the signal 500 ms after switching on and off the input guide vanishes.
After the description of the deconvolution process, the trap measurements where the input quadrupole is periodically switched are discussed in detail. In order to demonstrate that the decay rate originates from the trap dynamics, an artificial hole was created in the trap by rapidly lowering the voltage on one small ring electrode to a constant value when the input quadrupole and, accordingly, the filling process is switched off.

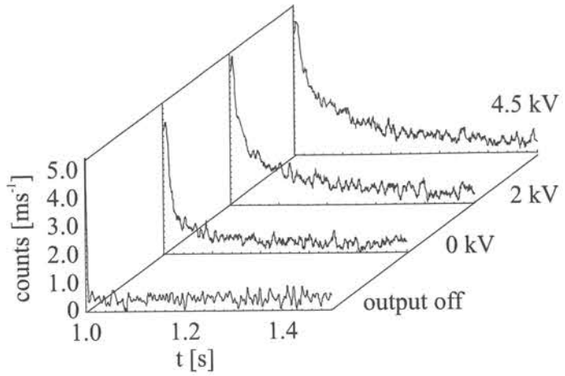

Figure 4.6: *Deconvoluted detector signals as a function of time for different trapping-field configurations. A rapid decay is observed when the output is switched off at t=1 s. The trap dynamics is revealed by rapidly switching the voltage on one small ring electrode from 4.5 kV to 0, 2 and 4.5 kV, respectively, after finishing the filling process in order to create an artificial hole in the trap. When the particular electrode is set to 0 kV a clear signal loss can be observed, whereas the slow decay caused by trapped molecules becomes dominant for higher voltages when the trap hole is closed. The signal trace obtained for output off serves as a reference.*

Fig. 4.6 shows the decay signals after deconvolution for reduced voltages on the particular ring electrode of 0, 2 and 4.5 kV, respectively. In the decay measurement where the voltage has been switched to 0 kV, a fast decay can be observed followed by a small and slow decay contribution. The fast decay is caused by the losses due to the weaker field near the particular ring electrode. The molecules causing the slow decay are either too slow to overcome even the weak field potential barrier or they do not encounter the weak field on their way inside the trap. Note that the start of the decay is delayed by the time the molecules need to pass through the output quadrupole. When the voltage on the ring electrode is raised to 2.0 kV, the loss rate decreases which leads to a reduction of the fast decay contribution, whereas the slow decay caused by molecules which are trapped longer is more pronounced. For the remaining curve, the voltage on the electrode is set to 4.5 kV and here the slow decay is dominant. However, an initial fast decay component can always be observed. In order to investigate this behavior, the Monte-Carlo simulation of the double bend quadrupole described in section 3.4 is extended to the electrostatic trap. The trap electrode configuration with the input and output quadrupole segments has been generated in an equidistant three-dimensional grid using SIMION 3D software. The grid dimensions are $150 \times 150 \times 150$ grid points with a grid unit of 0.1 mm. The electric field for a configuration with voltages of ± 4.5 kV is obtained by differentiation of the potential array generated by SIMION 3D. From the discrete electric field distribution in the three-dimensional grid, the continuous distribution is obtained by third order polynomial interpolation. Before the molecules leave the last section of the double bend quadrupole, their positions and velocities inside the quadrupole and their Stark shifts are registered. After these molecules with the registered starting conditions are injected into the input

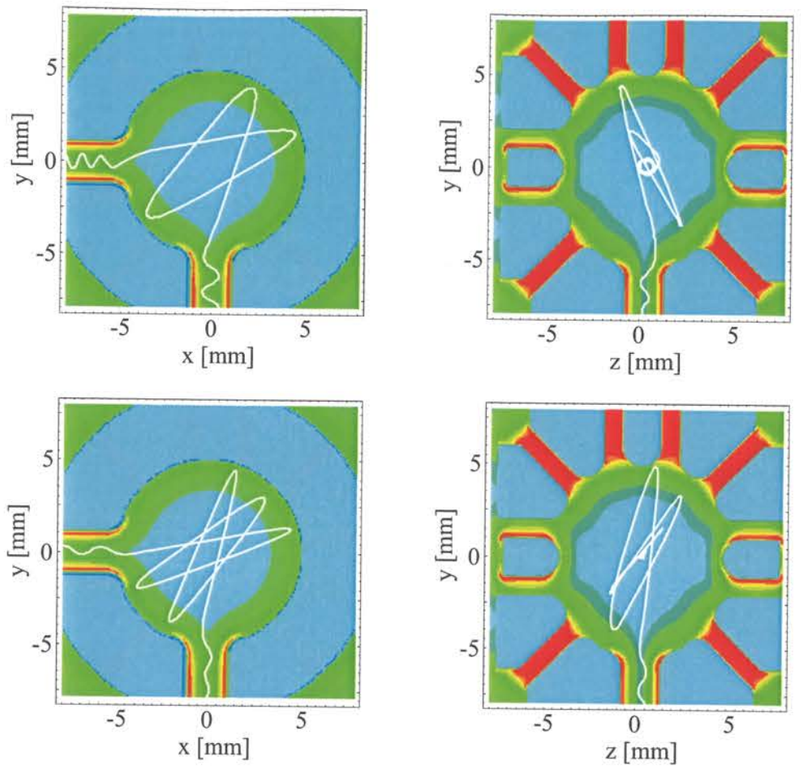

Figure 4.7: *Two trajectories of molecules which are trapped for less than 5 ms are shown. The pictures in one line show the projection of the particular trajectory on the xy plane and on the yz plane, respectively. The molecules enter the trap volume from below and they oscillate inside the trap until they find one of the exits. For short trapping times the oscillation predominantly takes place close to the xy plane which is described by the middle electrode so that the molecules quickly find the exits.*

quadrupole of the trap, they are propagated through the trap electric field. From the previous discussion it becomes clear that a large fraction of molecules cannot be trapped as the electric field inside the trap is lower compared to the quadrupole field. The trapped molecules are propagated until they find one of the exit quadrupoles where their positions, their velocities, and their Stark shifts are recorded.

In order to investigate the reason for the fast decay component, two representative trajectories from molecules which leave the trap after less than 5 ms are shown in Fig. 4.7. From the figure it is obvious that the fast decay is caused by a class of molecular trajectories which stay near the plane defined by the middle ring-electrode. As both exit channels lie in this plane, a fast escape is very probable. In contrast to this, Fig. 4.8 shows two trajectories from molecules which are trapped for more than 20 ms. Here, it can be seen that the trajectories fill the whole trap volume and the extended trapping time is caused

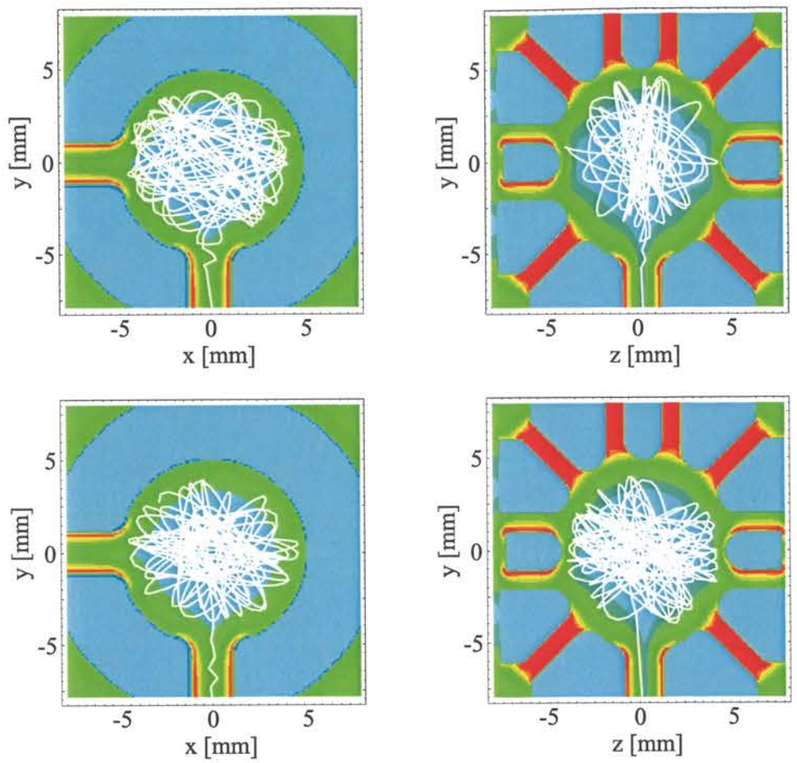

Figure 4.8: *Two trajectories of molecules which are trapped for longer than 20 ms are shown. The pictures in one line show the projection of the particular trajectory on the xy plane and on the yz plane, respectively. As the molecules fill the whole trap volume, it takes more time until they find an exit which results in an extended trapping time.*

by the fact that the molecules need more time to find one of the exits. As the lifetime of the molecules in the trap depends on how fast they find an exit, the lifetime is velocity dependent. Therefore the decay cannot be described by an exponential function and, hence, not by a (1/e)-lifetime. An alternative measure of the trap lifetime is the time after which half the molecules have left the trap. From the data obtained with voltages of ±4.5 kV a lifetime of 130 ±10 ms can be derived.
In the following, an analytic rate equation model as well as the simulation results are used to investigate the trap decay in detail. The rate of incoming molecules, $\dot{N}_{in}(v)$, and the rate of outgoing molecules, $\dot{N}_{out}(v)$, of a particular velocity v can be described by

$$\begin{aligned} \dot{N}_{in}(v) &= \phi(v) \\ \dot{N}_{out}(v) &= N(v)\, a\, v \end{aligned} \tag{4.3}$$

with $\phi(v)$ the incoming flux, $N(v)$ the number of trapped molecules of a particular velocity

v and a is a constant describing the average number of trap escapes per trajectory length. The parameter $\phi(v)$ is proportional to the velocity distribution of the molecules entering the trap. Note that the loss rate is proportional to the molecular velocity. During the filling process, the filling and the loss rate equilibrate ($\dot{N}_{in}(v) = \dot{N}_{out}(v)$) and the equilibrium trap population of a certain velocity class can be written as

$$N(v) = \phi(v)/av. \tag{4.4}$$

The differential equation for the population $N(v,t)$ of a velocity class in the trap at a time t after interrupting the filling process is

$$\dot{N}(v,t) = -N(v,t)av \tag{4.5}$$

which can be solved analytically by

$$N(v,t) = N(v)e^{-avt}. \tag{4.6}$$

The time dependence of the total loss rate is obtained by integrating $\dot{N}(v,t)$ over all molecular velocities

$$\dot{N}(t) = -\int_0^\infty \phi(v)e^{-avt}dv \tag{4.7}$$

$$= -1 + \frac{1}{2}\, a\, e^{\frac{1}{4}a^2t^2\alpha^2}\sqrt{\pi}\, t\, \alpha \left[1 - \mathrm{Erf}\left(\frac{a\,t\,\alpha}{2}\right)\right] \tag{4.8}$$

with a the number of escapes per path length, α the characteristic velocity of the molecules, and Erf the error function. The values for a and α can be obtained by fitting the functional form derived in eq. 4.8 to the deconvoluted experimental data using a and α as fit parameters. The experimental data can well be described by the fit with the optimum fit parameters $a = 1\,\mathrm{m}^{-1}$ and $\alpha = 14.2\,\mathrm{m/s}$. With this model, the average path length of a molecule inside the trap is roughly estimated to $\approx 1\,\mathrm{m}$. Fig. 4.9 shows the deconvoluted experimental data together with the trap decay rate obtained from the analytic estimate. The curve obtained from the analytic model is normalized to the experimental data so that the total number of molecules leaving the trap is equal in both cases. It can be seen that the analytic model describes the decay of the count rate to a good approximation.
The time dependence of the trap decay rate can also be verified with the simulation. For this purpose, 7400 trajectories of trapped molecules have been analyzed with regard to their trapping time. As the molecular trajectories were simulated consecutively, the simulation results need to be renormalized so that the results can be interpreted in terms of the equilibrium situation. Under equilibrium conditions, eqn. 4.4 shows that the number of molecules $N(v)$ of a particular velocity class inside the trap is given by the incoming flux $\phi(v)$ divided by the velocity v. Due to this, the contribution of fast molecules to the equilibrium particle number is reduced relative to the contribution of the slow molecules as they leave the trap faster. Therefore, the flux of molecules leaving the trap in a certain time interval has to be weighted with a factor proportional to the reciprocal molecule velocity $1/v$. When equilibrium conditions are reached, the trap signal consists of the sum over all the weighted flux contributions of the relevant time intervals. The trap decay can be modelled by successive subtraction of the weighted flux contributions from

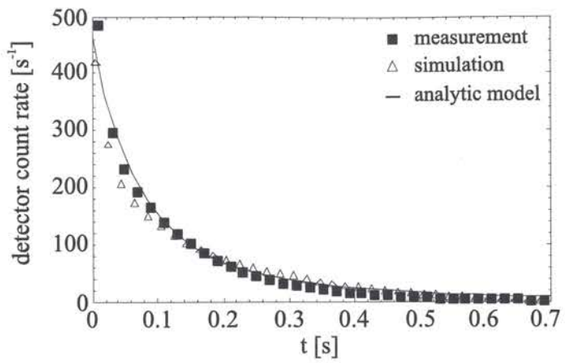

Figure 4.9: *Signal decay from the deconvoluted experimental data with electrode voltages of ±4.5 kV is shown together with the decay obtained from the simulation and from an analytic model explained in the text. Obviously, the simulation and the analytic model describe the shape of the decay to a good approximation.*

the sum over all contributions according to their trapping times. Here, the weighted flux contributions from the trap have been grouped in trapping time intervals with a width of 20 ms. With the successive subtraction of the contributions from the equilibrium rate, a time-dependent decay signal is obtained which is shown in Fig. 4.9.
Obviously, the decay trace obtained from the simulation results is in good agreement with the deconvoluted experimental data for short as well as for large trapping times. The investigation of the trap decay shows that the lifetime of the molecules is mainly limited by the exit channels, whereas collisions with the background gas do not contribute significantly under the present vacuum conditions.

4.3.3 Majorana Transitions

In the electrostatic trap, the average orientation of the dipole moment follows the direction of the electric field E adiabatically. This approximation holds for regions where $E \gg 0$, however, in the trap there exist small areas with $E \approx 0$ where the adiabatic approximation breaks down leading to a finite probability for a change in the orientation of the dipole moment. These Majorana transitions are possible decay channels as transitions to non-trapping molecular states are likely to occur. Fig. 4.10 a) shows the electric field strength along the z and the x-axis of the trap where the regions with a low field strength become obvious. The field in the central region of the trap is small over a wide range and it is zero in the center. Additionally, there are several spots where the field strength reduces to ≈ 500 V/cm. In these low-field regions, Majorana transitions are possible. In general, Majorana transitions are expected when the maximum rate of change $\dot{\theta}_{max} = |\dot{E}(\vec{r})|/E(\vec{r})$ of the electric field is faster than the frequency associated with the transition to non-trapping states. For a rough estimate, this frequency is chosen to be the inversion frequency of ND_3 with $\nu_{inv} = 1588.9$ MHz. This frequency corresponds to the energy gap between

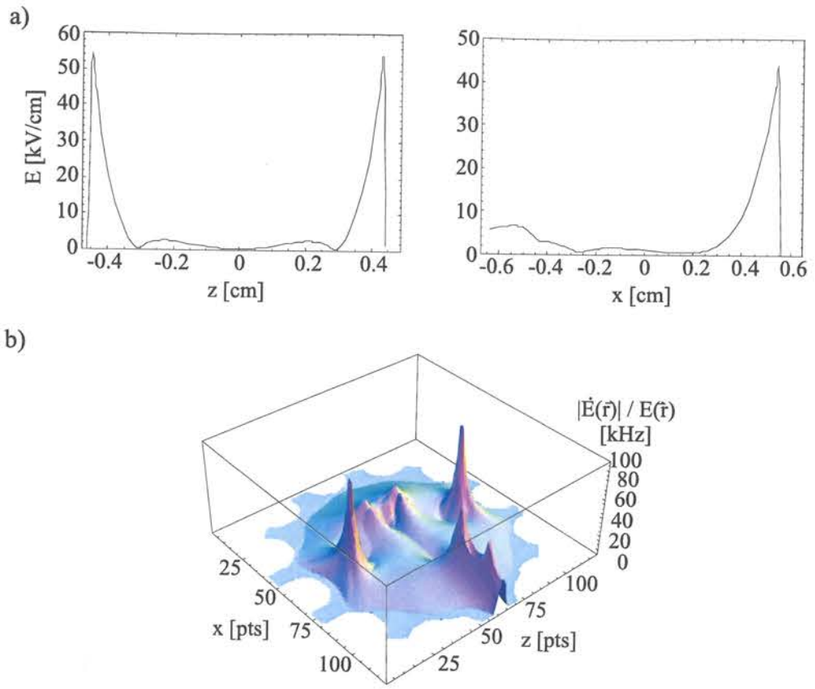

Figure 4.10: *(a) Electric field strength along the z-axis (trap axis) and along the x-axis. The asymmetry of the field along the x-axis is caused by the input quadrupole entering the trap. Note that the field minima in both graphs are at ≈ 500 V/cm. (b) The rate of change of the electric field in the xz-plane is shown. The white fringes indicate the position of the electrodes. Obviously, the rate of change is the highest at two spots close to the end caps and in the regions where the quadrupoles enter the trap volume.*

the high and low-field-seeking states for $E = 0$. In order to calculate $\dot{\theta}_{max}$, the derivative $|\dot{E}(\vec{r})|$ can be written as

$$|\dot{E}(\vec{r})| = |\frac{\partial E}{\partial x}\frac{dx}{dt} + \frac{\partial E}{\partial y}\frac{dy}{dt} + \frac{\partial E}{\partial z}\frac{dz}{dt}| \tag{4.9}$$

where the partial differentials of E are obtained numerically and the remaining differentials denote the velocity components of the molecule at position $\vec{r}$ inside the trap. With the average Stark shift of the molecules in the trap, the average velocity can be calculated. Section 4.3.5 will show that the average Stark shift of the molecules in the trap is equal to that in the guide. Fig. 4.10 b) shows the estimated rate of change $\dot{\theta}_{max}$ in the xz-plane of the trap. It can be seen that $\dot{\theta}_{max}$ is the highest at two spots close to the end caps and in the regions where the quadrupoles enter the trap volume. However, the maximum rate is far below the ND_3 inversion frequency so that from this rough estimate Majorana transitions are unlikely to happen. In a more accurate estimate, one has to take into account the possible transitions to other hyperfine levels lying much closer together than

the inversion levels. Due to the variety of molecular states involved, these transitions have been neglected. Nevertheless, the rough estimate provides useful information about the shape and the positions of the regions where transitions are likely to happen. In a larger trap, where these regions might become bigger, a more accurate estimate will be required. In case of the present trap, the rough estimate describes the experimental results well as no significant losses due to Majorana transitions can be observed.

4.3.4 Velocity Distribution

Longitudinal Velocity Distribution

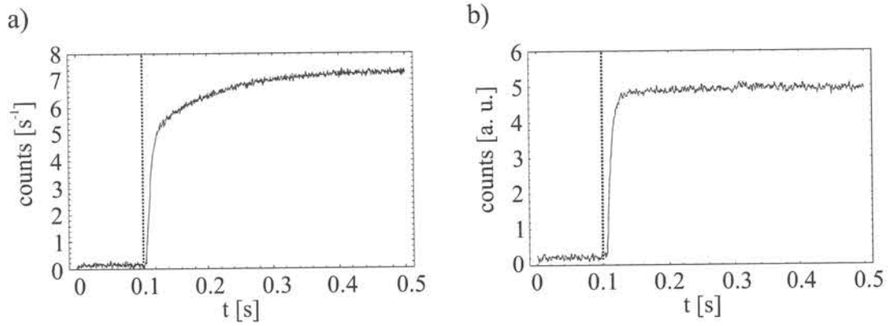

Figure 4.11: *(a) Measured time-of-flight signal obtained from molecules emerging from the trap with electrode voltages of ±4.5 kV. The rising slope is caused by molecules which are guided through the 17 cm long output quadrupole, and the vertical dashed line indicates the starting point of the guiding process. (b) Time-of-flight signal after deconvolution. The slow signal rise after t = 0.15 s vanishes and the deconvoluted signal is used to derive a velocity distribution.*

In the following, the temperature of the trapped ND_3 sample is determined by a measurement of the molecules' velocity distribution. Therefore, a time-of-flight (TOF) measurement is performed where the trap is continuously filled and only the 17 cm long output quadrupole is switched on and off at rate of 1 Hz. All electrodes were set to voltages of ±4.5 kV. As soon as the output quadrupole is switched on, molecules from the trap are guided to the detector where their arrival time is recorded. Fig. 4.11 a) shows a TOF signal which has developed after more than 50,000 cycles. As the rising slope of the TOF signal is affected by the spurious signal already discussed in section 3.6.5, the measured signal was deconvoluted according to the method described above using the same deconvolution kernel. The TOF signal after deconvolution is shown in Fig. 4.11 b). With the delay and the rising slope of the deconvoluted signal, the longitudinal velocity distribution can be derived by differentiation. For a single molecular state, the velocity distribution should show a relatively sharp velocity cut-off because the guide and the trap filter on kinetic energy. But given a mixture of states with different Stark shifts, the cut-off is smeared

out so that the velocity distribution can be described by a one-dimensional thermal distribution. Fig. 4.12 shows the velocity distribution obtained from the deconvoluted data. It

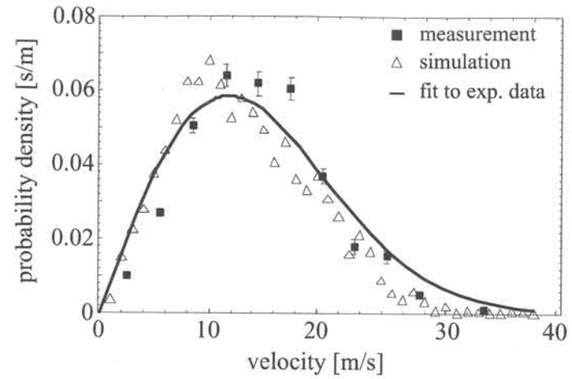

Figure 4.12: *Velocity distribution of trapped ND_3 molecules derived from data obtained with electrode voltages of ± 4.5 kV (squares). The line is a fit to the measured data of the functional form $(2v_l/\alpha^2)\exp[-v_l^2/\alpha^2]$, with the characteristic velocity $\alpha = 16.6 \pm 1$ m/s. The triangles denote simulation results.*

can be described by a characteristic velocity $\alpha = 16 \pm 1$ m/s with $\alpha = \sqrt{2k_BT/m}$, where k_B is the Boltzmann constant, T the temperature and m the molecular mass. This velocity corresponds to a motional temperature of 300 mK. Note that the molecular velocities in the output quadrupole are slightly smaller than inside the trap because the molecules are decelerated when entering the quadrupole field. However, as there are only conservative potentials involved, the temperature of the sample does not change. The experimental data are in good agreement with the simulation.

Transverse Velocity Distribution

The transverse velocity distribution of the trapped molecules can be estimated by recording the decrease of the flux of guided molecules in the output quadrupole when the electric field in the latter is reduced. During the measurements, the voltages on the input quadrupole and the trap were set to ±4.5 kV and the voltages on the input quadrupole were switched. In each measurement, the electric field in the output quadrupole was set to a different but constant value. It was observed that more than 90% of the flux from the trap can be guided even if the output quadrupole voltage is reduced down to ± 750 V so that most of the molecules can be two-dimensionally trapped in an electric field of only 15 kV/cm. Below this voltage, the guided flux decreases and at voltages of ±160 V (≈3 kV/cm), for example, the initial flux has reduced by a factor of two. The measured decrease of the signal amplitude as a function of the output quadrupole voltage is in good agreement with the simulation of the experiment. The measured data are shown in Fig. 4.13 a), together with the simulation results. In the simulation, the molecules emerging from the trap are

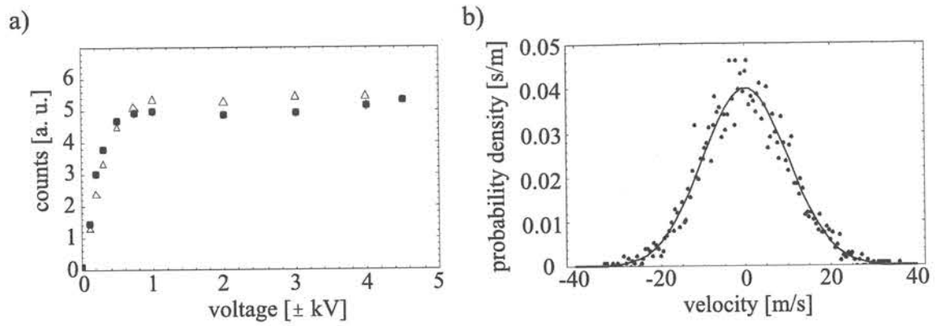

Figure 4.13: *(a) Signal amplitude from trapped molecules as a function of the output quadrupole voltages. The measured data (boxes) are in good agreement with the simulation results (triangles). The increase in signal as a function of the quadrupole voltages enables an estimation of the transverse velocity distribution. (b) Transverse velocity distribution obtained from the simulation with trap electrode voltages of ± 4.5 kV. The line is a fit of the functional form* $1/(\sqrt{\pi}\alpha)\exp[-v_t^2/\alpha^2]$ *with the characteristic velocity* $\alpha = 14.2 \pm 0.2$ *m/s.*

propagated in a segmented guide with the particular voltage differences. For detection, the molecules have to pass the QMS inlet aperture which is positioned at a distance of 1 cm behind the guide. The agreement between simulation and experiment justifies the assumption that the transverse velocity distribution in the experiment can be described with the distribution obtained from the simulation. Furthermore, the measurement shown in Fig. 4.13 a) shows an interesting feature at the output voltage range between ±1 kV and ±4 kV. It can be observed that the signal amplitude shows a slight dip at ±2 kV before it rises again towards higher output voltages. This feature can also be observed in the simulation. In principle, one would expect a steady increase of the guided flux with an increase of the output voltages. However, for low output voltages, the molecules are accelerated at the transition from the trap quadrupole segment to the output quadrupole due to the potential difference. Therefore, the longitudinal velocity of the molecules decreases for higher output voltages. The dip can be explained by the fact that slower molecules miss the detector inlet aperture with a higher probability because their transversal spread behind the guide is larger. Fig. 4.13 b) shows the simulated transverse velocity distribution in the guide with a characteristic velocity of $\alpha = 14.2$ m/s.
It follows that the characteristic velocity α is roughly equal for the longitudinal and the transversal velocity distribution, in contrast to the situation in the input quadrupole guide. There, the longitudinal velocities can be much higher as longitudinal filtering is less restrictive than transverse filtering. The trap equally filters the longitudinal and the transverse velocities and, additionally, randomizes these two degrees of freedom. This leads to an equilibration of the velocity distributions as it is confirmed by the simulation.

4.3.5 Flux Characterization

Flux dependence on the electrode voltages

With the angle distribution of the guided molecules behind the output quadrupole and the sensitivity of the QMS, the total flux emerging from the trap can be determined. From the measured angle distribution it has been determined that only 15% of the guided flux reaches the detector. As the detector sensitivity is of the order of 10^{-4} counts/molecule, the guided flux from the trap with all electrodes set to ±4.5 kV amounts to $3\times10^8\,s^{-1}$. If this number is compared with the input flux of $\approx 2\times10^{10}\,s^{-1}$, the trapped ratio amounts to 1.5% which is in agreement with the simulation results. Comparable trapping results were obtained with other dipolar gases like formaldehyde (CH_2O) and methylchloride (CH_2Cl) which also show a linear Stark effect. This shows that the continuously loadable trap is suited for various gases with a sufficiently large Stark shift. Similar to the situation in

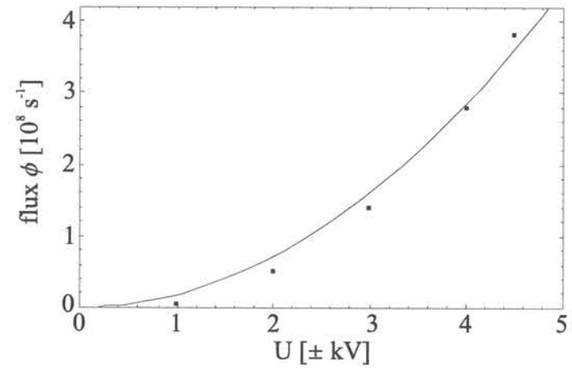

Figure 4.14: *Guided flux* ϕ *out of the trap as a function of the electrode voltages* U*. The voltages were changed on the trap electrodes as well as on the input and output quadrupoles. The line is a quadratic fit with the functional form* $\phi = aU^2$*.*

the double bend quadrupole, it can be observed that the guided flux from the trap shows a quadratic dependence on the applied electric field for a molecule with a linear Stark shift. Fig. 4.14 shows the measured flux of ND_3 molecules obtained after averaging over 5000 cycles. The quadratic rise proves that the states contributing to the signal have a linear Stark shift. With the knowledge of the average speed $\bar{v} = 2\alpha/\sqrt{\pi}$ and the total molecular flux Φ out of the trap, one can estimate the number density n in the trap by $\Phi = \frac{1}{4}n\bar{v}A$, where A is the effective area of each of the two exit channels. The radius of the circular effective area A can be approximated by the half width of the molecular density distribution inside the guide which has been shown in section 3.18. For electrode voltages of ±4.5 kV, the radius of the area A is about 400 μm. Assuming an average molecular speed $\bar{v}$ of 18 m/s, the number density inside the trap is of the order of $10^8\,cm^{-3}$ resulting in a number of $\approx 6\times10^7$ trapped molecules.

Flux dependence on the input guide voltages

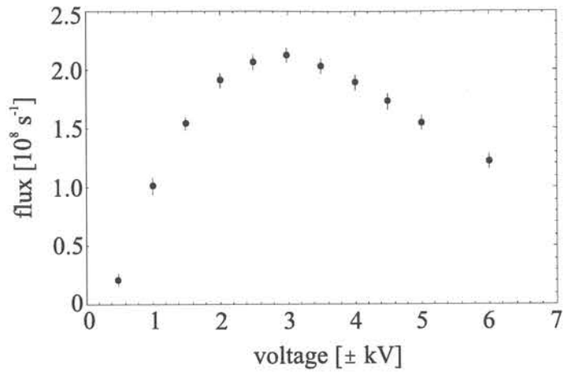

Figure 4.15: *Measured flux emerging from the trap as a function of the input quadrupole voltages. The voltages on the trap and the output quadrupole electrodes are set to the constant values of ±4 kV. For small input quadrupole voltages, the flux emerging from the trap increases as the flux in the input quadrupole increases. At a voltage of ±3 kV, the flux reaches a maximum as the maximum velocity after the guide is comparable to the maximum velocity accepted by the trap. For higher voltages, the molecules are accelerated due to the potential difference between the quadrupole and the trap which causes a reduction of the trap signal.*

In a further measurement, the flux from the trap with constant electrode voltages of ±4 kV has been investigated when the voltages on the input quadrupole have been varied. The experimental data are shown in Fig. 4.15. For small voltages, the flux from the trap increases as the flux in the input quadrupole increases. The flux reaches a maximum at voltages of ±3 kV even though the trap is set to voltages of ±4 kV. The reason for the occurrence of the maximum below the trap voltage values is the following: Due to geometric reasons the electric field in the trap is smaller than the field inside the quadrupole at equal voltages. Additionally, the quadrupole guide with a comparatively large curvature accepts higher velocities than the trap. When the input quadrupole voltages are further increased, the guidable velocities as well as the average potential energy of the molecules in the guide increases. The increase in potential energy leads to an acceleration of the molecules when entering the lower field region of the trap as the potential energy is converted into kinetic energy. This effect is responsible for the decrease of the guided flux for higher voltages.

Flux dependence on the reservoir pressure

In the following, the flux dependence on the reservoir pressure is investigated. The measurements were performed in a reservoir pressure range from 0.15 mbar to 3.0 mbar and the nozzle temperature has been set to 150 K. All electrodes are set to voltages of ±4.5 kV. The resulting flux curve is shown in Fig. 4.16, together with the flux from the input guide

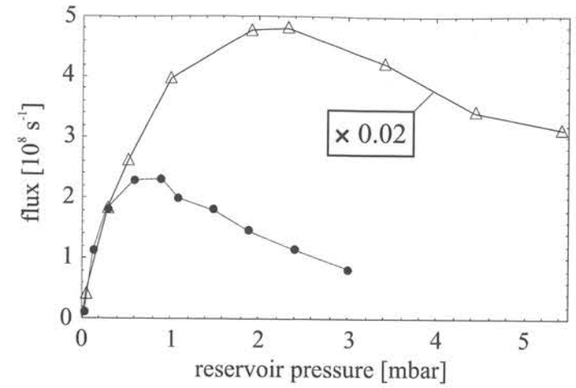

Figure 4.16: *Flux from the trap (circles) together with the flux from the input guide (triangles) as a function of the nozzle pressure at electrode voltages of ±4.5 kV. Note that the flux from the input guide is ≈ 50 times higher on this scale. Compared to the flux from the guide, the flux from the trap reaches a maximum at a lower reservoir pressure.*

already discussed in section 3.6.3. Similar to the situation in the input guide, the flux from the trap increases linearly and it starts deviating from the linear dependence above a reservoir pressure of ≈ 0.3 mbar. At this pressure the Knudsen regime, where the mean free path is larger than the nozzle diameter, changes over into the viscous regime, where intermolecular collisions along the capillary frequently occur. Especially the slowest molecules are susceptible for collisions with fast molecules as it takes them longer to pass the nozzle and the first part of the guide which is directly in the beam of fast, not-guided, molecules. When the pressure is further increased, collisions quickly remove the slow molecules which can be observed in Fig. 4.16: After the deviation from the linear behavior, the maximum flux from the trap is reached at a reservoir pressure of ≈ 0.8 mbar before the flux decreases again for higher pressures. The signal from the trap is particularly sensitive on the depletion of the low velocities in the guided flux as only the slowest molecules can be trapped. Therefore, the flux from the trap reaches its maximum value at lower pressures compared to the flux in the guide.

Stark shift distribution

Fig. 4.17 shows the simulated Stark shift distribution of ND_3 molecules emerging from the trap. The distribution is based on the Stark shift values of 7300 molecules, and it is very similar to the distribution in the input quadrupole guide shown in section 3.17. The two exposed peaks are a feature resulting from the discretisation. The similarity of both distributions is obvious as the occurrence of different Stark shifts in the guide and the trapped gas should be a conserved quantity, independent on how deep the limiting electric field value filters the original velocity distribution. Therefore, the relative abundance of the molecular states inside the trap should be the same as that in the guided beam, given

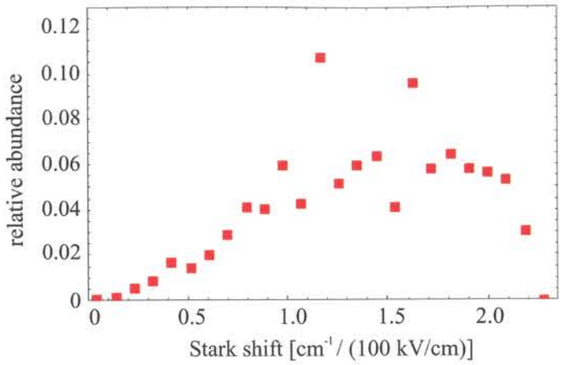

Figure 4.17: *Simulated Stark shift distribution of molecules emerging from the trap. The Stark shift distribution of the trapped molecules is very similar to the distribution in the input quadrupole guide.*

in Tab. 3.1. From the distribution, the average Stark potential experienced by the trapped molecules can be calculated to $\approx 1.4\,\mathrm{cm}^{-1}/100\,\frac{kV}{cm}$ which results in a trap depth of 800 mK. As expected, the trap depth of 800 mK is substantially higher than the temperature of the trapped molecules of 300 mK derived from their velocity distribution.

4.4 Conclusion and Outlook

In this chapter a continuously loaded, large-volume electrostatic trap for polar molecules is demonstrated experimentally. The results show that a sample of ND_3 molecules at a density of $10^8\,\mathrm{cm}^{-3}$ can be trapped with a lifetime of 130 ± 10 ms. It has been found that the trap lifetime is basically governed by the probability of the molecules to leave the trap via the exit channels. In principle, the probability of finding these holes is small and can even be made arbitrary small by making the trap volume and/or the electric field larger. The longitudinal velocity distribution of the trapped molecules in the output guide is obtained by a time-of-flight measurement and it can be described by a characteristic velocity $\alpha = 16.6$ m/s. Even though the setup does not allow a direct measurement of the transverse velocity, the simulation results indicate that the transverse velocity distribution in the output guide can be described by a characteristic velocity $\alpha = 14.2$ m/s which is consistent with an indirect measurement. From the similarity of the characteristic velocities it can be seen that the trap equally filters the longitudinal and the transverse velocities and, additionally, randomizes these two degrees of freedom. This leads to an equilibration of the velocity distributions. The temperature of the trapped sample is determined to 300 mK. These results indicate that it is possible to filter and trap translationally cold molecules at comparatively high densities from a thermal reservoir. Here, the trap is filled from a quadrupole guide, but it is also conceivable to produce the trapped molecules inside the trap, for example by reactive collisions, buffer gas loading or crossed molecular beam techniques [70]. A single output guide would then allow the continuous extraction of the

molecules out of the production region. The use of electrostatic fields for trapping offers many perspectives, as electric fields can be made in a wide variety of shapes and they can be ramped or rapidly switched. Furthermore, electric fields can be superimposed with magnetic or optical traps. For the future, it would be interesting to investigate to which extent the trap lifetime can be elongated by the use of a larger trap with an increased trap surface. The present setup is particularly well suited for these investigations as the lifetime is not limited by the background pressure. The basic goal behind the extension of the trap lifetime is to see indications of cold collisions in the trap. The investigation of cold collisions between polar molecules is very important as they provide valuable information for future evaporative cooling experiments.

A remarkable step forward to a cold and dense sample of molecules would be a combination of the guiding and trapping technique with buffer-gas cooling in a helium cryostat. In such a cryostat, cold molecules can be produced by thermalization with cold helium vapor. It should be possible to guide the cold molecules out of the cryogenic cell where they can be trapped. The advantages of trapping the molecules outside the cryostat are the better optical access and a better isolation of the trapped sample from the helium vapor. However, the helium might cause problems because of voltage breakthroughs at the high voltages required for guiding. If this problem can be solved, the use of a cryostat holds promise to produce molecules with cold internal and external degrees of freedom.

The availability of state-selected molecules at sufficiently high densities is a key precondition for entering the fields of research outlined in the introduction of this thesis. It is important to note that the field of cold molecules is still a young field of research and a growing number of methods for manipulation and trapping are under investigation in the different research groups. The methods available at present already allow a reliable control of a molecular sample and they provide good starting conditions for the investigation of cooling methods suited for molecules. The demonstration of a method which is able to efficiently cool a molecular sample would be a milestone in molecular physics. Once cold and dense samples are available, the anisotropic and long-range dipole-dipole interaction could be observed and new phases of matter could be searched. The field of precision measurements would benefit enormously and, with the increased interaction times of the cooled molecules with external fields, one can think of pushing the current experimental limits. This is, for example, strongly required for measurements which are searching for time symmetry violations in polar molecules. The field of cold chemistry is also of considerable interest to physicists and chemists. With regard to this, the trap developed in this experiment offers the intriguing possibility of an electrostatic reaction chamber. Provided electrostatic or mechanical valves can be developed, one can even envision a small cold chemical factory made out of a network of interconnected "reaction vessels" with new possibilities in controlling chemical reactions.

Bibliography

[1] C. S. Wu, E. Ambler, R. W. Hayward, D. D. Hoppes, and R. F. Hudson. Experimental Test of Parity Conservation in Beta Decay. *Phys. Rev.*, 105:1413, 1957.

[2] J. H. Christenson, J. Cronin, V. L. Fitch, and R. Turlay. Evidence for the 2π decay of the K_2^0 meson. *Phys. Rev. Lett.*, 13:138, 1964.

[3] L. R. Hunter. Tests of Time-Reversal Invariance in Atoms, Molecules and the Neutron. *Science*, 252:73, 1991.

[4] E. Hinds and B. Sauer. Electron dipole moments. *Physics World*, page 37, April 1997.

[5] P. G. H. Sandars. Measurability of the proton electric dipole moment. *Phys. Rev. Lett.*, 19:1396, 1967.

[6] B. C. Regan, E. D. Commins, C. J. Schmidt, and D. DeMille. New Limit on the Electron Electric Dipole Moment. *Phys. Rev. Lett.*, 88:071805, 2002.

[7] J. J. Hudson, B. E. Sauer, M. R. Tarbutt, and E. A. Hinds. Measurement of the Electron Electric Dipole Moment Using YbF Molecules. *Phys. Rev. Lett.*, 89:023003, 2002.

[8] D. E. Egorov, J. D. Weinstein, D. Patterson, B. Friedrich, and J. M. Doyle. Spectroscopy of laser-ablated buffer-gas-cooled PbO at 4 K and the prospects for measuring the electric dipole moment of the electron. *Phys. Rev. A*, 63:030501, 2001.

[9] N. Fortson, P. Sandars, and S. Barr. The Search for a Permanent Electric Dipole Moment. *Physics Today*, page 33, June 2003.

[10] N. F. Ramsey. Electric Dipole Moment of the Neutron. *Annu. Rev. Nucl. Part. Sci.*, 40:1, 1990.

[11] E. Bodo and F. A. Gianturco. Features of chemical reactions at vanishing kinetic energy: the presence of internally "hot" reagents. *Eur. Phys. J. D*, 31:423, 2004.

[12] N. Balakrishnan and A. Dalgarno. Chemistry at ultracold temperatures. *Chem. Phys. Lett.*, 341:653, 2001.

[13] T. Takayanagi and Y. Kurosaki. van der Waals resonances in cumulative reaction probabilities for the F+H_2, D_2, and HD reactions. *J. Chem. Phys.*, 109:8929, 1998.

[14] E. Bodo, F. A. Gianturco, N. Balakrishnan, and A. Dalgarno. Chemical reactions in the limit of zero kinetic energy: virtual states and Ramsauer minima in F+H_2→HF+H. *J. Phys. B: At. Mol. Opt. Phys.*, 37:3641, 2004.

[15] P. F. Weck and N. Balakrishnan. Chemical reactivity of ultracold polar molecules: investigation of H+HCl and H+DCl collisions. *Eur. Phys. J. D*, 31:417, 2004.

[16] L. Santos, G. V. Shlyapnikov, P. Zoller, and M. Lewenstein. Bose-Einstein Condensation in Trapped Dipolar Gases. *Phys. Rev. Lett.*, 85:1791, 2000.

[17] M. Baranov, L. Dobrek, K. Goral, L. Santos, and M. Lewenstein. Ultracold dipolar gases - a challenge for experiments and theory. *Nobel Symposium "Coherence and Condensation in Quantum Systems"*, Göteborg, 4.-7.12.2001.

[18] S. Giovanazzi, A. Görlitz, and T. Pfau. Tuning the Dipolar Interaction in Quantum Gases. *Phys. Rev. Lett.*, 89:130401, 2002.

[19] A. Griesmaier, J. Werner, S. Hensler, J. Stuhler, and T. Pfau. Bose-Einstein Condensation of Chromium. *Phys. Rev. Lett.*, 94:160401, 2005.

[20] I. F. Silvera and J. T. M. Walraven. Stabilization of Atomic Hydrogen at Low Temperatures. *Phys. Rev. Lett.*, 44:164, 1980.

[21] H. F. Hess, G. P. Kochanski, J. M. Doyle, N. Masuhara, D. Kleppner, and T. J. Greytak. Magnetic Trapping of Spin-Polarized Atomic Hydrogen. *Phys. Rev. Lett.*, 59:672, 1987.

[22] R. van Roijen, J. J. Berkhout, S. Jaakkola, and J. T. M. Walraven. Magnetic Trapping of Spin-Polarized Atomic Hydrogen. *Phys. Rev. Lett.*, 61:931, 1988.

[23] J. Kim, B. Friedrich, D. P. Katz, D. Patterson, J. D. Weinstein, R. DeCarvalho, and J. M. Doyle. Buffer-Gas Loading and Magnetic Trapping of Atomic Europium. *Phys. Rev. Lett.*, 78:3665, 1997.

[24] J. D. Weinstein, R. DeCarvalho, J. Kim, D. Patterson, B. Friedrich, and J. M. Doyle. Magnetic trapping of atomic chromium. *Phys. Rev. A*, 57:R3173, 1998.

[25] J. M. Doyle, B. Friedrich, J. Kim, and D. Patterson. Buffer-gas loading of atoms and molecules into a magnetic trap. *Phys. Rev. A*, 52:R2515, 1995.

[26] J. D. Weinstein, R. DeCarvalho, T. Guillet, B. Friedrich, and J. M. Doyle. Magnetic trapping of calcium monohydride molecules at millikelvin temperatures. *Nature*, 395:148, 1998.

[27] D. Egorov, T. Lahaye, W. Schöllkopf, B. Friedrich, and J. M. Doyle. Buffer-gas cooling of atomic and molecular beams. *Phys. Rev. A*, 66:043401, 2002.

[28] H. F. Hess. Evaporative cooling of magnetically trapped and compressed spin-polarized hydrogen. *Phys. Rev. B*, 34:3476, 1986.

[29] N. Masuhara, J. M. Doyle, J. C. Sandberg, D. Kleppner, T. J. Greytak, H. F. Hess, and G. P. Kochanski. Evaporative Cooling of Spin-Polarized Atomic Hydrogen. *Phys. Rev. Lett.*, 61:935, 1988.

[30] M. H. Anderson, J. R. Ensher, M. R. Matthews, C. E. Wieman, and E. A. Cornell. Observation of Bose-Einstein condensation in a dilute atomic vapor. *Science*, 269:198, 1995.

[31] C. C. Bradley, C. A. Sackett, J. J. Tollett, and R. G. Hulet. Evidence of Bose-Einstein Condensation in an Atomic Gas with Attractive Interactions. *Phys. Rev. Lett.*, 75:1687, 1995.

[32] K. B. Davis, M.-O. Mewes, M. R. Andrews, N. J. van Druten, D. S. Durfee, D. M. Kurn, and W. Ketterle. Bose-Einstein Condensation in a Gas of Sodium Atoms. *Phys. Rev. Lett.*, 75:3969, 1995.

[33] H. R. Thorsheim, J. Weiner, and P. S. Julienne. Laser-induced photoassociation of ultra-cold sodium atoms. *Phys. Rev. Lett.*, 58:2420, 1987.

[34] J. Weiner, V. S. Bagnato, S. C. Zilio, and P. S. Julienne. Experiments and theory in cold and ultracold collisions. *Rev. Mod. Phys.*, 71:1, 1999.

[35] A. P. Mosk, M. W. Reynolds, T. W. Hijmans, and J. T. M. Walraven. Photoassociation of spin-polarized hydrogen. *Phys. Rev. Lett.*, 82:307, 1999.

[36] N. Herschbach, P. J. J. Tol, W. Wassen, W. Hogervorst, G. Woestenenk, J. W. Thomsen, P. Van der Straten, and A. Niehaus. Photoassociation spectroscopy of cold He (2^3 S) atoms. *Phys. Rev. Lett.*, 84:1874, 2000.

[37] G. Zinner, T. Binnewies, F. Riehle, and E. Tiemann. Photoassociation of Cold Ca Atoms. *Phys. Rev. Lett.*, 85:2292, 2000.

[38] Y. Takasu, K. Komori, K. Honda, M. Kumakura, T. Yabuzaki, and Y. Takahashi. Photoassociation Spectroscopy of Laser-Cooled Ytterbium Atoms. *Phys. Rev. Lett.*, 93:123202, 2004.

[39] H. Wang and C. Stwalley. Ultracold photoassociative spectroscopy of heteronuclear alkali-metal diatomic molecules. *J. Chem. Phys.*, 108:5767, 1998.

[40] U. Schlöder, C. Silber, and C. Zimmermann. Photoassociation of heteronuclear lithium. *Appl. Phys. B*, 73:801, 2001.

[41] A. J. Kerman, J. M. Sage, S. Sainis, T. Bergeman, and David DeMille. Production and State-Selective Detection of Ultracold RbCs Molecules. *Phys. Rev. Lett.*, 92:153001, 2004.

[42] C. Haimberger, J. Kleinert, M. Bhattacharya, and N. P. Bigelow. Formation and detection of ultracold ground-state polar molecules. *Phys. Rev. A*, 70:021402, 2004.

[43] M. W. Mancini, G. D. Telles, A. R. L. Caires, V. S. Bagnato, and L. G. Marcassa. Observation of Ultracold Ground-State Heteronuclear Molecules. *Phys. Rev. Lett.*, 92:133203, 2004.

[44] D. Wang *et al.* Photoassociative Production and Trapping of Ultracold KRb Molecules. *Phys. Rev. Lett.*, 93:243005, 2004.

[45] D. Comparat, N. Vanhaecke, C. Lisdat, and P. Pillet. *Formation and Trapping of Cold Molecules.* In: M. Weidemüller and C. Zimmermann (Ed.), Interactions in Ultracold Gases, Wiley-VCH, Weinheim, p. 320, 2003.

[46] A. N. Nikolov, J. R. Enscher, E. E. Eyler, H. Wang, W. C. Stwalley, and P. L. Gould. Efficient production of ground state potassium molecules at sub-mk temperatures by two-step photoassociation. *Phys. Rev. Lett.*, 84:246, 2000.

[47] R. Wynar, R. S. Freeland, D. J. Han, C. Ryu, and D. J. Heinzen. Molecules in a Bose-Einstein Condensate. *Science*, 287:1016, 2000.

[48] J. M. Gerton, D. Strekalov, I. Prodan, and R. G. Hulet. Direct observation of growth and collapse of a Bose-Einstein condensate with attractive interactions. *Nature*, 408:692, 2000.

[49] D. Jaksch, V. Venturi, J. I. Cirac, C. J. Williams, and P. Zoller. Creation of a Molecular Condensate by Dynamically Melting a Mott Insulator. *Phys. Rev. Lett.*, 89:040402, 2002.

[50] T. Rom, T. Best, O. Mandel, A. Widera, M. Greiner, T. W. Hänsch, and I. Bloch. State Selective Production of Molecules in Optical Lattices. *Phys. Rev. Lett.*, 93:073002, 2004.

[51] E. A. Donley, N. R. Claussen, S. T. Thompson, and C. E. Wieman. Atom-molecule coherence in a Bose-Einstein condensate. *Nature*, 417:529, 2002.

[52] S. Dürr, T. Volz, A. Marte, and G. Rempe. Observation of Molecules Produced from a Bose-Einstein Condensate. *Phys. Rev. Lett.*, 92:020406, 2004.

[53] K. Xu, T. Mukaiyama, J. R. Abo-Shaeer, J. K. Chin, D. E. Miller, and W. Ketterle. Formation of Quantum-Degenerate Sodium Molecules. *Phys. Rev. Lett.*, 91:210402, 2003.

[54] D. S. Petrov, C. Salomon, and G. V. Shlyapnikov. Weakly Bound Dimers of Fermionic Atoms. *Phys. Rev. Lett.*, 93:090404, 2004.

[55] C. A. Regal, C. Ticknor, J. L. Bohn, and D. S. Jin. Creation of ultracold molecules from a Fermi gas of atoms. *Nature*, 424:47, 2003.

[56] K. E. Strecker, G. B. Partridge, and R. G. Hulet. Conversion of an Atomic Fermi Gas to a Long-Lived Molecular Bose Gas. *Phys. Rev. Lett.*, 91:080406, 2003.

[57] J. Cubizolles, T. Bourdel, S. J. J. M. F. Kokkelmans, G. V. Shlyapnikov, and C. Salomon. Production of Long-Lived Ultracold Li_2 Molecules from a Fermi Gas. *Phys. Rev. Lett.*, 91:240401, 2003.

[58] S. Jochim, M. Bartenstein, A. Altmeyer, G. Hendl, C. Chin, J. Hecker Denschlag, and R. Grimm. Pure Gas of Optically Trapped Molecules Created from Fermionic Atoms. *Phys. Rev. Lett.*, 91:240402, 2003.

[59] M. Greiner, C. A. Regal, and D. S. Jin. Emergence of a molecular Bose-Einstein condensate from a Fermi gas. *Nature*, 426:537, 2003.

[60] H. L. Bethlem. *Deceleration and Trapping of Polar Molecules using Time-varying Electric Fields.* Thesis, Katholieke Universiteit Nijmegen, 2002.

[61] H. L. Bethlem, G. Berden, and G. Meijer. Decelerating Neutral Dipolar Molecules. *Phys. Rev. Lett.*, 83:1558, 1999.

[62] H. L. Bethlem, G. Berden, A. J. A. van Roij, F. M. H. Crompvoets, and G. Meijer. Trapping Neutral Molecules in a Travelling Potential Well. *Phys. Rev. Lett.*, 84:5744, 2000.

[63] H. L. Bethlem, A. J. A. van Roij, R. T. Jongma, and G. Meijer. Alternate Gradient focusing and deceleration of a molecular beam. *Phys. Rev. Lett.*, 88:133003, 2002.

[64] M. R. Tarbutt, H. L. Bethlem, J. J. Hudson, V. L. Ryabov, V. A. Ryzhov, B. E. Sauer, G. Meijer, and E. A. Hinds. Slowing Heavy, Ground-State Molecules using an Alternating Gradient Decelerator. *Phys. Rev. Lett.*, 92:173002, 2004.

[65] H. L. Bethlem, F. M. H. Crompvoets, R. T. Jongma, S. Y. T. van de Meerakker, and G. Meijer. Deceleration and trapping of ammonia using time-varying electric fields. *Phys. Rev. A*, 65:053416, 2002.

[66] H. L. Bethlem, G. Berden, F. M. H. Crompvoets, R. T. Jongma, A. J. A. van Roij, and G. Meijer. Electrostatic trapping of ammonia molecules. *Nature*, 406:491, 2000.

[67] J. R. Bochinski, E. R. Hudson, H. J. Lewandowski, G. Meijer, and J. Ye. Phase Space Manipulation of Cold Free Radical OH Molecules. *Phys. Rev. Lett.*, 91:243001, 2003.

[68] M. Gupta and D. Herschbach. Slowing and Speeding Molecular Beams by Means of a Rapidly Rotating Source. *J. Phys. Chem. A*, 105:1626, 2001.

[69] B. Friedrich. Slowing of supersonically cooled atoms and molecules by time-varying nonresonant dipole forces. *Phys. Rev. A*, 61:025403, 2000.

[70] M. S. Elioff, J. J. Valentini, and D. W. Chandler. Subkelvin Cooling NO Molecules via "Billard-like" Collisions with Argon. *Science*, 302:1940, 2003.

[71] N. F. Ramsey. *Molecular Beams.* Oxford University Press, Oxford, 1956.

[72] G. Herzberg. *Infrared and Raman Spectra of Polyatomic Molecules.* Van Nostrand Reinhold, Inc., New York, 1945.

[73] J. Bulthuis. private communication.

[74] J. J. Sakurai and S. F. Tuan (editor). *Modern quantum mechanics.* Addison-Wesley Publishing Company, Inc., revised edition, 1994.

[75] C. H. Townes and A. L. Schawlow. *Microwave Spectroscopy.* Dover Publications, Inc., New York, 1975.

[76] R. G. Nuckolls, L. J. Rueger, and H. Lyons. Microwave Absorption Spectrum of ND_3. *Phys. Rev.*, 89:1101, 1953.

[77] G. Herzberg. *Molecular Spectra and Molecular Structure, III. Electronic Spectra and Electronic Structure of Polyatomic Molecules.* Van Nostrand Reinhold Company, New York, 1966.

[78] G. W. King, R. M. Hainer, and P. C. Cross. The Asymmetric Rotor. *J. Chem. Phys.*, 11:27, 1943.

[79] P. C. Cross, R. M. Hainer, and G. W. King. The Asymmetric Rotor. *J. Chem. Phys.*, 12:210, 1944.

[80] T. D. Hain, R. M. Moision, and T. J. Curtiss. Hexapole state-selection and orientation of asymmetric top molecules: CH_3F_2. *J. Chem. Phys.*, 111:6797, 1999.

[81] H. Friedburg, W. Paul. Reflexion eines Atomstrahles am Rande eines Magnetfeldes. *Naturwiss.*, 37:20, 1950.

[82] H. Friedburg, W. Paul. Optische Abbildung mit neutralen Atomen. *Naturwiss.*, 38:159, 1951.

[83] J. P. Gordon, H. J. Zeiger, and C. H. Townes. Molecular microwave oscillator and new hyperfine structure in the microwave spectrum of NH_3. *Phys. Rev.*, 95:282, 1954.

[84] H. G. Bennewitz, W. Paul, and C. Schlier. Fokussierung polarer Moleküle. *Z. Phys.*, 141:6, 1955.

[85] J. P. Gordon, H. J. Zeiger, and C. H. Townes. The Maser - New Type of Microwave Amplifier, Frequency Standard, and Spectrometer. *Phys. Rev.*, 99:1264, 1955.

[86] J. Reuss. *State Selection by Nonoptical Methods.* In: G. Scoles (Ed.), Atomic and Molecular Beam Methods, Vol. 1. Oxford University Press, New York, p.276, 1988.

[87] D. Auerbach, E. E. A. Bromberg, and L. Wharton. Alternate-Gradient Focusing of Molecular Beams. *J. Chem. Phys.*, 45:2160, 1966.

[88] D. Kakati and D.C. Lainé. Alternate-Gradient Focusing of a Molecular Beam of Ammonia. *Phys. Lett.*, 24A:676, 1967.

[89] D. Kakati and D.C. Lainé. Alternate-Gradient Focusing of Neutral Particles. *Phys. Lett.*, 28A:786, 1969.

[90] F. Günther and K. Schügerl. State selection of polar molecules by alternate gradient focusing. *Z. Phys. Chemie*, NF80:155, 1972.

[91] H. J. Loesch. A novel, simple rotational state analyzer/selector for polar linear molecules. *Chem. Phys.*, 207:427, 1996.

[92] H. J. Loesch and B. Scheel. Molecules on Kepler Orbits: An Experimental Study. *Phys. Rev. Lett.*, 85:2709, 2000.

[93] D. P. Katz. A storage ring for polar molecules. *J. Chem. Phys.*, 107:8491, 1997.

[94] F. M. H. Crompvoets, H. L. Bethlem, R. T. Jongma, and G. Meijer. A prototype storage ring for neutral molecules. *Nature*, 411:174, 2001.

[95] J. R. Bochinski, E. R. Hudson, H. J. Lewandowski, G. Meijer, and J. Ye. Phase Space Manipulation of Cold Free Radical OH Molecules. *Phys. Rev. Lett.*, 91:243001, 2003.

[96] W. H. Wing. Electrostatic Trapping of Neutral Atomic Particles. *Phys. Rev. Lett.*, 45:631, 1980.

[97] S. K. Sekatskii and J. Schmiedmayer. Trapping polar molecules with a charged wire. *Eur. Phys. Lett.*, 36:407, 1996.

[98] R. T. Jongma, G. von Helden, G. Berden, and G. Meijer. Confining CO molecules in stable orbits. *Chem. Phys. Lett.*, 270:304, 1997.

[99] F. Shimizu and M. Morinaga. Electric Trapping of Neutral Atoms. *Jpn. J. Appl. Phys. Part 2*, 31:L1721, 1992.

[100] E. Peik. Electrodynamic trap for neutral atoms. *Eur. Phys. J. D*, 6:179, 1999.

[101] J. van Veldhoven, H. L. Bethlem, and G. Meijer. An AC electric trap for ground-state molecules. *Phys. Rev. Lett.*, 94:083001, 2005.

[102] B. Ghaffari, J. M. Gerton, W. I. McAlexander, K. E. Strecker, D. M. Homan, and R. G. Hulet. Laser-free slow atom source. *Phys. Rev. A*, 60:3878, 1999.

[103] P. W. H. Pinkse, T. Junglen, T. Rieger, S. A. Rangwala, and G. Rempe. *Filtering Slow Polar Molecules from a Thermal Gas.* In: M. Weidemüller and C. Zimmermann (Ed.), Interactions in Ultracold Gases, Wiley-VCH, Weinheim, p. 477, 2003.

[104] P. Zugenmayer. Zur Theorie der Molekularstrahlerzeugung mit Hilfe zylindrischer Rohre. *Z. Angew. Phys.*, 3, 1966.

[105] R. D. Present. *Kinetic Theory of Gases.* McGraw-Hill Book Company, Inc., New York Toronto London, 1958.

[106] M. Wutz, H. Adam, W. Walcher, K. Jousten. *Handbuch Vakuumtechnik, 7. Auflage.* Vieweg, Braunschweig/Wiesbaden, 2000.

[107] S. A. Rangwala, T. Junglen, T. Rieger, P. W. H. Pinkse, and G. Rempe. A continuous source of translationally cold dipolar molecules. *Phys. Rev. A*, 67:043406, 2003.

[108] R.L. Summers. Gas Correction Factors for Bayard-Alpert Ionization Gauges. *NASA Technical Report, NASA-TN-D-5285*, 1969.

[109] *CRC Handbook of Chemistry and Physics.* CRC Press, Inc., 74. edition, **6**-94, 1993.

[110] T. Junglen, T. Rieger, S. A. Rangwala, P. W. H. Pinkse, and G. Rempe. Two-Dimensional Trapping of Dipolar Molecules in Time-Varying Electric Fields. *Phys. Rev. Lett.*, 92:223001, 2004.

List of Figures

List of Tables

Publications

S.A. Rangwala, T. Junglen, T. Rieger, P.W.H. Pinkse, and G. Rempe, Continuous source of translationally cold dipolar molecules, *Phys. Rev. A* **67**: 043406, 2003

P. W. H. Pinkse, T. Junglen, T. Rieger, S. A. Rangwala, and G. Rempe, Interactions in Ultracold Gases, 477, edited by M. Weidemüller and C. Zimmermann, (Wiley-VCH, Weinheim, 2003)

T. Junglen, T. Rieger, S.A. Rangwala, P.W.H. Pinkse, and G. Rempe, Two-Dimensional Trapping of Dipolar Molecules in Time-Varying Electric Fields, *Phys. Rev. Lett.* **92**: 223001, 2004

T. Junglen, T. Rieger, S.A. Rangwala, P.W.H. Pinkse, and G. Rempe, Slow ammonia molecules in an electrostatic quadrupole guide, *Eur. Phys. J. D* **31**: 365, 2004

T. Rieger, T. Junglen, S.A. Rangwala, P.W.H. Pinkse, and G. Rempe, Continuous Loading of an Electrostatic Trap for Polar Molecules, *Phys. Rev. Lett.* **95**: 173002, 2005

Danksagung

An dieser Stelle möchte ich all jenen meinen Dank aussprechen, die zum Gelingen dieser Arbeit beigetragen haben:

- An erster Stelle danke ich Prof. Gerhard Rempe, der mir in seiner Arbeitsgruppe die Möglichkeit gegeben hat, beim Aufbau eines neuen Experimentes mitwirken zu können. Seine sachkundige Unterstützung und die vielen anregenden Gespräche in jeder Phase der Arbeit waren mir eine große Hilfe. Besonders möchte ich mich für die stets angenehme Atmosphäre und das Vertrauen bedanken, das er mir entgegenbrachte.

- Mein besonderer Dank gilt auch Dr. Pepijn Pinkse, der mich seit den ersten Stunden dieses Experimentes freundschaftlich begleitet hat. Seine Geduld, seine Ermunterungen und seine Hilfe während der gesamten Zeit haben wesentlich zum Erfolg der Arbeit beigetragen.

- Dr. Sadiq Rangwala danke ich für die vielen konstruktiven Diskussionen und für seine engagierte Mitarbeit an diesem Experiment.

- Thomas Rieger, meinem Mitdoktoranden, danke ich für die von einem sehr freundschaftlichen Umgang geprägte gemeinsame Laborzeit. Auf seine Hilfe und seinen Einsatz konnte ich mich stets verlassen, und er hat großen Anteil am Zustandekommen dieser Arbeit. Unvergessen bleibt so manche Episode im täglichen Kampf mit dem Computer, bei dem er mir so oft zur Seite stehen mußte.

- Michael Motsch und Patrick Windpassinger danke ich für die kollegiale Zusammenarbeit und für die angenehme Atmosphäre im Büro.

- Den Spezialisten von der Technik Josef Bayerl, Franz Denk, Helmut Stehbeck und Thomas Wiesmeier, ohne deren tatkräftige Mitarbeit ein solches Experiment nicht durchführbar ist.

- Allen „BEClern", „Kavitäten", „Pistoleros" sowie den „Q-Gates" sei für die reibungslose Zusammenarbeit und für die bereitwillige Hilfe bei der Lösung von alltäglichen Problemen herzlich gedankt.

- Nicht unerwähnt lassen möchte ich die Mitarbeiter in der Werkstatt des MPQ, denen (fast) kein Auftrag zu kompliziert ist, und die die wesentlichen Bauteile für das Experiment angefertigt haben. Ihnen sei an dieser Stelle für ihre professionelle Arbeit gedankt.

- Einen ganz besonderen Dank möchte ich meinen Eltern Helga und Erwin Junglen für ihre bedingungslose Unterstützung während meiner gesamten Ausbildung aussprechen.
- Schließlich gilt mein Dank den Bonner Freunden und Kommilitonen und ganz besonders auch meiner Freundin Claudia Horn.